SYNTHESIS, CHARACTERIZATION, AND EXPERIMENTAL INVESTIGATION OF PHOTONIC CRYSTALS DERIVED FROM BIOLOGY

by

Matthew Ray Jorgensen

A dissertation submitted to the faculty of
The University of Utah
in partial fulfillment of the requirements for the degree of

Doctor of Philosophy

Department of Chemistry

University of Utah

May 2012

The University of Utah Graduate School

STATEMENT OF DISSERTATION APPROVAL

The dissertation of **Matthew Ray Jorgensen**

has been approved by the following supervisory committee members:

Michael H. Bartl	, Chair	**12-09-2011** Date Approved
Peter B. Armentrout	, Member	**12-09-2011** Date Approved
Edward M. Eyring	, Member	**12-09-2011** Date Approved
Thomas G. Richmond	, Member	**12-09-2011** Date Approved
Jordan Gerton	, Member	**12-09-2011** Date Approved

and by **Henry S. White**, Chair of the Department of **Chemistry**

and by Charles A. Wight, Dean of The Graduate School.

ABSTRACT

The synthesis, characterization, and nonclassical optical properties of photonic crystals (PCs) created from naturally occurring biological templates was studied. Biotemplated PCs were created from several different natural structures using sol-gel chemistry methods. PCs were characterized using a combination of reflection spectroscopy, SEM image analysis, three-dimensional structure modeling, photonic band structure calculations, and density of optical states calculations. The effect our PCs had on the density of optical states (DOS) was probed using time correlated single photon counting spectroscopy.

By carefully controlling the sol-gel chemistry used in the templating process, it is possible to synthesize hollow silica inverse, solid silica inverse, hollow titania inverse, solid titania inverse, and solid titania replicate structures. The inverse-type structures have the advantage of being accessible through a single templating step, while the titania replica is capable of a predicted full photonic band gap. Each structure was investigated using methods mentioned above.

The reliability of reflectance spectroscopy was investigated. It was found that in certain cases, a continuum of structural parameters yield reflections that match photonic band structure calculations. Methods to improve this situation are discussed. When applied to titania inverse opals, it was found that the refractive index could be determined to ±0.05 and the volume fraction to ±0.5%. Accurately determining the refractive index

of inverse opals is useful in estimating the refractive index of other PCs made from the same sol-gel.

Calculation of the DOS using a combination of MIT's photonic bands package and house-written software was applied to biotemplated photonic crystals. It was found that even partial band gap photonic crystals can greatly modify the DOS.

Finally, the rate of spontaneous emission of quantum dots embedded in photonic crystals was measured to indirectly probe the DOS. Three different models were used to extract the lifetime from radiative decay curves. It was found that a log-normal distribution of lifetimes was the most meaningful model. The radiative lifetime of quantum dots embedded in titania photonic crystals replicated from *Lamprocyphus augustus* was modified by up to a factor of ten, an amount unprecedented in the photonic crystal literature.

For Katie, Portia, and Atticus

TABLE OF CONTENTS

ACKNOWLEDGEMENTS

I express my sincerest gratitude for Dr. Michael Bartl, my advisor and mentor for encouraging me to be the best that I can be. Over my years in graduate school Mike taught me what it means to conduct world-class research, encouraging me to do experiments that I didn't want to do because it was the right thing to do. Mike held me to the highest ethical standard through example, leaving a deep impression.

I heartily acknowledge the hand of Dr. Jeremy Galusha in this work. Jeremy was my first contact when I was investigating graduate schools. His kind response to my emails was a factor in my decision to attend the University of Utah to work in the Bartl group. Jeremy and I worked closely together during my first two years, during which time he became a trusted coworker, mentor, and friend. Most of the work reported in this thesis I started with Jeremy or is built upon his pioneering research.

The other members of the Bartl group, especially Dr. Jacqueline Siy-Ronquillo, Moussa Barhoum, Tommy Terooatea, Mike Dahlby, and Benjamin Yonkee, have provided invaluable discussion and feedback. I thank my graduate school classmates Douglas Kreich, Nikka Bradely, Alexis Crawford, and Krystal Brown for their continual support and friendship. Outside of the University of Utah, I thank my Fall 2011 Physical Chemistry class at Southern Utah University for their patience with my first attempt at teaching while finishing this thesis. I thank my Father for teaching me integrity, my late

Mother for giving me a chemistry set and telescope as a child, and my siblings for their support.

Finally, this thesis would not have existed without the unconditional support of my loving wife. Katie took a huge risk marrying me 10 years ago, before I had even earned my high school diploma. She worked as a cashier at a fast food restaurant to put me through college, then managed apartments and took care of our kids through graduate school, and now has tolerated my nearly continuous absence from home during my first semester teaching at Southern Utah University.

I would like to thank the Royal Society of Chemistry [Reproduced with permission of the Royal Society of Chemistry (Jorgensen & Bartl, *J. Mater. Chem.* **DOI:** 10.1039/C1JM11037C). Copyright 2010 The Royal Society of Chemistry] for some of the material in Chapter 2. I thank Elsevier [Reprinted with permission of Elsevier (Jorgensen, Yonkee, and Bartl, *Scripta Mater.* **DOI:** 10.1016/ j.scriptamat.2011.08.018) copyright 2010 Elsevier] for some of the material in Chapter 2. I thank the American Physical Society [Reproduced with permission of the American Physical Society (Jorgensen, Galusha, and Bartl, *Phys. Rev. Lett.* **DOI:** 10.1103/ PhysRevLett.107.143902) copyright 2010 The American Physical Society] for some of the material in Chapter 5.

CHAPTER 1

INTRODUCTION

Photonic Crystals

Many of the most important technologies of the 20th century, from lasers to fiber optics and solar cells, rely on control over light. Using what is now considered conventional optical ideas – a resonant cavity, total internal reflection, and antireflective coatings – these technologies have impacted all of our lives. While improvements are still being made in laser technology, optical communication, solar cells, and information processing, the limit of what is possible using 20th century technology appears to be rapidly approaching.

Looking forward to the future, methods to exercise a greater control over light are necessary. The ability to slow light could revolutionize solar technology[1-4] and photocatalysis.[5] Being able to trap a photon with an emitter, creating a photon-emitter bound state, is the foundation for quantum computing, the qubit.[6-7] Of course, if qubits are to be used light needs to be routed to and from the bound states in an optical circuit. Control over spontaneous emission would dramatically lower the threshold energy for lasers and allow cavity-less lasing.[8-10] Motivated by these challenges, and the potential impact of overcoming them, researchers have sought materials that can control light in revolutionary ways similar to the control semiconductors allow over electrons.

Originally proposed in the late 1980s photonic crystals are a promising new concept predicted to allow control over the propagation of light as well as spontaneous emission.[11-12] Only in the past decade have many of these predictions been experimentally verified in the microwave and infrared.[13-14] Very recently, researchers in the Bartl group have been taking inspiration from nature to create and test photonic crystals that control visible light to an unprecedented degree.[15-19]

Biomimetic Photonics – the Intersection of Chemistry, Physics, and Biology

Photonic crystals are optical nanostructured materials with a refractive index periodic on the order of the wavelength of light they interact with. Within a photonic crystal, Bragg scattering events lead to direction and frequency dependent dispersion relations. Borrowing terminology familiar to semiconductor physics, these special materials have directional photonic bands and stop gaps, as well as (under certain conditions) full photonic band gaps.[4, 11-12] Photonic band gaps offer an unrivaled control over light, and are the foundation of several new optical concepts such as low-threshold light amplification through control of spontaneous emission, slow-light enhanced photochemistry and catalysis, and quantum computing.[9, 20-22]

Studied independently of each other, great progress has been made in the study of photonic band gap crystals, materials chemistry, and structural coloration in nature. Only recently, however, a true cooperation between these disciplines has blossomed into the new field of biomimetic and biotemplated photonic crystals – the study of which exists at the intersection of biology, physics, and chemistry. As a result of this cooperation, great

progress has been made towards the creation and integration of next-generation technologies relying on an enhanced control over light.

This thesis focuses on this new field of biomimicry in photonic materials design and characterization. In the remainder of this chapter, an overview of photonic structure engineering in biology will be given, followed by an introduction on the physics of photonic band gap materials, recent progresses in man-made photonic crystals (and current limitations), and the potential of bioreplication for creating novel photonic structures, inaccessible by purely synthetic engineering routes. Finally, the contributions from different disciplines will be woven together into a unified picture of photonic crystals inspired by – or derived from – biology.

The second chapter will provide details on the conversion of organic photonic crystals into a variety of inorganic structures, addressing various challenges to the replication process. Chapter 3 will describe the characterization processes used to better understand both natural and synthetic photonic crystals. Density of optical states, that critical property that connects emission behavior of a photon emitter with its environment, will be discussed in Chapter 4 in connection with theoretical studies on several photonic crystals. In Chapter 5, modification of the rate of spontaneous emission by photonic crystal samples will be demonstrated to an unprecedented degree. Finally, experiments currently underway and ideas for the future will be reviewed along with concluding remarks in Chapter 6.

Structured Materials in Biology

Nature has developed interesting ways to overcome material challenges. Unlike lab conditions, where extremes in temperature, pressure, and pH are possible to achieve a synthetic goal, living systems produce a remarkable diversity of structural materials under ambient conditions.[23-25] Examples of such structure-function relations are found throughout the world of biology from those giving stature and motion, like bones and muscles, to those with special sensory functions like the human eye. The unsurpassed elegance of evolutionary engineering in nature is found only if examined close enough. For example, in the sponge Euplectella sp. silica nanometer-scale spheres are packed into sheets that are laminated together by organic material into cylindrical spicules. The cylinders are arranged in a square lattice, cemented together at the nodes with silica, complete with struts. The design overcomes the inherent brittleness of the material, glass, while avoiding "over engineering" the structure with redundant features.[24] Figure 1.1 shows the beautiful hierarchal structure employed by Euplectella to overcome a complex structural problem. Nature produces a variety of mineralized materials, some multifunctional and others specifically tailored to a purpose. The structure-function relationship of many of these has been explored, and certain structures like the crossed lamellar of highly twined aragonite have been observed widespread in phylum of invertebrates.[23] Mechanical stability in spite of unique challenges is not the only triumph of structural materials in biology.

Nanostructured materials have also been used by biology to produce a vast palette of structural colors using interference, scattering, and diffraction effects.[26] Structural colors have been found across the spectrum of biology in plants, marine life, birds,

insects, and some mammals.[15, 27-38] Figure 1.2 shows four examples of structural color across biology. In the marine world, octopus, squid, and cuttlefish (cephalopods) have an impressive ability to camouflage and signal using body pattern and skin color, which can change almost instantaneously. The patterning results from pigmented cells, structural reflectors, or any combination of both and it is the physiological ability to change these cells that allows such a wide variety of dynamic optical effects, as illustrated in Figure 1.3. It is speculated that the colors produced by multilayer reflector cells, which change with viewing angle, are used to guide schools of cephalopods and frighten predators. At oblique angles, the reflector cells also polarize light, which may be further useful in specialized communication because cephalopods have a keen ability to detect polarized light. The exact method by which the reflector cells change their color is yet unknown, however it is hypothesized that a change in protein state (with accompanying change in refractive index) and interlayer spacing could cause the effect.[27]

Biological structural colors have been developed for a variety of reasons, ranging from camouflaging to frightening predators and attracting mates.[39] This requires an array of optical effects: From strongly iridescent to near angle-independent coloration, from shimmering bright to matte hues, from vivid to pastel-like colors and various combinations thereof. Moreover, biological photonic structures were optimized to operate under various illumination conditions; while many species create their optical effects in bright sunlight, others operate under highly scattering conditions produced by water-droplets and wet leaves in rainforests. Others have to function under dim illumination at the forest floor or within dense vegetation. These different applications, optical effects, and

environmental conditions have led to a diversity of photonic structures in biology that is virtually limitless. The structures range from simple one-dimensional multilayers of biopolymeric layers with slightly different refractive indices,[40-41] to two-dimensional lattices composing the internal structure of skeletons and hairs of sea animals[42-43] and feathers of several species of birds,[37, 44-45] and to various three-dimensional architectures.[15, 36, 46-51] The latter can be found within colored cuticle scales of many species of beetles (Coleoptera) and butterflies (Lepidoptera) in form of quasi-periodic arrangements, chiral, honeycomb and nonclose-packed ball-stick structures, as well as various cubic lattices, including gyroid and diamond-based geometries (Figures 1.4 and 1.5).

This large variation in crystal structure symmetries, lattice constants and dielectric volume fractions dramatically extends the currently available "synthetic" photonic crystal structures. While the direct use of biological structures for optical applications is limited since they are composed of biopolymeric compounds with rather poor mechanical, heat and photo stability, they provide intriguing templates. From a materials viewpoint, biological structures are therefore similar to synthetic polymeric photonic crystal templates created by direct ink writing, laser writing, holography, or colloidal self-assembly, as discussed in Chapter 1. Also in these examples, the fabricated polymeric structures have to be converted into inorganic replicas by infiltration with various precursor compounds. Consequently, infiltration methods successfully used to produce replicas of synthetic templates such as atomic layer deposition, low-temperature evaporation techniques and sol-gel chemistry-based routes can also be applied to replicate biotemplates.

Since biological photonic structures are integrated into larger body parts (feathers, wings, hair, exoskeleton) they often require preinfiltration processing steps. For example, in contrast to the free-standing, open and easily accessible lattice frameworks of most synthetic template structures, biological photonic structures are often buried, hidden, or embedded within a structure-less matrix. This is particularly true for photonic structures of most butterflies and beetles, which are contained in wing and exoskeleton scales and are thus partially or completely surrounded by an impermeable biopolymeric shell (see also Figure 1.4).[16, 35-36] For successful infiltration/replication it is therefore important to provide access to the interior photonic structures by cutting or microtoming part of the shell-like biopolymer. In addition, many biopolymeric scales and hairs are covered with a hydrophobic, wax-like film. Since this layer can prevent wetting of the photonic structure, in some templating methods it has to be removed by treatment with organic solvents or acids.

One specific example of structural color in nature is of particular relevance to this thesis: coloration in cuticular scales of certain beetles and weevils, especially *Lamprocyphus Augustus* which has been studied by the Bartl group in detail.[35, 49] *L. Augustus* lives in the rainforests of Brazil, and is bright, shimmery, iridescent green in color. Its coloration likely had the evolutionary advantage of camouflaging it among the wet undergrowth, while simultaneously keeping it cool by reflecting the most intense part of the solar spectrum.[39] Looking closer, it is found that the insect's color comes from epidermal scales attached to its exoskeleton, and within these scales an elegant three dimensional patterning. Figure 1.4 shows *L. Augustus*, and "zooms in" to show that the

coloration comes from exoskeletal scales, and that the scales contain patterning. By taking 30 nm thick slices of the scales using a focused ion beam and imaging each slice, Galusha et al. were able to digitally reconstruct a portion of the scale, finding the pattern to be a face centered cubic lattice with intersecting cylinders oriented in the [1,1,1] crystal direction, a so-called diamond-based lattice.[49] They found that the lattice constant was such that Bragg diffraction from the myriad interfaces resulted in green light being constructively reflected from the scale, while destructively interfering inside, in other words it was shown to be a prime example of a natural photonic crystal.

Theoretical Background of Photonic Crystals

Light traveling through a nonhomogeneous transparent dielectric medium has partial reflections at each of the interfaces of differing refractive index components. If the arrangement of these interfaces is periodic, these multiple reflections can constructively or destructively interfere with each other leading to frequency ranges, which are absent within the material and other ranges that are enhanced.[4, 11-12] The frequencies of light sustainable in photonic crystals are called photonic bands, and can be found from the macroscopic Maxwell equations (cast as an eigenvalue problem) using methods analogous to the variational principle of quantum mechanics.[52] Using a plane wave expansion approach and the variational principle, Johnson and Joannopolous developed a method to calculate the allowed frequencies in a photonic crystal.[53-54]

Briefly, if it is assumed that the field strengths are small enough that second order optical effects are negligible, the material is isotropic, that the dielectric constant is independent of the frequency in the region of interest, and that the material is transparent

(the dielectric constant is real and positive) then Maxwell's equations expressed in the magnetic field, ***H(r)***, can be cast as an eigenvalue problem (equation 1.1) where $\varepsilon(\boldsymbol{r})$ is the spatially dependant dielectric constant, ω is the frequency, and c is the speed of light.

(1.1) $$\nabla \times \left(\frac{1}{\varepsilon(\boldsymbol{r})}\nabla \times \boldsymbol{H}(\boldsymbol{r})\right) = \left(\frac{\omega}{c}\right)^2 \boldsymbol{H}(\boldsymbol{r})$$

Once equation 1.1, is used with the variational method to find the magnetic component, the electric field is easily found through equation 1.2 where $i = \sqrt{-1}$ and ε_0 is the vacuum permittivity.

(1.2) $$\boldsymbol{E}(\boldsymbol{r}) = \frac{i}{\omega\varepsilon_0\varepsilon(\boldsymbol{r})}\nabla \times \boldsymbol{H}(\boldsymbol{r})$$

Similar to the operators familiar in quantum mechanics, the operator in equation 1.1, $\widehat{\Theta}$, is linear and Hermitian. As a result, the solutions are orthogonal. The smallest eigenvalue ω_0^2/c^2 is the minimum of equation 3 over all conceivable field patterns (given by $\boldsymbol{H_0}$), the next smallest eigenvalue minimizes equations 3 over the subset of fields orthogonal $\boldsymbol{H_0}$ and so on.

(1.3) $$U_f(\boldsymbol{H}) \triangleq \frac{(\boldsymbol{H},\widehat{\Theta}\mathbf{H})}{(\boldsymbol{H},\boldsymbol{H})}$$

By solving equation 1 for the first few eigenvalues over the principle directions in the photonic crystal, the allowed frequencies within the crystal are collected and can be summarized in a photonic band diagram. The bulk of the work in calculating photonic bands has been written into MIT's Photonic Bands software package (MPB)[53] by the aforementioned Johnson and Joannopolus. MPB was used extensively in this work, in investigating and characterizing photonic crystals as well as in conjunction with house-written software for the calculation of the density of optical states.[19]

The physical origin of photonic band gaps can be understood by making analogies to concepts familiar to solid state physics. Since light inside a photonic crystal is considered as a plane wave interacting with a periodic dielectric, the electric/magnetic fields can be thought of as Bloch states having a wavevector $\boldsymbol{k}$. In this case, wavevectors (and their associated frequencies) that differ only by a multiple of $2\pi/a$ are identical. It follows that only wavevectors over a limited range need to be considered – called the Brillouin zone. In a one-dimensional photonic crystal (or Bragg stack), the Brillouin zone spans $-\pi/a$ to π/a and photonic band gaps occur at the edge of the Brillouin zone, where $|\boldsymbol{k}| = \pm\pi/a$.

In general, for each allowed value of $\boldsymbol{k}$, there are two equally valid wave functions for the light given by a sine and a cosine function. For most values of $\boldsymbol{k}$, these solutions are degenerate because the energy density of the light in both solutions is equally distributed in both high and low dielectric parts. However when $|\boldsymbol{k}| = \pm\pi/a$, the wavelength of light is equal to $2a$, and the sine and cosine solutions are no longer degenerate. In one case, the electric field maxima are located in the high dielectric, with nodes in the low, a situation that is energetically favorable – this is called the dielectric band. In the other case, field maxima are located in the low dielectric regions (typically air), a situation that is energetically unfavorable compared to the previous – this is called the air band. Figure 1.6 illustrates both of these situations. The difference between the energy/frequency of the dielectric band and the air band is the photonic band gap.[54] There is no value of $\boldsymbol{k}$ that leads to a frequency within a band gap. To extend this idea into three dimensions, each direction is considered as a one-dimensional problem and all the important directions in the crystal can be spanned by following the edges of the three-

dimensional Brillouin zone. Since the origin of the photonic band gap arises from the difference in energy imposed by the concentration of field energy in high and low dielectric parts, it follows that the dielectric contrast of the two parts is of critical importance in photonic crystal problems. For a photonic crystal to operate in the visible, if follows that it is required that the dielectric constant of the material be as high as possible, while still remaining transparent. This final requirement, as well as crystal characterization is a challenge well addressed by physical chemistry.

Materials Chemistry Aspect of Photonic Crystals

To date, tremendous progress in photonic structure engineering has been made in the microwave and infrared regimes. Using top-down microfabrication and bottom-up colloidal self-assembly techniques, various three-dimensional photonic crystal structures have been synthesized with complete band gaps at infrared frequencies.[14, 55-62] In contrast to the successes in the infrared regime, complete photonic band gaps at visible frequencies have proven elusive due mainly to difficulties in creating efficient three-dimensional photonic lattices with feature sizes in the hundred-nanometer range. In the following section the fabrication strategies for photonic crystals operating in the infrared and visible regimes will be reviewed. Then, the advantages and limitations of different top-down and bottom-up fabrication techniques focusing on attainable feature sizes, crystal lattices, and high-dielectric compounds will be discussed.

The fabrication of photonic band gap crystals operating at infrared frequencies has benefited tremendously from powerful microprocessing techniques that have been optimized in the semiconductor industry during the last 50 years. These techniques can

generally be classified into direct and indirect methods. In the former, a desired photonic crystal structure is formed directly out of a high-dielectric semiconductor compound. For example, Lin and coworkers used a comprehensive multilevel stacking process consisting of a repeated deposition, lithographic patterning, and etching to successfully fabricate dielectric woodpile (a diamond-based lattice structure) photonic crystals with band gaps in the infrared regime.[55] Subsequently, Noda et al. developed a wafer-fusion-based method to create woodpile structures made out of GaAs with a complete band gap at near infrared wavelengths,[56] whereas Johnson, Joannopoulos and coworkers designed and fabricated a nine-layer photonic crystal with a wide (up to 25% gap-to-mid-gap ratio) band gap out of silicon by sequential layer-by-layer scanning-electron-beam lithography.[59]

A common disadvantage of these direct methods is that fabrication of high-quality three-dimensional photonic crystals is very time consuming, expensive, and is generally limited to only a few layers. Indirect methods, on the other hand, use a template structure created out of inexpensive polymers. This structure serves as a sacrificial mold for templating high-index compounds such as silicon or germanium. Successfully applied methods to create such polymeric photonic crystal template structures, including the highly efficient diamond-based woodpile lattices, are multibeam holography, multiphoton lithography, and direct laser writing methods.[62-64] An interesting alternative to these light-patterning routes is the direct ink writing method originally developed by Lewis and coworkers.[65-66] In this technique, a cylindrical filament approximately 1 mm in diameter is formed by the deposition of a fluidic polyelectrolyte/water ink into an alcohol-rich reservoir. Braun, Lewis and coworkers demonstrated that this filament can then be

patterned in a layer-by-layer sequence to build a woodpile structure with photonic crystal feature sizes in the near infrared region.[61, 67]

All of these polymeric templates can then be converted into high-dielectric photonic crystals made out of silicon or germanium. Since the polymeric templates would not withstand the high deposition temperatures required for typical semiconductor deposition techniques such as chemical vapor deposition, they are first protected by a metal oxide (silica or alumina) coating formed by atomic layer deposition. For example, Ozin and coworkers showed that depending on the amount of metal oxide deposition (complete backfilling or deposition of a thin coating) it is possible to create high-dielectric photonic crystals in the form of a positive replica or an inverse of the original template structure [64, 70].[62, 68] While a silicon double inversion procedure produced a woodpile photonic crystal with a complete (up to 9% wide) band gap in the infrared,[68] region Hermatschweiler et al. showed that silicon inverse woodpile photonic crystals with more than a 14% wide complete band gap centered at a wavelength of around 2.5 mm can be fabricated by a silicon single inversion method.[62] Braun, Lewis and coworkers used a similar – although independently developed – technique to convert direct ink-writing-created woodpile templates into germanium photonic crystals with wide (up to 25%) complete band gaps centered at a wavelength of around 6 mm.[61]

An interesting – fast, simple, and low-cost – alternative to these rather labor-intensive routes is colloidal self-assembly.[69-71] In this bottom-up photonic crystal fabrication technique, monodisperse microspheres are deposited onto planar substrates by self- or directed assembly in close-packed face-centered cubic or hexagonally close-packed colloidal crystals (also called artificial opals, since these colloidal crystals closely

resemble the microstructure of natural opal gemstones). Figure 1.7 shows an example of synthetic opal where the number of deposited layers of spheres was carefully controlled. Similar to the indirect methods described above, these colloidal crystals are then used as templates and are infiltrated with an infrared-transparent high-dielectric component. After selective removal of the opal template a so-called inverse opal photonic crystal (a close-packed face-centered-cubic lattice of air spheres in a high dielectric material) is obtained.[72] While inverse opal photonic crystals are less effective (i.e., less efficient in affecting and controlling the propagation of light) than diamond-based lattices, it was shown that the formation of a complete photonic band gap is possible provided the high-dielectric material has a refractive index of 3 or higher versus air as the low-dielectric component.[73] Using polycrystalline silicon as the high-dielectric component (with a refractive index of 3.2–3.4), John and coworkers[14] and Norris and coworkers[57] successfully fabricated inverse opal photonic crystals with a complete band gap in the near infrared region.

Compared to the enormous progress achieved in fabricating photonic crystals operating in the infrared region, photonic structure engineering in the visible region is far less advanced – due mainly to the difficulties in shaping visible light-transparent, high-dielectric materials into efficient morphologies with periodicities at visible wavelengths. Unlike infrared photonic crystals with complete band gaps of up to 20–30% gap-to-mid-gap ratios,[55-61] enabled by infrared-transparent materials with refractive indices of 3.2 and higher, the lack of visible light-transparent dielectrics with comparable refractive indices embosses an enormous challenge for achieving complete band gaps at visible wavelengths.

In spite of these challenges, recent technological advances and discoveries have provided promising steps forward toward the goal of a synthetic full band gap photonic crystal operating in the visible. While not yet reaching the visible, top-down techniques continue to improve. New self-assembly techniques add variety and control over the structures available.[74-76] Looking for an alternative to very expensive and time consuming top-down methods, and seeking to be free from the limits of colloidal self-assembly, researchers have looked for inspiration from nature. Biotemplated and bioinspired photonics represent two focuses in this effort. First, natural photonic crystals and samples templated from them are being studied to assess their potential usefulness and provide insight into experimental structure/photonic property relationships.[15-19, 35] Second, the self-assembly of biomolecules in nature is being studied in hopes that once understood, they may be mimicked. Both focuses present significant material chemistry and analytical challenges.

Many biological photonic structures, including those found on the exoskeleton of beetles, are made of chitin[36, 47] (a biopolymer mixed with a cocktail of proteins) and are enclosed in a cuticular scale that is on the order of tens of micrometers in diameter.[34, 77] Since chitin has a relatively low refractive index and is autofluorescent, it is not amiable to spectroscopic study. To have experimental access to their otherwise unobtainable structures, inorganic oxide materials have been patterned with biological photonic crystals as templates using atomic layer deposition,[78-80] low temperature evaporation techniques,[81-83] and sol-gel chemistry.[84-87] Atomic layer deposition and evaporation techniques produce well-controlled shell-like copies, but require an open structure (such as those found on butterflies) and produce mainly shell-like replicas. Sol-gel chemistry is

a flexible alternative, shown to fill structures with even just a small opening.[15-17] By modifying the types of sol-gel compounds used along with their processing parameters, a variety of hollow and solid structures may be made.[88] This flexibility, taken with the abundance of natural photonic structures available, has allowed researchers to experimentally probe a wide variety of photonic structures that are otherwise unavailable, gaining knowledge useful in the future design of photonic crystal systems. While parameters must be optimized for biological photonic crystals coming from different species, there is a general sol-gel processing method that is discussed in detail in Chapter 2. The biotemplating method consists of removing the scale from the insect's exoskeleton by scraping them along the edge of a glass substrate or razor blade (a process that usually breaks them open), pretreating the scales with acid, and sol-gel infiltration between two slides. The biological template can be removed using acid digestion or thermal degradation in a muffle furnace. Depending on the desired outcome, the negative copy may be used in the same process again.

Deposition and Evaporation-Based Biotemplating Methods

Low-temperature atomic layer deposition is an excellent method for creating inorganic shell-like replica of biological photonic structures.[78-80] It combines a noncorrosive reaction environment and mild *pH* conditions with relatively low deposition temperatures of around 100-200 °C. Furthermore, since the infiltrated compound is formed by a layer-by-layer atomic deposition process, the degree of infiltration can easily be tuned by controlling deposition cycles. The precursors used

are in general gaseous compounds and therefore readily infiltrate even complex three-dimensional frameworks as long as the internal structure is fully accessible. Since the majority of photonic structures found in the wings of butterflies are open frameworks and require no or very little preinfiltration cutting, they are the templates of choice for most successful atomic layer deposition-based bioreplication attempts.

For example, Wang and co-workers created alumina replicas of the photonic structure of wing scales from the butterfly *Morpho peleides* by atomic layer deposition.[78] Using a low-temperature atomic layer deposition process at 100 °C and trimethyl aluminum ($Al(CH_3)_3$) and water as precursor sources, the biopolymeric photonic structure of *M. peleides* was coated with a layer of amorphous alumina. The thickness of the alumina coating was gradually increased by about 10 nanometer steps until a final thickness of 40 nanometers was achieved. Characteristic of photonic crystal structures, the infiltration process can be monitored and precisely controlled by analyzing the color of the reflected light. As shown in Figure 1.8a, a red-shift (from blue to pink) of the reflected light was observed due to a change in periodicity and effective refractive index of the composite as the thickness of the coating increased. When a desired layer thickness was obtained, the biopolymeric/alumina composite was heated to 800 °C in air. Under these conditions, the butterfly template completely decomposes by pyrolysis and the resulting structure is a shell-like copy of the original *M. peleides* photonic lattice made out of polycrystalline alumina. Scanning electron microscopy images are given in Figure 1.8 and show that even nanoscale structural features of the original

biotemplate were preserved by this process. Furthermore, optical reflectance spectroscopy studies revealed alumina replica features very similar to that of the original butterfly scales in terms of reflection peak wavelength position and shape.

Gaillot *et al.* developed a similar atomic layer deposition route to fabricate biotemplated organic-inorganic composite photonic crystal structures.[79] In their approach, the photonic scales covering the wings of the green swallowtail butterfly *Papilio blumei* were used as biological templates. The scale's exterior and the interior photonic structure were covered with titania *via* low-temperature atomic layer deposition. The intra-scale deposition of titania was enabled by diffusion and subsequent deposition of the gaseous titania precursors through surface cracks created by razor blades or sharp tips. Gaillot *et al.* also conducted detailed structural and optical studies on these organic-inorganic replica types.[79] Experimental results were compared to theoretical modeling and band structure calculations and provided valuable insights regarding the ability to tune the optical properties of these photonic crystals through slight variations of the deposited high-dielectric compound. In addition, analyses of the properties of these oxide-replica butterfly wings indirectly provided new insights into their structural complexity; with various intersecting nano-channels and connected chambers in addition to the photonic crystal structure.

A successfully applied evaporation-based biotemplating method is the so-called conformal-evaporated-film-by-rotation technique developed by Lakhtakia and co-workers.[81-83] This method, which evolved from the oblique angle deposition technique, combines thermal evaporation with simultaneous substrate tilting and

rotation in a low-pressure chamber. Since the reaction chamber pressure is in the micro*torr* regime, the evaporation/deposition process can be performed at low temperatures and under a noncorrosive environment, providing excellent conditions for replicating sensitive biological structures. Additionally, the high-speed rotation of the biological templates during the evaporation process facilitates formation of a homogeneous and dense inorganic film, even on highly curved and structured surfaces. Using this technique, the structures found in the wings of various butterflies were successfully replicated, including micro- and nanometer features of the photonic framework.[81, 83]

Sol-Gel Chemistry-Based Biotemplating Methods

Sol-gel chemistry is an interesting alternative to deposition and evaporation methods. While the latter allow to precisely control the degree of infiltration on an atomic scale, sol-gel methods are attractive for their simplicity enabled by flexible processing parameters.[89] In addition to being simple, fast and inexpensive, sol-gel methods extend the variety of accessible templated structures from shell-like positive replicas usually obtained by deposition methods to solid negative copies (inverse replicas) and further to solid positive copies (true replicas). However, to produce bioreplicas of high quality, some inherent problems of sol-gel chemistry have to be overcome. The most important of which are structural shrinkage, crack-formation and introduction of nanoporosity during the various sol-gel process steps, such as solvent evaporation, framework solidification and heat-induced crystallization. Moreover, since these steps depend also on the nature of the

biological template (e.g., geometry and accessibility of the photonic structure, mechanical stability of the framework, hydrophilicity of the biopolymeric compounds), the sol-gel parameters often have to be fine-tuned and optimized on a case-by-case basis. As will be discussed in the following, among sol-gel reactions certain infiltration and processing conditions are of particular importance: the precursor components and solvents, the sol composition and concentration, the post infiltration conditions such as drying time and humidity during the gelation process, and temperature and time of heat treatment.

Similar to evaporation and deposition approaches, the majority of sol-gel biotemplation attempts have focused on replicating the open-framework photonic structures found in the wing scales of various colored butterflies. For example, Zhang and co-workers created titanium and zinc oxide replicas from the wing scale's of the butterflies *Papilio paris* and *Thaumantis diores*.[84-85] The scales were infiltrated with ethanol solutions of titanium or zinc salts followed by heat treatment at 500 °C in air to induce crystallization of the oxide framework and removal of the biopolymeric template. Despite structural shrinkage during the heat-based framework densification-crystallization treatment, the replicated materials displayed optical band structure features in the blue-green region and could be used for solar cell and light emission applications. For example, titania replica were used as photoanodes with enhanced light harvesting efficiencies under visible-light illumination.[84] On the other hand, the patchy blue and black colored wing scales of *P. paris* replicated into zinc oxide have interesting room-temperature cathodoluminescence properties.[85] The same group also synthesized copper-doped

tungsten oxide replica of the wing scales of the butterfly *Euploea mulciber* by a similar sol-gel method (Figure 1.9). These replica showed enhanced gas sensing ability with a high selectivity for trimethylamine at concentrations as low as 0.5 ppm at 290 °C.[87]

An interesting variation of sol-gel biotemplating is the incorporation of sonochemistry reported by Zhu *et al*.[86] In this method, the internal biopolymeric nanostructure of blue-colored wings from *Morpho* butterflies was impregnated with an ethanol-water-based metal precursor solution followed by high-intensity ultra-sonication for several hours at room temperature. After sonication, the composites were heat-treated to remove the biopolymeric template, leaving behind replicas made from silica, titania and tin dioxide. All of the replicated samples possessed photonic nanostructures, which highly preserved the original butterfly wing structures and displayed optical reflectance features in the visible. Also in this work, it was found the nanocrystalline replica could be used as a gas sensor. For example, tin dioxide replicas displayed high sensitivity for ethanol vapor with a fast response time (8 seconds) and a short recovery time (15 seconds).

In addition to replicating the open-scale structures of butterfly wings, Bartl and co-workers showed sol-gel chemistry is also very effective for templating photonic lattices enclosed in the biopolymeric shells typically found in beetle exoskeletons.[15-16] Two fabrication steps were found to be critically important: precursor infiltration and complete removal of the entire biopolymeric template (interior photonic structure and surrounding shell). For the infiltration step, the liquid nature of sol-gel precursor has proven very useful. Small openings of the

scale, which can be created by cutting with a razor blade, are sufficient to infiltrate the entire internal photonic framework with a liquid silica-based precursor by capillary forces. Regarding the template removal, the commonly used pyrolysis method (heat treatment under oxidative conditions at temperatures between 300 and 500 °C) failed to produce high-fidelity replica. While this method is very effective in complete removal of the biopolymeric template, it also causes significant structural damage and depending on the thickness of the surrounding shell can lead to the complete destruction of the interior photonic framework.

To overcome this obstacle, Galusha *et al.* developed a low-temperature biopolymer acid-etching technique.[16] Treating the infiltrated composite with a mixture of concentrated nitric and perchloric acid led to the complete removal of the biological template while greatly reducing cracking and structural damage of the silica-based replica framework. Furthermore, since the acid treatment does not require high temperatures, shrinkage of the replicated framework is greatly reduced as compared to pyrolysis methods and can be as low as 5%. The same authors also showed the structural stability of the replica is further improved by using a hybrid organic/inorganic silica sol-gel precursor. The organic component of this SBA-type hybrid material, originally developed by the Stucky group,[90] provides some structural flexibility and aids in releasing structural stresses during the drying/gelation process. These refined sol-gel biotemplating conditions with reduced cracking and lattice shrinkage are promising steps towards photonic crystals with finely tuned band structure properties. In particular, keeping lattice shrinkage (which is accompanied by a frequency-blue-shift of the photonic band

structure features) to a minimum is important for applications that require band gaps at particular frequency ranges in the visible.

The final part of this chapter will discuss how such optimized sol-gel methods can be applied towards the fabrication of photonic crystals with a complete band gap at visible frequencies—a type of optical material that is still not achievable by any other engineering technique.

Experimentally evaluating the quality of biologically derived photonic crystals is a challenge due to their strong deviations from the idealities of photonic crystal theory which assume an infinite, defect free, surface free, and isotropic structure. Due to their small size, surfaces are a significant part of biological photonic crystals. Focused ion beam analysis has revealed that within a given scale, pixilated crystal domains exist oriented in different directions,[35] and the interfaces between these domains are defect planes. Quantifying the effect these nonidealities have on photonic crystal properties is currently being researched. However, even with the described defects, unprecedented photonic effects have been measured in biotemplated samples,[18] an encouraging result that has provided motivation and insight into future photonic crystal work.

Four techniques are typically used to characterize biotemplated photonic crystals. Microreflectance spectroscopy provides a first qualitative look at photonic crystal quality. Since photonic band gaps prevent frequency ranges of light from propagating within a photonic crystal in one or more directions, incident light within the band gap range is reflected. Scanning electron microscopy (SEM) of crushed samples provides the most direct measurement. From SEM images, the lattice constant, structural feature sizes, and approximate filling fraction are determined. Using SEM measurements, a three-

dimensional computer model of the structure is created that can be used with MPB software to calculate the photonic bands of an idealized version of the structure. The same computer model is used with house-written software in conjunction with MPB to calculate the density of optical states. The density of optical states is essentially a relative count of the number of optical modes available within a photonic crystal as a function of frequency.[73, 91] An example of calculated density of optical states using our method is included as Figure 1.10. For comparison, an approximation of the quadratic density of optical states behavior for a homogenous material with comparable effective dielectric is also included. Since the rate of spontaneous emission is proportional to the density of optical states according to Fermi's Golden Rule,[92] light sources embedded within photonic crystals emitting with a frequency in the range of reduced density of optical states exhibit an inhibition of spontaneous emission. The effect density of optical states has on spontaneous emission was experimentally verified to an unprecedented magnitude using quantum dots as the light source, a key result of this thesis that highlights the quality, flexibility, and future utility of diamond based photonic crystal structures. While researchers have yet been able to produce a fully synthetic diamond-lattice photonic crystal in the visible, the Bartl group has had access materials derived from biological systems that enabled these experiments thanks to the progress made in biotemplating methods.

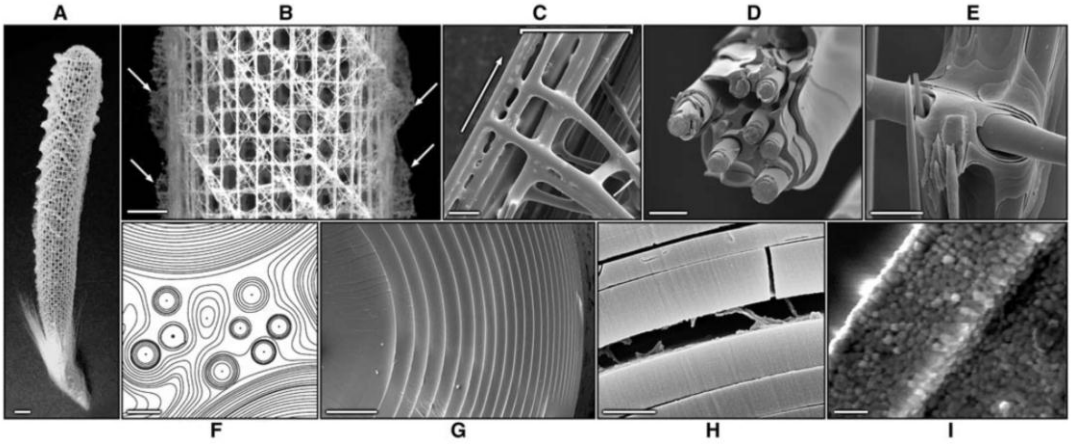

Figure 1.1. The mineralized skeleton of *Euplectella sp.* shown at larger magnifications from a to i. (a) Photograph of the entire skeleton, scale bar 1 cm. (b) Fragment of the cage showing the square grid lattice with cross beams, scale bar 5 mm. (c) SEM showing that each beam is composed of bundled spicules, scale bar 100 μm. (d) SEM of broken individual spicule revealing its internal structure, scale bar 20 μm. (e) Partially HF etched junction area showing that the lattice is cemented with silica, scale bar 25 μm. (f) Contrast enhanced SEM revealing the internal organization of the spicules, scale bar 10 μm. (g) SEM of individual fiber in spicule, scale bar 5 μm. (h) SEM of a fractured fiber layer showing organic interlayer glue, scale bar 1 μm. (i) High resolution SEM of the biosilica surface revealing its consolidated nanoparticle nature, scale bar 500 nm. Adapted from Ref. 24, reprinted with permission from AAAS.

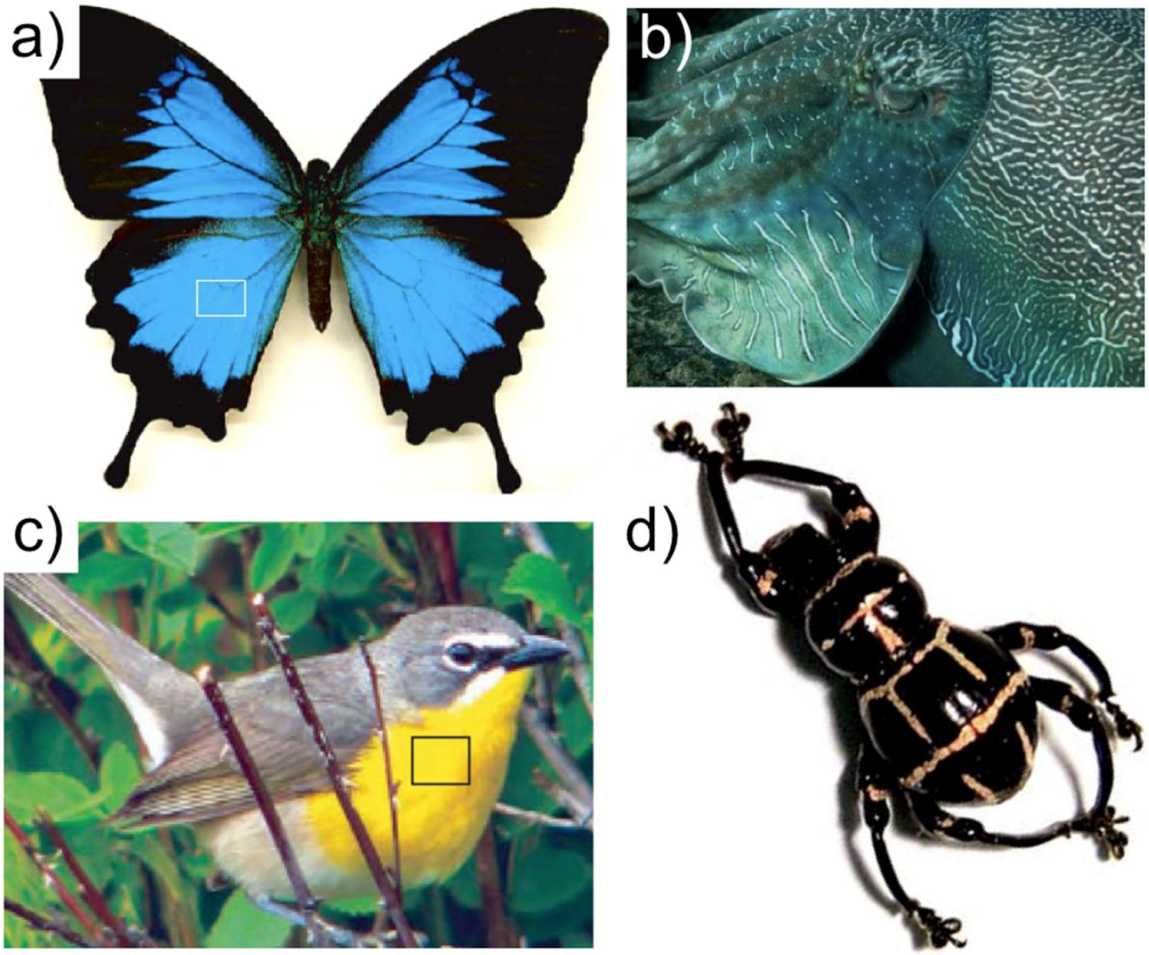

Figure 1.2 Photographs of structural colors in (a) the wings of the butterfly Papilio ulysses (adapted from ref. 38—reproduced by permission of The Royal Society of Chemistry http://dx.doi.org/10.1098/rsif.2008.0353.focus), (b) the skin of the cuttlefish Sepia apama (adapted from ref. 27—reproduced by permission of The Royal Society of Chemistry http://dx.doi.org/10.1098/rsif.2008.0366.focus), (c) the feathers of the yellow-breasted chat Icteria virens (adapted from ref. 38—reproduced by permission of The Royal Society of Chemistry http://dx.doi.org/10.1098/rsif.2008.0353.focus), and (d) the exoskeleton of the beetle Pachyrhynchus moniliferus (adapted from ref. 16—reproduced by permission of The Royal Society of Chemistry http://dx.doi.org/0.1039/B913217A).

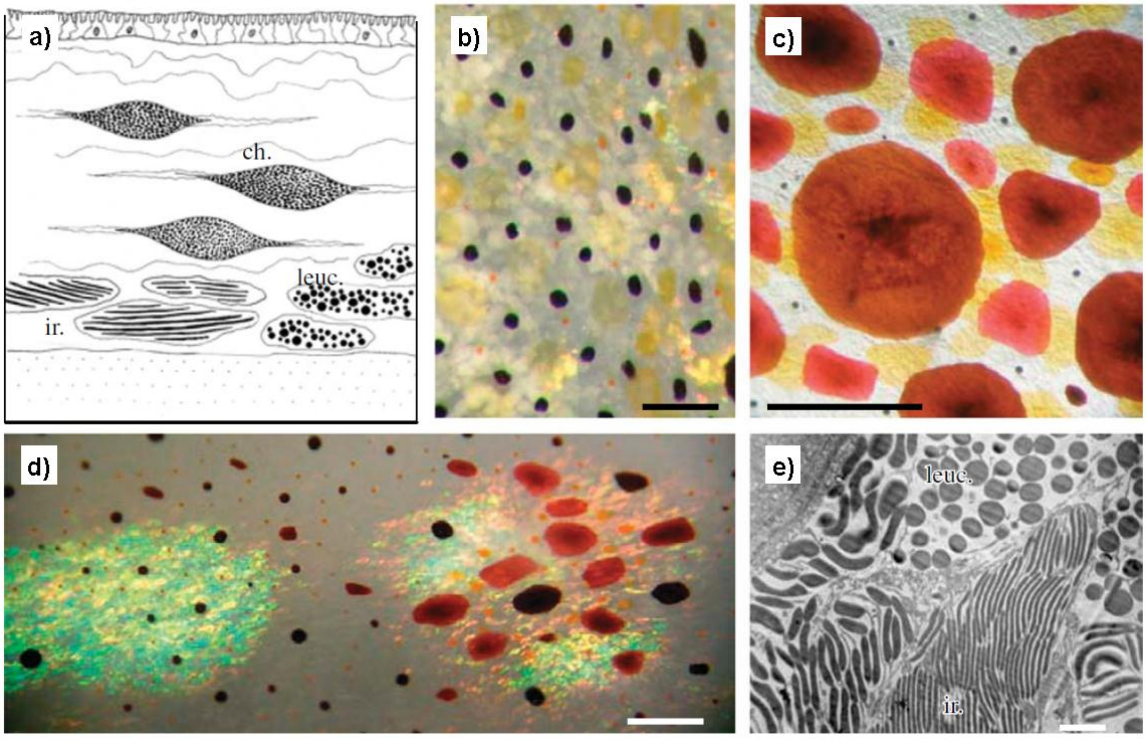

Figure 1.3 Structural coloration in cephalopod skin. (a) Skin in cross section showing the location of chromatophores (ch.) and structural reflectors (ir., iridophores; leuc., leucophores) in cephalopods. (b) Close-up of cuttlefish skin (*Sepia officinalis*) showing chromatophores (yellow, expanded; dark brown, partially retracted; orange, retracted) and white leucophores. Scale bar, 1 mm. (c) Brown, red and yellow chromatophores of squid (*L. pealeii*). Scale bar, 1 mm. (d) Combination of chromatophores and iridophores to illustrate the range of colours. Scale bar, 1 mm. (e) Electron micrograph showing iridophore plates (ir.) and spherical leucophores (leuc.) of cuttlefish (*S. officinalis*) skin. Scale bar, 1 mm. Reproduced with permission from reference 27.

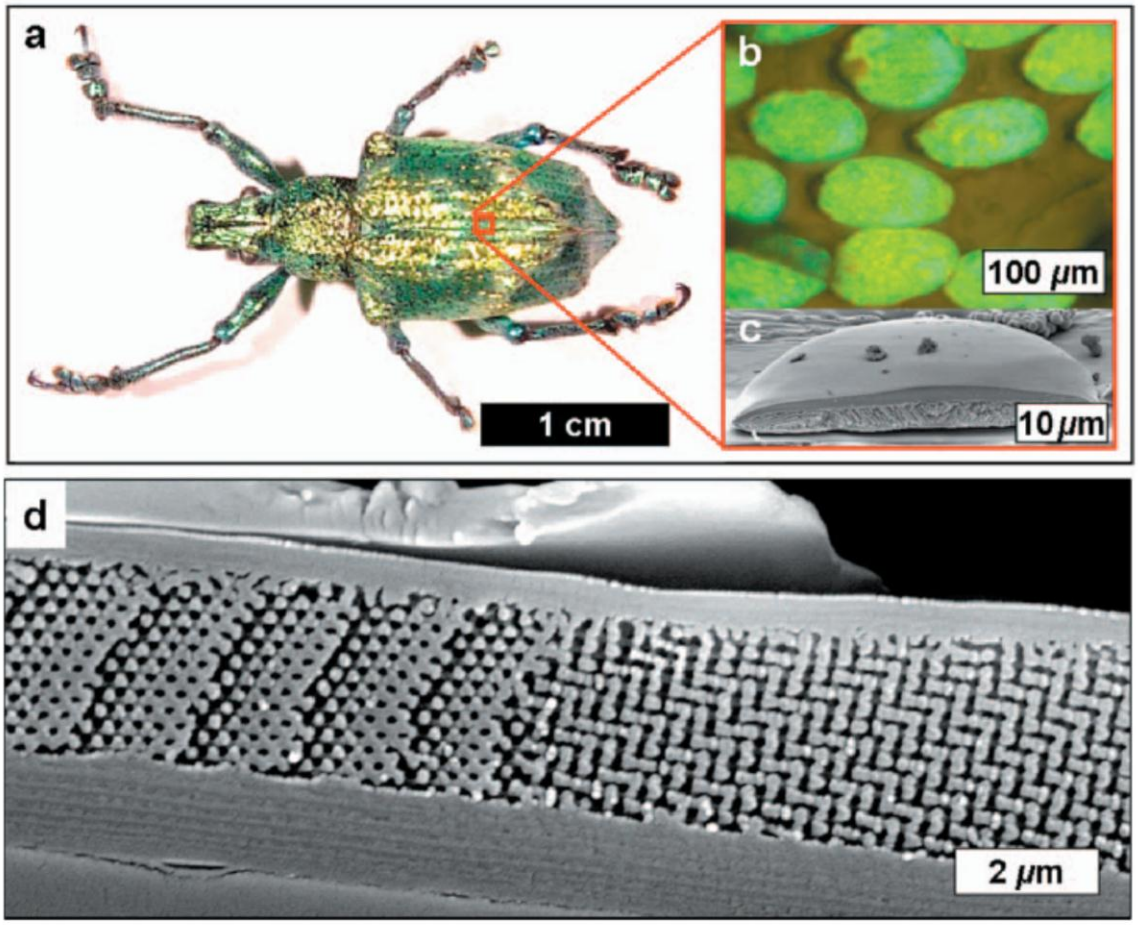

Figure 1.4 Images of structural color in the weevil *L. Augustus*. (a) Photograph of the entire insect. (b) Optical microscope image of individual scales found on the insects exoskeleton. (c) SEM image showing the cut edge of a single scale. (d) Detailed SEM of a cross-sectional region of a scale. Reprinted from ref 35 with permission from the American Physical Society.

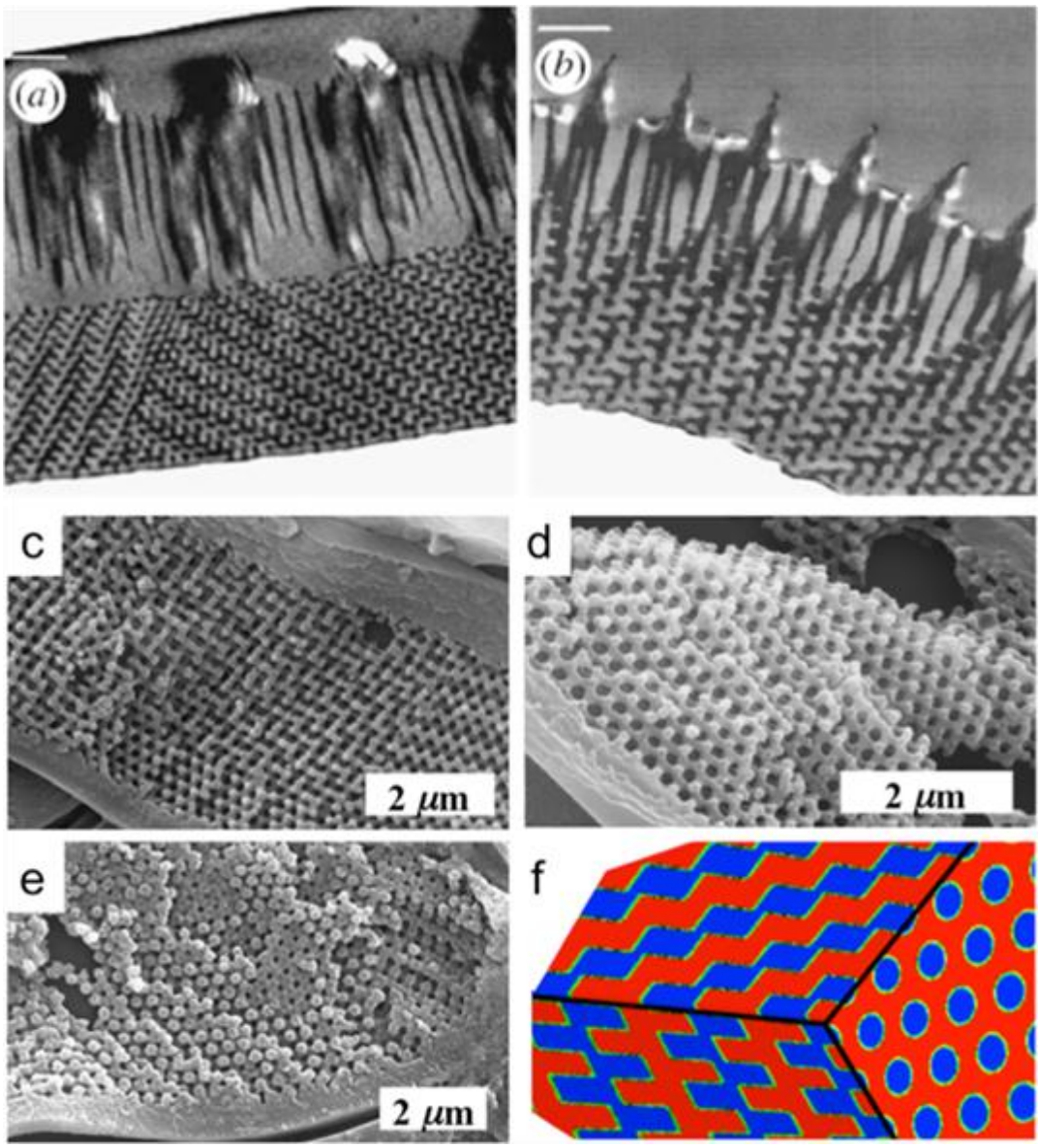

Figure 1.5 Examples of various structures found in insects. a, b) Transmission electron microscopy images of the photonic wing scale structure from the butterflies Parides sesostris (a) and Teinopalpus imperialis (b). Adapted from reference 51 – reproduced by permission of The Royal Society of Chemistry http://dx.doi.org/10.1098/rsif.2008.0353.focus. c, d, e) Scanning electron microscopy images of the photonic exoskeleton structure of the weevils Eupholus schoenherri, Pachyrhynchus moniliferus, and Eudiagogus pulcher, respectively. f) Calculated dielectric function of a diamond-based lattice (showing three orthogonal planes) isomorphous with that found in the weevil scales (air: dark; biopolymer: light). Adapted from reference 16 – reproduced by permission of The Royal Society of Chemistry http://dx.doi.org/10.1039/B913217A.

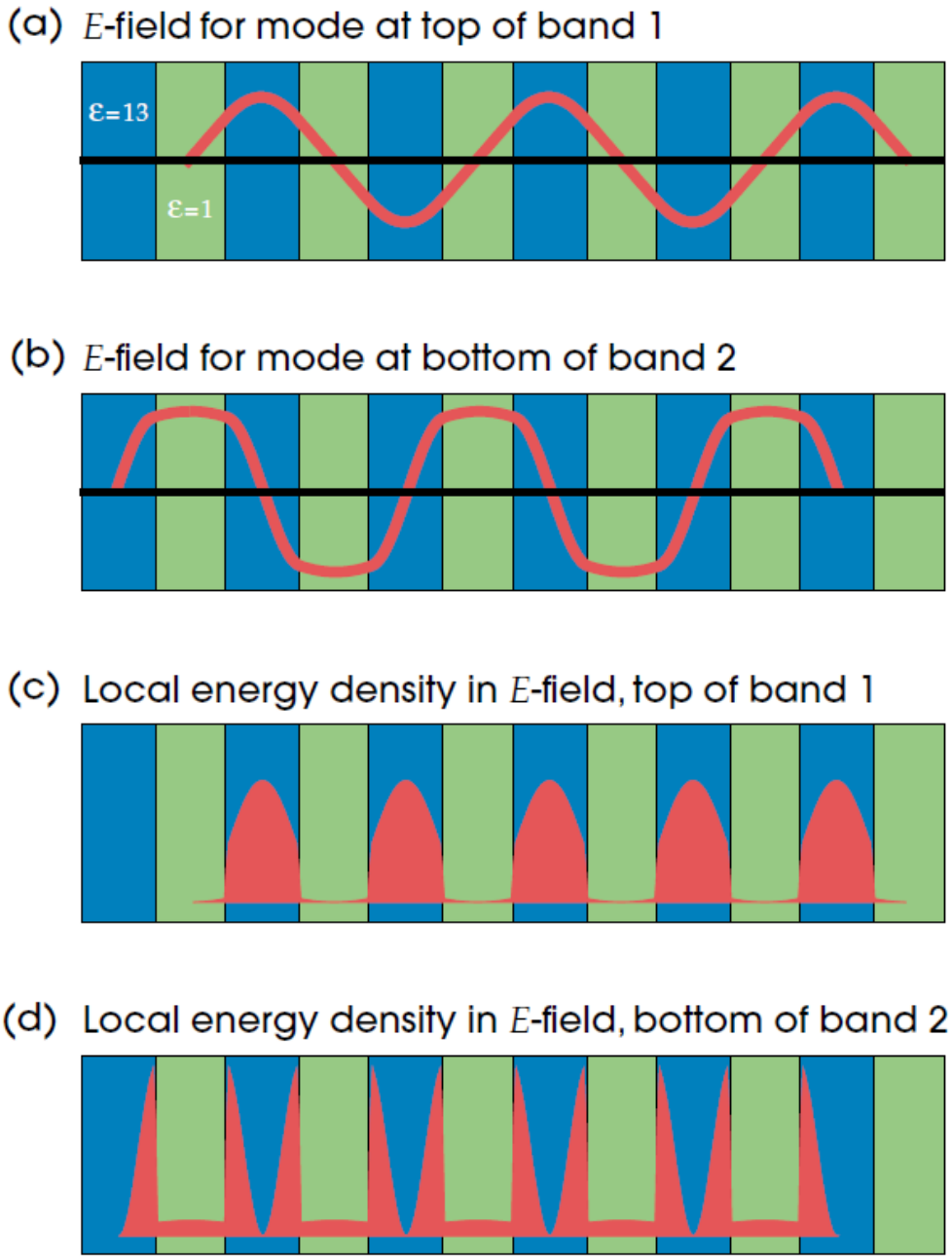

Figure 1.6 The modes associated with the photonic band gap in a one dimensional photonic crystal consisting of alternating layers of high and low dielectric, at $k = \pi/a$. The band gap arises due to the energy difference between the case where the electric field is concentrated in the high dielectric and the case where the electric field is concentrated in the low dielectric. Reprinted from ref 54 with permission from Princeton University Press.

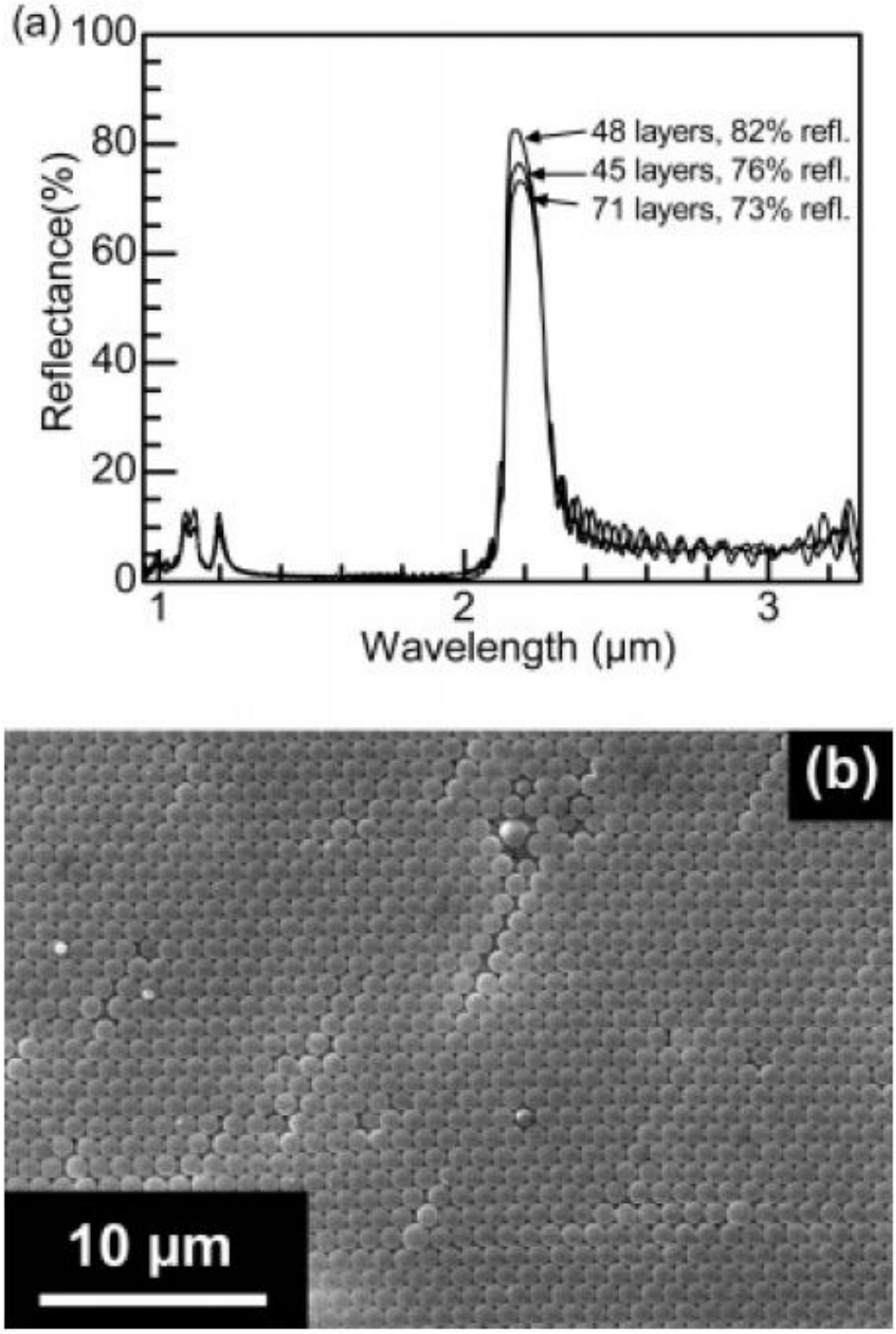

Figure 1.7 Synthetic opal photonic crystal and accompanying reflections. (a) IR reflection spectra from 3 colloidal photonic crystals prepared with varying numbers of layers from a 0.8% vol solution of spheres. (b) SEM of the top surface of the 71 layer crystal, having 73% reflection. Reprinted with permission from ref 71. Copyright (2006) American Chemical Society.

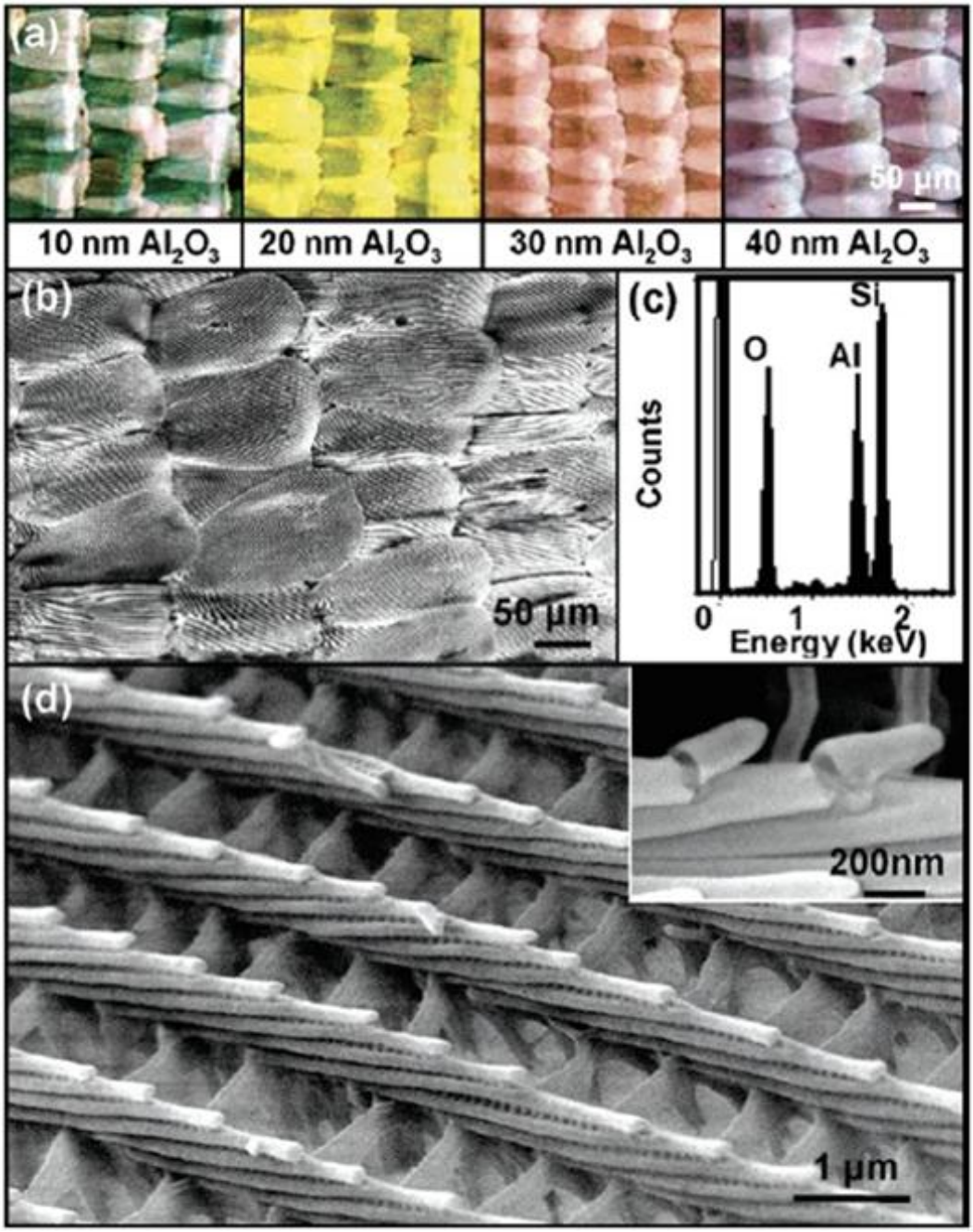

Figure 1.8 Example of carefully controlled bioreplication. a) Optical microscope image of the alumina coated *M. peleides* butterfly wing scales; color changes from original blue to pink. b) Scanning electron microscopy image of alumina replicas of butterfly wing scales. (c) Energy dispersive X-ray spectrum of alumina replicas shown in part b. d) Higher magnification scanning electron microscopy image of alumina replicas of butterfly wing scales and two broken rib tips (e). Reproduced with permission from reference 78. Copyright 2006 American Chemical Society.

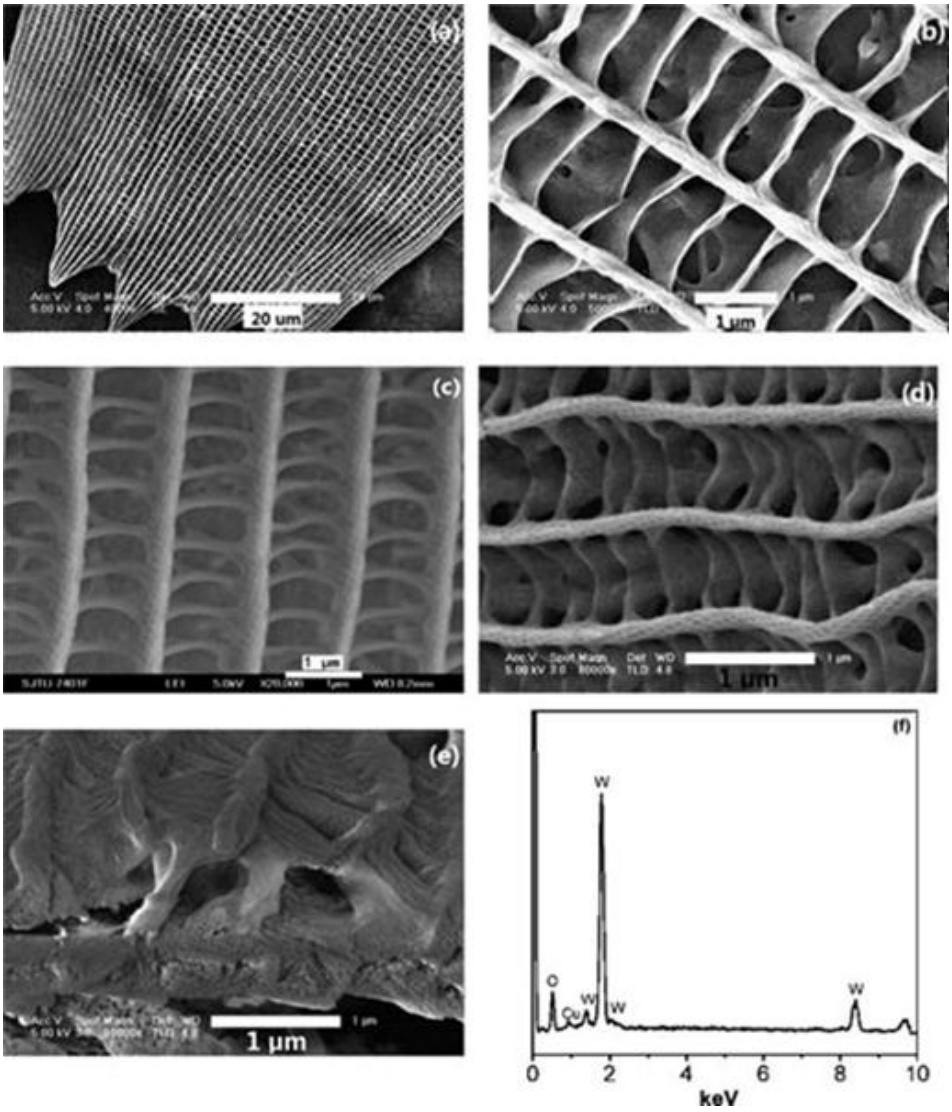

Figure 1.9 Top-view (a, b) and cross-view (c-e) scanning electron microscopy images of copper-doped tungsten oxide replicas of wing scales of the butterfly E. mulciber. f) Energy dispersive X-ray spectrum of the samples, revealing the presence of tungsten, oxygen and copper within the structure. Adapted from reference 87 – reproduced by permission of The Royal Society of Chemistry http://dx.doi.org/10.1039/C0JM02113J.

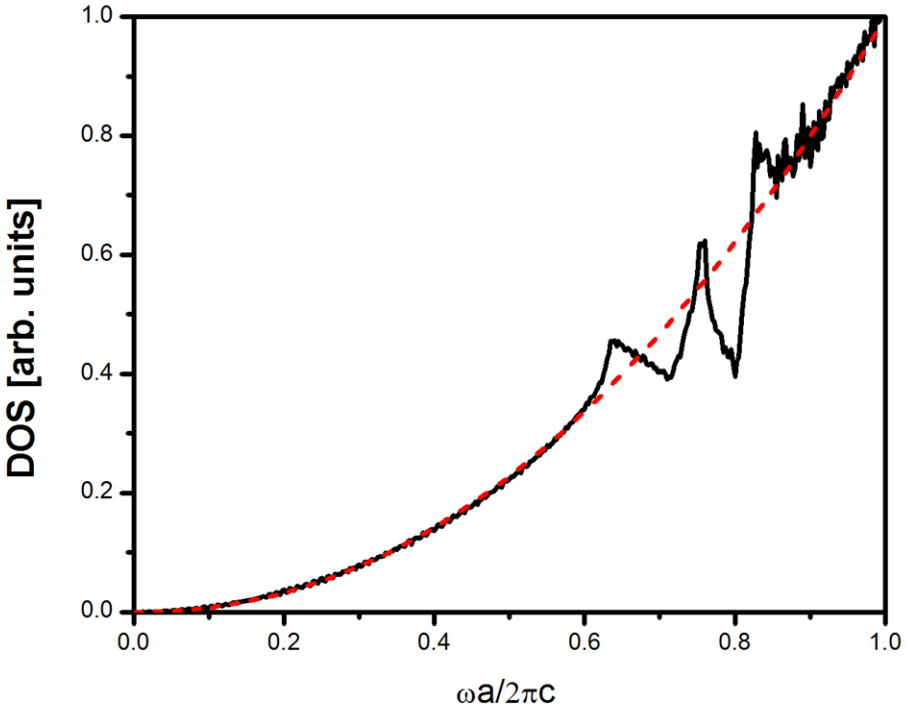

Figure 1.10 Example of calculated density of optical states for a FCC lattice of air cylinders surrounded by a material with dielectric of 2.4. The dashed line showing quadratic behavior represents the density of optical states in a homogenous medium having a dielectric equal to the effective dielectric of the structure as a whole.

References

1. Fujita, M.; Takahashi, S.; Tanaka, Y.; Asano, T.; Noda, S., Simultaneous Inhibition and Redistribution of Spontaneous Light Emission in Photonic Crystals. *Science* **2005,** *308* (5726), 1296-1298.

2. Mihi, A.; Miguez, H., Origin of Light-Harvesting Enhancement in Colloidal-Photonic-Crystal-Based Dye-Sensitized Solar Cells. *J. Phys. Chem. B* **2005,** *109* (33), 15968-15976.

3. Noda, S.; Fujita, M.; Asano, T., Spontaneous-Emission Control by Photonic Crystals and Nanocavities. *Nat. Photonics* **2007,** *1* (8), 449-458.

4. Joannopoulos, J. D.; Villeneuve, P. R.; Fan, S., Photonic Crystals: Putting a New Twist on Light. *Nature* **1997,** *386* (6621), 143-149.

5. Soukoulis, C. M., *Photonic Crystals and Light Localization*. Kluwer: Dordrecht, 2001.

6. Brennen, G. K.; Caves, C. M.; Jessen, P. S.; Deutsch, I. H., Quantum Logic Gates in Optical Lattices. *Phys. Rev. Lett.* **1999,** *82* (5), 1060.

7. Güney, D. Ö.; Meyer, D. A., Creation of Entanglement and Implementation of Quantum Logic Gate Operations Using a Three-Dimensional Photonic Crystal Single-Mode Cavity. *J. Opt. Soc. Am. B* **2007,** *24* (2), 283-294.

8. Painter, O.; Lee, R. K.; Scherer, A.; Yariv, A.; O'Brien, J. D.; Dapkus, P. D.; Kim, I., Two-Dimensional Photonic Band-Gap Defect Mode Laser. *Science* **1999,** *284* (5421), 1819-1821.

9. Woldeyohannes, M.; John, S., Coherent Control of Spontaneous Emission Near a Photonic Band Edge. *J. Opt. B* **2003,** (2), R43-R82.

10. Park, H.-G.; Kim, S.-H.; Kwon, S.-H.; Ju, Y.-G.; Yang, J.-K.; Baek, J.-H.; Kim, S.-B.; Lee, Y.-H., Electrically Driven Single-Cell Photonic Crystal Laser. *Science* **2004,** *305* (5689), 1444-1447.

11. John, S., Strong Localization of Photons in Certain Disordered Dielectric Superlattices. *Phys. Rev. Lett.* **1987,** *58* (23), 2486.

12. Yablonovitch, E., Inhibited Spontaneous Emission in Solid-State Physics and Electronics. *Phys. Rev. Lett.* **1987,** *58* (20), 2059.

13. Yablonovitch, E.; Gmitter, T. J.; Leung, K. M., Photonic Band Structure: The Face-Centered-Cubic Case Employing Nonspherical Atoms. *Phys. Rev. Lett.* **1991,** *67* (17), 2295.

14. Blanco, A.; Chomski, E.; Grabtchak, S.; Ibisate, M.; John, S.; Leonard, S. W.; Lopez, C.; Meseguer, F.; Miguez, H.; Mondia, J. P.; Ozin, G. A.; Toader, O.; van Driel, H. M., Large-Scale Synthesis of a Silicon Photonic Crystal with a Complete Three-Dimensional Bandgap near 1.5 Micrometres. *Nature* **2000,** *405* (6785), 437-440.

15. Galusha, J. W.; Jorgensen, M. R.; Bartl, M. H., Diamond-Structured Titania Photonic-Bandgap Crystals from Biological Templates. *Adv. Mater.* **2010,** *22* (1), 107-110.

16. Galusha, J. W.; Richey, L. R.; Jorgensen, M. R.; Gardner, J. S.; Bartl, M. H., Study of Natural Photonic Crystals in Beetle Scales and their Conversion into Inorganic Structures via a Sol-Gel Bio-templating Route. *J. Mater. Chem.* **2010,** *20* (7), 1277-1284.

17. Jorgensen, M. R.; Bartl, M. H., Biotemplating Routes to Three-Dimensional Photonic Crystals. *J. Mater. Chem.* **2011,** *21* (29), 10583-10591.

18. Jorgensen, M. R.; Galusha, J. W.; Bartl, M. H., Strongly Modified Spontaneous Emission Rates in Diamond-Structured Photonic Crystals. *Phys. Rev. Lett.* **2011,** *107* (14), 143902.

19. Jorgensen, M. R.; Yonkee, B.; Bartl, M. H. In *Strong Modification of Density of Optical States in Biotemplated Photonic Crystals*, SPIE 8071, Prague, Czech Republic, Bertolotti, M., Ed. SPIE: Prague, Czech Republic, 2011; pp 807109-9.

20. Chen, J. I. L.; von Freymann, G.; Choi, S. Y.; Kitaev, V.; Ozin, G. A., Amplified Photochemistry with Slow Photons. *Adv. Mater.* **2006,** *18* (14), 1915-1919.

21. Arpin, K. A.; Mihi, A.; Johnson, H. T.; Baca, A. J.; Rogers, J. A.; Lewis, J. A.; Braun, P. V., Multidimensional Architectures for Functional Optical Devices. *Adv. Mater.* **2010,** *22* (10), 1084–1101.

22. Halaoui, L. I.; Abrams, N. M.; Mallouk, T. E., Increasing the Conversion Efficiency of Dye-Sensitized TiO2 Photoelectrochemical Cells by Coupling to Photonic Crystals. *J. Phys. Chem. B* **2005,** *109* (13), 6334-6342.

23. Weiner, S.; Addadi, L.; Wagner, H. D., Materials Design in Biology. *Mat. Sci. Eng. C* **2000,** *11* (1), 1-8.

24. Aizenberg, J.; Weaver, J. C.; Thanawala, M. S.; Sundar, V. C.; Morse, D. E.; Fratzl, P., Skeleton of Euplectella sp.: Structural Hierarchy from the Nanoscale to the Macroscale. *Science* **2005,** *309* (5732), 275-278.

25. Cha, J. N.; Shimizu, K.; Zhou, Y.; Christiansen, S. C.; Chmelka, B. F.; Stucky, G. D.; Morse, D. E., Silicatein Filaments and Subunits from a Marine Sponge Direct the Polymerization of Silica and Silicones In Vitro. *Proc. Natl. Acad. Sci. USA* **1999,** *96* (2), 361-365.

26. Srinivasarao, M., Nano-Optics in the Biological World: Beetles, Butterflies, Birds, and Moths. *Chem. Rev.* **1999,** *99* (7), 1935-1962.

27. Mäthger, L. M.; Denton, E. J.; Marshall, N. J.; Hanlon, R. T., Mechanisms and Behavioural Functions of Structural Coloration in Cephalopods. *J. R. Soc. Interface* **2009,** *6* (Suppl 2), S149-S163.

28. Dolphin, A. C., β Subunits of Voltage-Gated Calcium Channels. *J. Bioenerg. Biomembr.* **2003,** *35* (6), 599-620.

29. Arikkath, J.; Campbell, K. P., Auxiliary Subunits: Essential Components of the Voltage-Gated Calcium Channel Complex. *Curr. Opin. Neurobiol.* **2003,** *13* (3), 298-307.

30. Glover, B. J.; Whitney, H. M., Structural Colour and Iridescence in Plants: The Poorly Studied Relations of Pigment Colour. *Ann. Bot. London* **2010,** *105* (4), 505-511.

31. Lee, D. W., Ultrastructural Basis and Function of Iridescent Blue Colour of Fruits in Elaeocarpus. *Nature* **1991,** *349* (6306), 260-262.

32. Bone, R. A.; Lee, D. W.; Norman, J. M., Epidermal Cells Functioning as Lenses in Leaves of Tropical Rain-Forest Shade Plants. *Appl. Opt.* **1985,** *24* (10), 1408-1412.

33. Prum, R. O.; Torres, R. H., Structural Colouration of Mammalian Skin: Convergent Evolution of Coherently Scattering Dermal Collagen Arrays. *J. Exp. Biol.* **2004,** *207* (12), 2157-2172.

34. Vukusic, P.; Sambles, J. R., Photonic Structures in Biology. *Nature* **2003,** *424* (6950), 852-855.

35. Galusha, J. W.; Richey, L. R.; Gardner, J. S.; Cha, J. N.; Bartl, M. H., Discovery of a Diamond-Based Photonic Crystal Structure in Beetle Scales. *Phys. Rev. E* **2008,** *77* (5), 050904(1-4).

36. Ghiradella, H. T.; Butler, M. W., Many Variations on a Few Themes: A Broader Look at Development of Iridescent Scales (and Feathers). *J. R. Soc. Interface* **2009,** *6* (Suppl 2), S243-S251.

37. Prum, R. O.; Dufresne, E. R.; Quinn, T.; Waters, K., Development of Colour-Producing β-keratin Nanostructures in Avian Feather Barbs. *J. R. Soc. Interface* **2009,** *6* (Suppl 2), S253-S265.

38. Shawkey, M. D.; Morehouse, N. I.; Vukusic, P., A Protean Palette: Colour Materials and Mixing in Birds and Butterflies. *J. R. Soc. Interface* **2009,** *6* (Suppl 2), S221-S231.

39. Doucet, S. M.; Meadows, M. G., Iridescence: A Functional Perspective. *J. R. Soc. Interface* **2009,** *6* (Suppl 2), S115-S132.

40. Parker, A. R., The Diversity and Implications of Animal Structural Colours. *J. Exp. Biol.* **1998,** *201* (16), 2343-2347.

41. Vigneron, J. P.; Colomer, J. F.; Vigneron, N.; Lousse, V., Natural Layer-By-Layer Photonic Structure in the Squamae of Hoplia Coerulea (Coleoptera). *Phys. Rev. E* **2005,** *72* (061), 904.

42. Ha, Y. H.; Vaia, R. A.; Lynn, W. F.; Costantino, J. P.; Shin, J.; Smith, A. B.; Matsudaira, P. T.; Thomas, E. L., Three-Dimensional Network Photonic Crystals via Cyclic Size Reduction/ Infiltration of Sea Urchin Exoskeleton. *Adv. Mater.* **2004,** *16* (13), 1091-1093.

43. Parker, A. R.; McPhedran, R. C.; McKenzie, D. R.; Botten, L. C.; Nicorovici, N. A. P., Photonic Engineering - Aphrodite's Iridescence. *Nature* **2001,** *409* (6816), 36-37.

44. Li, Y.; Lu, Z.; Yin, H.; Yu, X.; Liu, X.; Zi, J., Structural Origin of the Brown Color of Barbules in Male Peacock Tail Feathers. *Phys. Rev. E* **2000,** *72*, 010902.

45. Vigneron, J. P.; Colomer, J. F.; Rassart, M.; Ingram, A. L.; Lousse, V., Structural Origin of the Colored Reflections from the Black-Billed Magpie Feathers. *Phys. Rev. E.* **1993,** *73*, 021914.

46. Biró, L. P.; Kertész, K.; Vértesy, Z.; Márk, G. I.; Bálint, Z.; Lousse, V.; Vigneron, J. P., Living Photonic Crystals: Butterfly Scales -- Nanostructure and Optical Properties. *Mat. Sci. Eng. C* **2007,** *27* (5-8), 941-946.

47. Seago, A. E.; Brady, P.; Vigneron, J.-P.; Schultz, T. D., Gold Bugs and Beyond: A Review of Iridescence and Structural Colour Mechanisms in Beetles (Coleoptera). *J. R. Soc. Interface* **2009,** *6* (Suppl 2), S165-S184.

48. Prum, R. O.; Quinn, T.; Torres, R. H., Anatomically Diverse Butterfly Scales All Produce Structural Colours by Coherent Scattering. *J. Exp. Biol.* **2006,** *209* (4), 748-765.

49. Galusha, J. W.; Richey, L. R.; Bartl, M. H., High Resolution Three-Dimensional Reconstruction of Photonic Crystal Structure Found in Beetle Scales. *IEEE LEOS Summer Conference* **2008**.

50. Michielsen, K.; Stavenga, D. G., Gyroid Cuticular Structures in Butterfly Wing Scales: Biological Photonic Crystals. *J. R. Soc. Interface* **2008,** *5* (18), 85-94.

51. Poladian, L.; Wickham, S.; Lee, K.; Large, M. C. J., Iridescence from Photonic Crystals and its Suppression in Butterfly Scales. *J. R. Soc. Interface* **2009,** *6* (Suppl 2), S233-S242.

52. McQuarrie, D. A.; Simon, J. D., *Physical Chemistry: A Molecular Approach*. University Science Books: Sausalito, 1997.

53. Johnson, S.; Joannopoulos, J., Block-Iterative Frequency-Domain Methods for Maxwell's Equations in a Planewave Basis. *Opt. Express* **2001,** *8* (3), 173-190.

54. Joannopoulos, J. D., *Photonic Crystals: Molding the Flow of Light*. Princeton Univ Pr: 2008.

55. Lin, S.; Fleming, J.; Hetherington, D.; Smith, B.; Biswas, R.; Ho, K.; Sigalas, M.; Zubrzycki, W.; Kurtz, S.; Bur, J., A Three-Dimensional Photonic Crystal Operating at Infrared Wavelengths. *Nature* **1998,** *394* (6690), 251-253.

56. Noda, S.; Tomoda, K.; Yamamoto, N.; Chutinan, A., Full Three-Dimensional Photonic Bandgap Crystals at Near-Infrared Wavelengths. *Science* **2000,** *289* (5479), 604-606.

57. Y. A. Vlasov, X. Z. B., J. C. Sturm, D. J. Norris, On-Chip Natural Assembly of Silicon Photonic Bandgap Crystals. *Nature* **2001,** *414*, 289-293.

58. Maldovan, M.; Thomas, E. L.; Carter, C. W., Layer-By-Layer Diamond-Like Woodpile Structure with a Large Photonic Band Gap. *Appl. Phys. Lett.* **2004,** *84* (3), 362-364.

59. Qi, M. H.; Lidorikis, E.; Rakich, P. T.; Johnson, S. G.; Joannopoulos, J. D.; Ippen, E. P.; Smith, H. I., A Three-Dimensional Optical Photonic Crystal with Designed Point Defects. *Nature* **2004,** *429* (6991), 538-542.

60. Wong, S.; Deubel, M.; Perez-Willard, F.; John, S.; Ozin, G. A.; Wegener, M.; von Freymann, G., Direct Laser Writing of Three-Dimensional Photonic Crystals with Complete a Photonic Bandgap in Chalcogenide Glasses. *Adv. Mater.* **2006,** *18* (3), 265-+.

61. García-Santamaría, F.; Xu, M.; Lousse, V.; Fan, S.; Braun, P. V.; Lewis, J. A., A Germanium Inverse Woodpile Structure with a Large Photonic Band Gap. *Adv. Mater.* **2007,** *19*, 1567–1570.

62. Hermatschweiler, M.; Ledermann, A.; Ozin, G. A.; Wegener, M.; von Freymann, G., Fabrication of Silicon Inverse Woodpile Photonic Crystals. *Adv. Funct. Mater.* **2007,** *17* (14), 2273-2277.

63. Sun, H., Three-Dimensional Photonic Crystal Structures Achieved with Two-Photon-Absorption Photopolymerization of Resin. *Appl. Phys. Lett.* **1999,** *74* (6), 786.

64. Deubel, M.; von Freymann, G.; Wegener, M.; Pereira, S.; Busch, K.; Soukoulis, C. M., Direct Laser Writing of Three-Dimensional Photonic-Crystal Templates for Telecommunications. *Nat. Mater.* **2004,** *3* (7), 444-447.

65. Gratson, G. M.; Xu, M.; Lewis, J. A., Microperiodic Structures: Direct Writing of Three-Dimensional Webs. *Nature* **2004,** *428* (6981), 386-386.

66. Lewis, J. A., Direct Ink Writing of 3D Functional Materials. *Adv. Funct. Mater.* **2006,** *16* (17), 2193-2204.

67. Gratson, G. M.; García-Santamaría, F.; Lousse, V.; Xu, M.; Fan, S.; Lewis, J. A.; Braun, P. V., Direct-Write Assembly of Three-Dimensional Photonic Crystals: Conversion of Polymer Scaffolds to Silicon Hollow-Woodpile Structures. *Adv. Mater.* **2006,** *18* (4), 461-465.

68. Tétreault, N.; von Freymann, G.; Deubel, M.; Hermatschweiler, M.; Pérez-Willard, F.; John, S.; Wegener, M.; Ozin, G. A., New Route to Three-Dimensional Photonic Bandgap Materials: Silicon Double Inversion of Polymer Templates. *Adv. Mater.* **2006,** *18* (4), 457-460.

69. Jiang, P.; Bertone, J. F.; Hwang, K. S.; Colvin, V. L., Single-Crystal Colloidal Multilayers of Controlled Thickness. *Chem. Mater.* **1999,** *11* (8), 2132-2140.

70. Norris, D. J.; Arlinghaus, E. G.; Meng, L.; Heiny, R.; Scriven, L. E., Opaline Photonic Crystals: How Does Self-Assembly Work? *Adv. Mater.* **2004,** *16*, 1393-1399.

71. Shimmin, R. G.; DiMauro, A. J.; Braun, P. V., Slow Vertical Deposition of Colloidal Crystals: A Langmuir-Blodgett Process? *Langmuir* **2006,** *22*, 6507-6513.

72. Tétreault, N.; Míguez, H.; Ozin, G. A., Silicon Inverse Opal—A Platform for Photonic Bandgap Research. *Adv. Mater.* **2004,** *16* (16), 1471-1476.

73. Busch, K.; John, S., Photonic Band Gap Formation in Certain Self-Organizing Systems. *Phys. Rev. E* **1998,** *58* (3), 3896.

74. Aguirre, C. I.; Reguera, E.; Stein, A., Tunable Colors in Opals and Inverse Opal Photonic Crystals. *Adv. Funct. Mater.* **2010,** *20* (16), 2565-2578.

75. Aparicio, F. J.; Lozano, G.; Blaszczyk-Lezak, I.; Barranco, A. n.; Míguez, H. n., Conformal Growth of Organic Luminescent Planar Defects within Artificial Opals. *Chem. Mater.* **2009,** *22* (2), 379-385.

76. Ding, T.; Song, K.; Clays, K.; Tung, C.-H., Bottom-Up Photonic Crystal Approach with Top-Down Defect and Heterostructure Fine-Tuning. *Langmuir* **2009,** *26* (6), 4535-4539.

77. Parker, A. R.; Townley, H. E., Biomimetics of Photonic Nanostructures. *Nat. Nano.* **2007,** *2* (6), 347-353.

78. Huang; WangWang; Wang, Z. L., Controlled Replication of Butterfly Wings for Achieving Tunable Photonic Properties. *Nano Lett.* **2006,** *6* (10), 2325-2331.

79. Gaillot, D. P.; Deparis, O.; Welch, V.; Wagner, B. K.; Vigneron, J. P.; Summers, C. J., Composite Organic-Inorganic Butterfly Scales: Production of Photonic Structures with Atomic Layer Deposition. *Phys. Rev. E* **2008,** *78* (3), 031922.

80. Huang, J.; Wang, X.; Wang, Z. L., Bio-Inspired Fabrication of Antireflection Nanostructures by Replicating Fly Eyes. *Nanotechnology* **2008,** *19* (2), 025602.

81. Martín-Palma, R. J., Biomimetization of Butterfly Wings by the Conformal-Evaporated-Film-By-Rotation Technique for Photonics. *Appl. Phys. Lett.* **2008,** *93* (8), 083901.

82. Martín-Palma, R. J.; et al., Replication of Fly Eyes by the Conformal-Evaporated-Film-By-Rotation Technique. *Nanotechnology* **2008,** *19* (35), 355704.

83. Lakhtakia, A.; Martín-Palma, R. J.; Motyka, M. A.; Pantano, C. G., Fabrication of Free-Standing Replicas of Fragile, Laminar, Chitinous Biotemplates. *Bioinsp. Biomim.* **2009,** *4*, 034001.

84. Zhang, W.; Zhang, D.; Fan, T.; Gu, J.; Ding, J.; Wang, H.; Guo, Q.; Ogawa, H., Novel Photoanode Structure Templated from Butterfly Wing Scales. *Chem. Mater.* **2008,** *21* (1), 33-40.

85. Zhang, W.; Zhang, D.; Fan, T.; Ding, J.; Gu, J.; Guo, Q.; Ogawa, H., Biosynthesis of Cathodoluminescent Zinc Oxide Replicas Using Butterfly (Papilio paris) Wing Scales as Templates. *Mat. Sci. Eng. C* **2009,** *29* (1), 92-96.

86. Zhu, S.; Zhang, D.; Chen, Z.; Gu, J.; Li, W.; Jiang, H.; Zhou, G., A Simple and Effective Approach Towards Biomimetic Replication of Photonic Structures from Butterfly Wings. *Nanotechnology* **2009,** *20* (31), 315303.

87. Zhu, S.; Liu, X.; Chen, Z.; Liu, C.; Feng, C.; Gu, J.; Liu, Q.; Zhang, D., Synthesis of Cu-Doped WO_3 Materials with Photonic Structures for High Performance Sensors. *J. Mater. Chem.* **2010,** *20*, 9126-9132.

88. Jorgensen, M. R.; Yonkee, B. P.; Bartl, M. H., Solid and Hollow Inorganic Replicas of Biological Photonic Crystals. *Scripta Mater.* **2011,** *65* (11), 954-957.

89. Brinker, D. J.; Scherrer, G. W., *Sol−Gel Science, The Physics and Chemistry of Sol−Gel Processing*. Academic Press: San Diego, CA, 1990.

90. Zhao, D.; Yang, P.; Melosh, N.; Feng, J.; Chmelka, B. F.; Stucky, G. D., Continuous Mesoporous Silica Films with Highly Ordered Large Pore Structures. *Adv. Mater.* **1998,** *10* (16), 1380-+.

91. Nikolaev, I. S.; Vos, W. L.; Koenderink, A. F., Accurate Calculation of the Local Density of Optical States in Inverse-Opal Photonic Crystals. *J. Opt. Soc. Am. B* **2009,** *26* (5), 987-997.

92. Loudon, R., *The Quantum Theory of Light*. Oxford University Press: New York, 2000.

CHAPTER 2

BIOTEMPLATING ROUTES TO THREE-DIMENSIONAL PHOTONIC CRYSTALS

Introduction

Nature produces many interesting examples of biological photonic crystals operating in the visible region. These intricate structures are responsible for many optical effects and colors of marine animals, birds and insects, and offer a palette of lattice structures to choose from,[1-13] including the most sought-after diamond-based lattices that were recently discovered by the Bartl group in exoskeleton scales of certain weevils.[14-15] Unfortunately, these biopolymeric photonic crystal structures have limited value for direct experimental use because they autofluoresce, are mechanically unstable and have a relatively low refractive index. However, they are valuable templates and can be used to create replicas out of inorganic compounds.[10, 12]

With the discovery of diamond-based photonic crystal lattices in certain weevils,[14-15] a door to exciting new possibilities in photonic band gap research was opened. For example, digital modeling and band structure calculations showed the diamond-based lattice found in the weevil *Lamprocyphus augustus* possesses a complete photonic band gap in the green region of the electromagnetic spectrum when fabricated out of a dielectric compound with a refractive index of 2.1 or higher.[16] These

calculations also revealed that a complete band gap only opens for a positive replica of the beetle's lattice, eliminating conventional single-infiltration sol-gel processes that only result in the formation of inverse copies of the original template.

These calculations by a graduate student in the Bartl group (Jeremy Galusha) were very promising. In response to these calculations, I assisted him in the development of a double-imprint sol-gel biotemplation method to convert the bio-structures into high-dielectric replicas (Figure 2.1).[16] After Jeremy left, I took over the project and searched for ways to expand the range of possible inorganic replicas that can be fabricated from one type of biotemplate. These studies were supported by the fact that even certain partial band gaps in photonic crystals are still capable of controlling light in important ways. In the following, it will be shown how sol-gel bioreplication can be tuned to yield several different inorganic replicas from one particular biological photonic crystal structure. For example, by modifying the sol-gel precursor composition and/or the processing parameters used, four different types of replica photonic crystals can be created from one type of biotemplate with a diamond-based lattice. These replicas include negative solid replicas (solid inverse structures) made out of silica and titania, and negative hollow replicas (hollow inverse structures) made out of silica and titania; an additional fifth structure, a positive solid replica made out of titania can be made by using the solid inverse silica structure as a sacrificial template.[17] All these structures were experimentally investigated by optical spectroscopy and scanning electron microscopy (SEM). Figure 2.2 outlines the general biotemplating method used for inverse-type structures.

Bioreplication Processes

The insects used in this study as biotemplates were the weevils *Lamprocyphus augustus*, *Eupholus schoenherri* and *Pachyrhynchus moniliferus*, and were obtained from "Bugmaniac," Diepenbeek, Belgium (www.thebugmaniac.be). While each of these weevils has scales containing isomorphic diamond-based photonic lattice structures of air cylinders surrounded by the biopolymer chitin, their crystal lattice constants differ, resulting in photonic stop gaps and thus optical reflection peaks at various wavelength positions between 500 and 700 nm.[15]

For replication, weevil scales were scraped off the exoskeleton of the insect and sandwiched between two clean glass slides. In all procedures, except the silica solid inverse replicas used in the double-imprint, the scales were pretreated with 3:1 $HNO_3/HClO_4$ to remove the thin waxy layer coating the biopolymer structure, followed by soaking in water and then ethanol for at least 1 h at each stage as shown in Figure 2.2. The pretreated samples were thoroughly dried at 50 °C prior to sol–gel infiltration. Following pretreatment the processing parameters were varied to produce different structures (see Figures 2.2 and 2.3).[16-18]

Below, a detailed description of the sol-gel solution parameters and processing conditions are presented for the fabrication of five different inorganic replicas from one biological template.

Silica Negative Solid Replica

A single scale was removed from *L. augustus* and infiltrated by capillary forces with an SBA-type[19] hybrid organic/inorganic precursor solution. SBA-type hybrid silica

was used as the sol compound due to its superior structural properties (i.e., minimized crack-formation and framework collapse) upon drying compared to pure silica.[20] The silica sol was prepared by hydrolyzing tetraethylorthosilicate (5.6 mL, Aldrich) in 0.1 M HCl (1.9 mL) followed by the addition of the block-copolymer Pluronic® F127 (1.0 g) dissolved in ethanol (10 mL). After a short drying-period the biopolymeric template was removed by $HNO_3/HClO_4$ acid-etching. The silica based imprint was rinsed with DI water and placed onto a glass slide.

Silica Negative Hollow Replica

Hollow silica shell structures (hollow positive silica replicas) were made in a similar manner to silica inverse structures. Sol-gel solution was made using the procedure above, except that Pluronic F127 was omitted. The pretreated scales were infiltrated with sol-gel solution and allowed to dry for 3 h before being placed in a 100 °C oven for 1 h, after which the slides were separated. The chitin template was removed by thermal degradation in air by heating the sample slowly at 2 °C/min to 400 °C where it was held for 3 h.

Titania Negative Solid Replica

Solid titania inverse structures (negative titania replicas) were prepared by infiltrating pretreated scales with titania solution (2 mL TEOT, 1.4 mL conc. HCl, and 2 mL ethanol). After a 24 h drying period, the slides were separated and the chitin template was removed by slowly heating the samples at 2 °C/min in a muffle furnace to 450 °C, and holding the samples at that temperature for 3 h.

Titania Negative Hollow Replica

Hollow titania shell structures (hollow positive titania replicas) were prepared by slightly modifying the titania sol-gel solution (2 mL TEOT, 0.4 mL conc. HCl, 1.6 mL TFA). The same infiltration, drying, and template remove procedure was used as in the fabrication procedure of negative titania replicas.

Titania Positive Solid Replica.

To produce positive replica, a double-imprint biotemplating route was used.[16] In the first step of this route an inverse of the original biopolymeric beetle photonic structure was created via the silica-based sol-gel chemistry route explained above. This inverse was subsequently used as an intermediary template for creating a titania replica of the original diamond-based structure. Here, the silica framework was infiltrated with an acid-stabilized liquid titania sol-gel precursor by capillary forces. The titania sol was prepared by hydrolyzing titanium ethoxide (2 mL, Aldrich) in a mixture of concentrated trifluoroacetic acid (1.6 mL) and concentrated HCl (0.4 mL) for 20 min after which ethanol (2 mL) was added. Infiltration was followed by heating of the silica/titania composite at 500 °C for 2 h to induce titania nano-crystallization. To ensure a highly crystalline, dense titania framework, the infiltration-crystallization cycle was repeated. In this way, possible cavities and cracks formed due to shrinkage in the initial heat-treatment were filled with titania. Repeated infiltration-crystallization was also useful to tune the volume fraction of infiltrated titania and we found that between one and three successive cycles gave the best results. Finally, the intermediary silica-based template

was removed by HF acid-etching, producing a structurally fine-tuned titania replica of the beetle's diamond-based photonic crystal with lattice periodicities at visible wavelengths.

Characterization Studies

Optical microreflectance data were collected from each of the structures using a Nikon ME600 light microscope equipped with a 20× objective (N.A. 0.45), which was fiber-coupled to an Ocean Optics USB4000 vis/NIR spectrometer. The lattice structures of each of the replicas were determined by SEM imaging using an FEI NovaNano microscope. For SEM imaging, inorganic biotemplated structures were moved to a clean substrate using a statically charged razor blade. The scales were removed from the blade by touching it to a small droplet of ethanol on the substrate. After transfer, the structures were crushed to reveal the interior structure. The pieces were collected on a piece of conductive tape, mounted to an SEM stub, and coated with a thin layer of gold for imaging.

Results and Discussion

Using biological scales as templates was a unique materials challenge for two reasons: the natural variation in surface chemistry and the physical size of the scales. It was found that while the key structural features were isomorphic across several species of weevils, the interaction of titania and silica sol-gels with the biopolymeric frameworks varied. We speculate that this is due to a variation in surface chemistry within the scales. Due to these differences across species, sol-gel parameters had to be optimized for each insect. The small physical size of the scales (~30×30 μm) presented difficulties in the

handling of the samples. Work removing, opening, and infiltrating many 100s of scales was delicately done with the tip of a razor blade and the help of an optical microscope.

Some example optical reflectance spectra and SEM images are shown in Figure 2.4. Each of the samples has a well-defined reflection peak centered in the wavelength range between 500 and 550 nm. While this might seem surprising, given how different the structures are, one has to consider that optical reflectance measurements of photonic crystals reveal only the existence of at least one photonic stop gap normal to the probe direction. The case of natural photonic crystals is further complicated by the fact that the structure contains a pixelated arrangement of crystal directions, meaning that several directions are measured at a given time. Since the crystal directions are pixelated, there is no way to experimentally tell if a peak is due to a single stop gap, multiple overlapping gaps, or a full photonic band gap. Additionally, as I will show in the next chapter, in inverse opals, a continuum of structural parameters can lead to identical peak positions. The issue of characterization of the structural and photonic properties is addressed in detail in the following chapter. The most concrete experimental measurement of photonic crystal quality comes from SEM images.

Hollow silica structures, for example Figure 2.4a, were found in general to be thin-walled with excellent uniformity of shell thickness. It was possible to vary the shell thickness to produce structures with walls almost transparent in SEM to thick-walled structures by using silica-sol solutions with varying viscosity by adding various amounts of ethanol (from 2 to 10 mL). The assessment of wall thickness is qualitative however, because accurate measurements of wall thickness were not possible from SEM images.

In spite of their thin wall, silica inverse structures were structurally robust enough to be moved using a razor blade without breaking.

Solid silica structures, for example Figure 2.1 and Figure 2.4b, had a grainier texture as was revealed by SEM imaging. With the inclusion of the polymer F127 into the silica precursor sol, the sol-gel recipe above resulted in solid structures even when the amount of ethanol ranged from 4 mL to 12 mL. Using this approach, robust mesostructured hybrid silica inverse imprints of the beetle photonic crystal were fabricated. The inverse structures have a highly accessible framework with an overall shrinkage of the lattice constant of less than 5%. When less than 4 mL of ethanol was added, the silica-sol did not appear to infiltrate the scales completely; possibly due to the increased viscosity.

In comparison to the hollow silica structures, uniform hollow titania structures (Figure 2.4c) were considerably more difficult to make. These structures seemed particularly sensitive to the type of scale used and the way the scales were pretreated. In general the experimental parameters were found to vary significantly between scales coming from different species (the recipe given above applies to the weevil *P. moniliferus*). Failed experiments typically resulted in scales with nonuniform hollow areas mixed with solid areas, see for example Figure 2.5. Interestingly, these materials exhibited remarkable structural stability. While the other structures would crack along lattice planes when disturbed with a razor, these required much more effort to break open so that SEM images could be obtained.

The solid titania inverse structures (Figure 2.4d) were obtained when TFA was omitted from the sol-gel recipe, and occurred over a broader range of parameters

compared to the hollow titania inverse structures. The lattice constant was reduced by about 20% in these samples due to shrinkage, however the volume fraction of the solid remained about the same as the air fraction in the original scale 40±5%. These samples are the most promising for future spectroscopic studies because their relatively high refractive index, estimated from band structure calculations as 2.1±0.1, and low filling fraction result in photonic stop gaps that overlap in all but one crystal direction.

The experimental procedure used in the synthesis of the titania positive replica induced titania nano-crystallization, producing a dense polycrystalline anatase titania framework with a refractive index of 2.3 ± 0.1.[16] Jeremy Galusha conducted a range of structural and optical characterization studies on the double-imprint titania replica with my assistance.[16] Structural studies were performed by focused ion beam milling and scanning electron microscopy imaging, revealing the diamond-based photonic lattice with ABC stacked layers of hexagonally ordered air cylinders in a surrounding high-dielectric matrix was excellently preserved after the double-templating procedure (Figure 2.6a,b). Moreover, shrinkage of the structure was kept below 15%, giving a final lattice constant of 366 ± 24 nm and high-dielectric volume fractions between 30% and 40%. The corresponding calculated band structure diagram is shown in Figure 2.6c and revealed a 5% wide (gap-to-mid-gap ratio) complete band gap. The optical properties of the diamond-structured titania replica were examined by multidirectional reflectance microspectroscopy measurements. Reflectance spectra were recorded normal or slightly off-normal to particular crystal axes of the diamond-based lattice. In addition, to cover an even larger range of directions, a series of angle-dependent reflectance spectra covering a 30° range were collected, as shown in Figure 2.7. The obtained series of intensity-

normalized spectra displayed no significant dependence of the reflectance peak position on the recording-angle in accordance with calculations.[16]

While the structural and optical results of the positive titania replica are extremely promising, it was found that synthesis of this structure was challenging having a yield of only a few percent. This yield is perhaps due to the apparent sensitivity of the interaction of titania sol with the silica inverse framework. The second step in the synthesis was highly tuned and worked only for a very narrow set of parameters that seem to change with seasonal variations in the lab environment, where the indoor humidity in Utah varies from ~10% in the winter to up to 50% in the summer. Although the calculated 5% complete photonic band gap for an ideal—surface and defect-free—lattice is most likely too narrow to stay open in a real sample. It was in response to these challenges that I explored the other four replica structures described above, which are all accessible through a single templating step.

Conclusion

The simplicity of sol–gel templating and the readily available biological templates with lattices not available by current engineering methods make bioreplication the method of choice for the fabrication of new photonic crystals operating at visible frequencies. We demonstrated the versatility of sol–gel chemistry as a useful tool for tuning the lattice type and parameter of replicas obtained from a single biotemplate. Hollow and solid inverse silica, hollow and solid inverse titania, and solid titania replica structures were made for biological photonic structures taken from a variety of insects. While optical reflectance is a useful tool to qualitatively understand a photonic crystal's

properties, a deeper understanding of photonic effects requires a more detailed investigation. Characterization by modeling photonic crystal structures – using structural parameters measured from SEM images – in conjunction with photonic band structure and density of optical states calculations will provide important insight into the potential of these structures. These types of modeling and characterization studies will be described in detail in the following chapter.

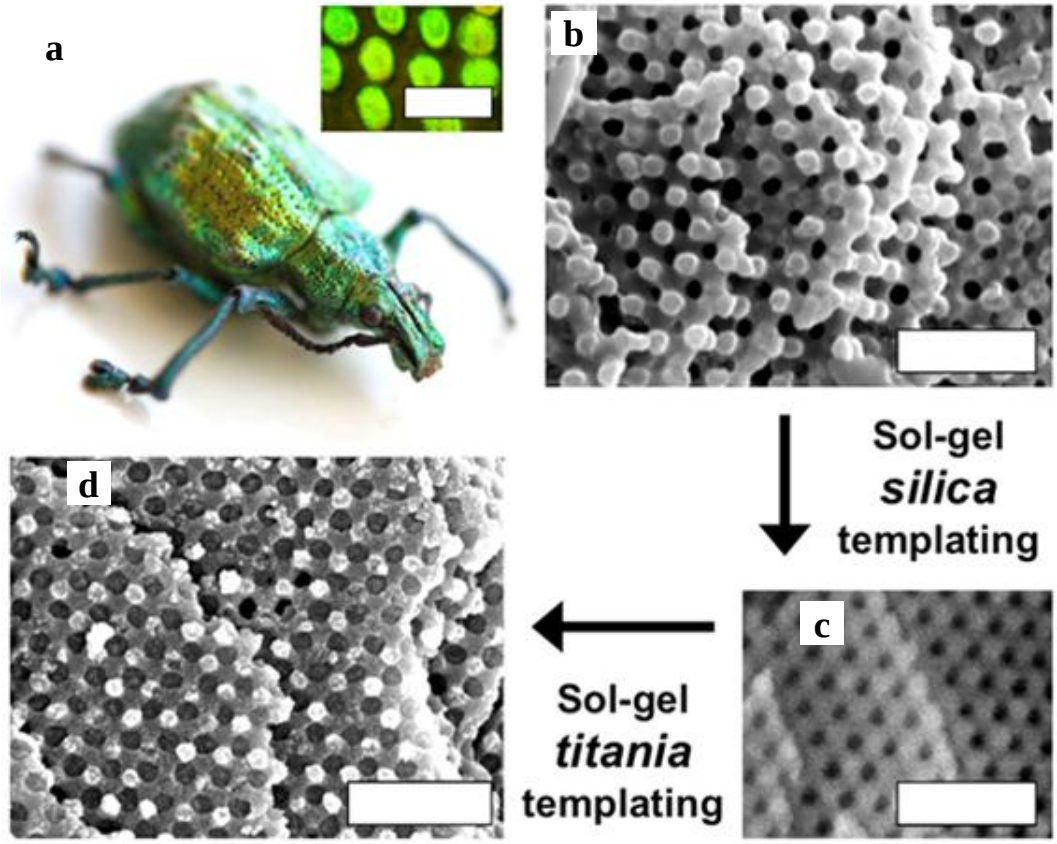

Figure 2.1 Illustration of the double-imprint sol-gel biotemplating route for converting photonic scales of the weevil *L. augustus* into high-dielectric titania replica. a) Weevil *L. augustus* and its green colored photonic scales (inset). b, c, d) Scanning electron microscopy images of a cross-sectional views of b) the original biopolymeric photonic structure, c) the inverse structure made of hybrid silica and d) the titania replica templated from the intermediary hybrid silica structure. Scale bars are 200 μm (a) and 1 μm (b, c, d). Adapted from 16, Copyright Wiley-VCH Verlag GmbH & Co. KGaA. Reproduced with permission.

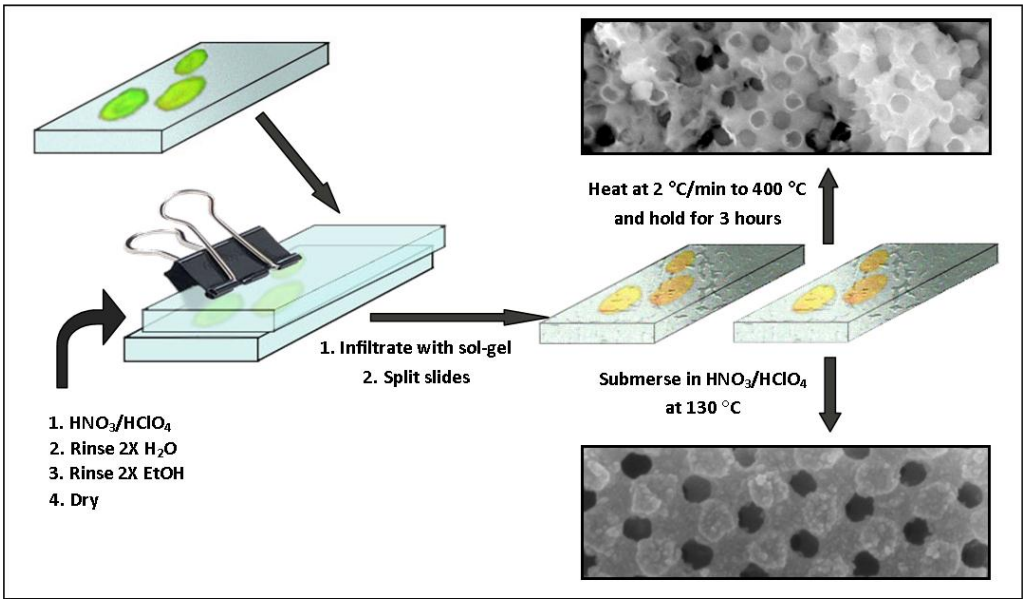

Figure 2.2 Schematic of sol-gel biotemplating process. Exoskeletal scales are scraped onto a slide, breaking them open. The scales are sandwiched between another slide while they are treated with acid, cleaned, and infiltrated with sol-gel. The cuticular scale is removed from the chitin/sol-gel composite by acid etching or thermal degradation. Inset SEM images are of silica shell structure (top) and silica inverse structure (bottom).

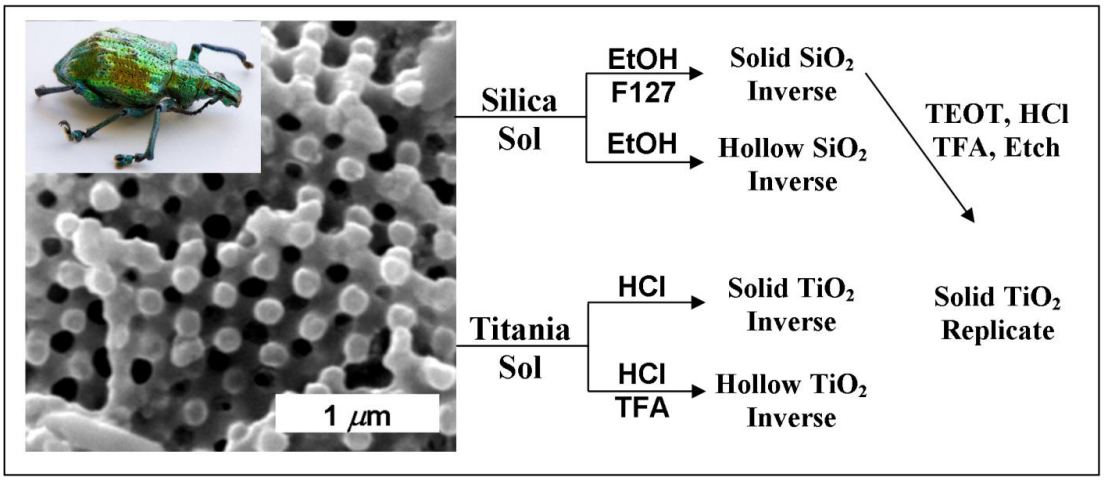

Figure 2.3 Illustration of the variety of structures available from a single template. (Left) SEM image of the biopolymeric photonic crystal found in the weevil *Lamprocyphus augustus* (inset). (Right) Schematic showing the variety of replica structures accessible from a single biotemplate via sol–gel infiltration chemistry. Reprinted from reference 17, with permission from Elsevier.

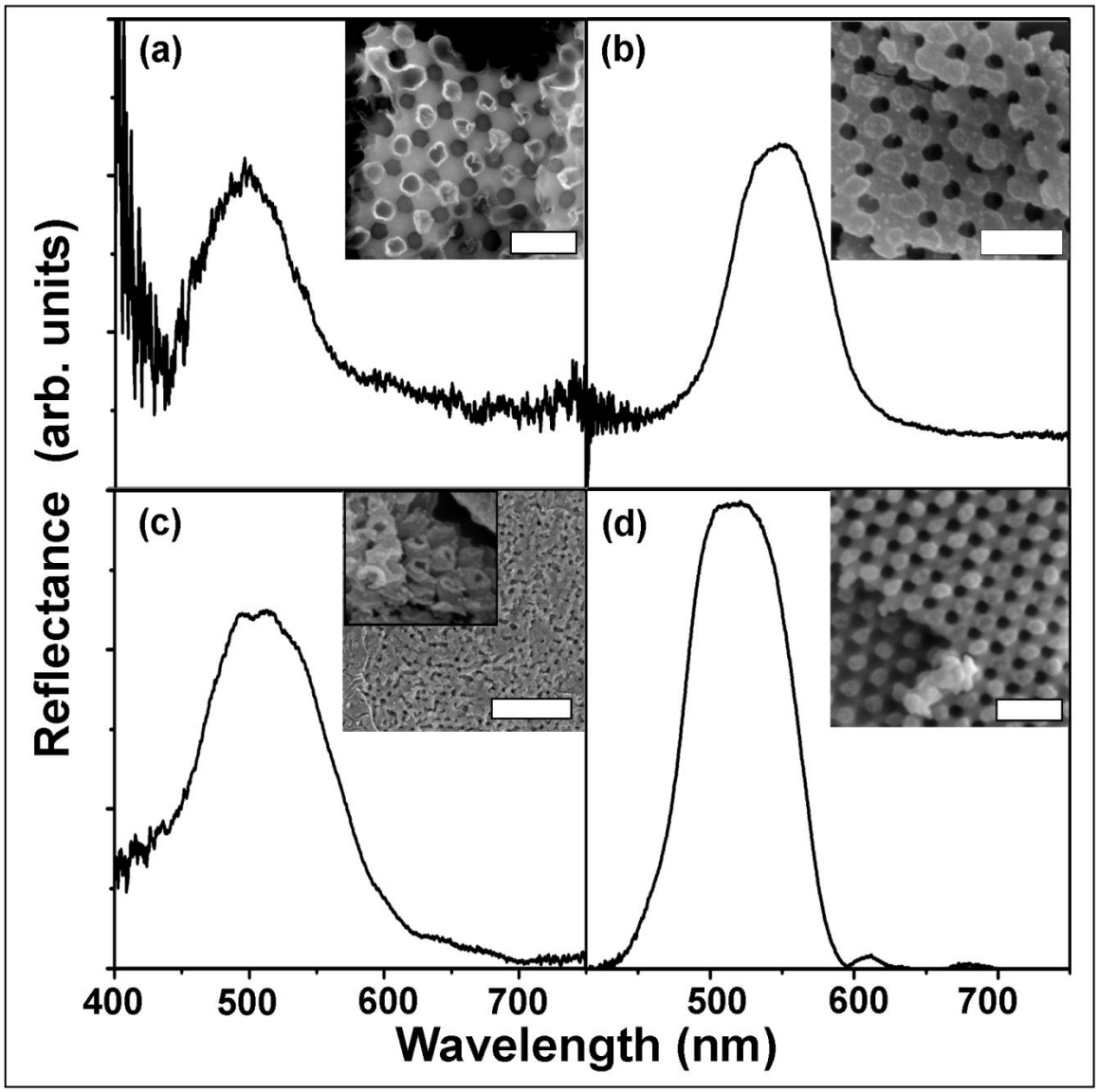

Figure 2.4 Example SEM images and reflections from a variety of structures produced. Optical reflection spectra of (a) a silica hollow inverse replica, (b) a silica solid inverse replica, (c) a titania hollow inverse replica and (d) a titania solid inverse replica. Insets show the corresponding SEM images. Scale bars in (a), (b) and (d) are 500 nm, the scale bar in (c) is 2 μm, and the base of the inset in (c) is 750 nm. Reprinted from reference 17, with permission from Elsevier.

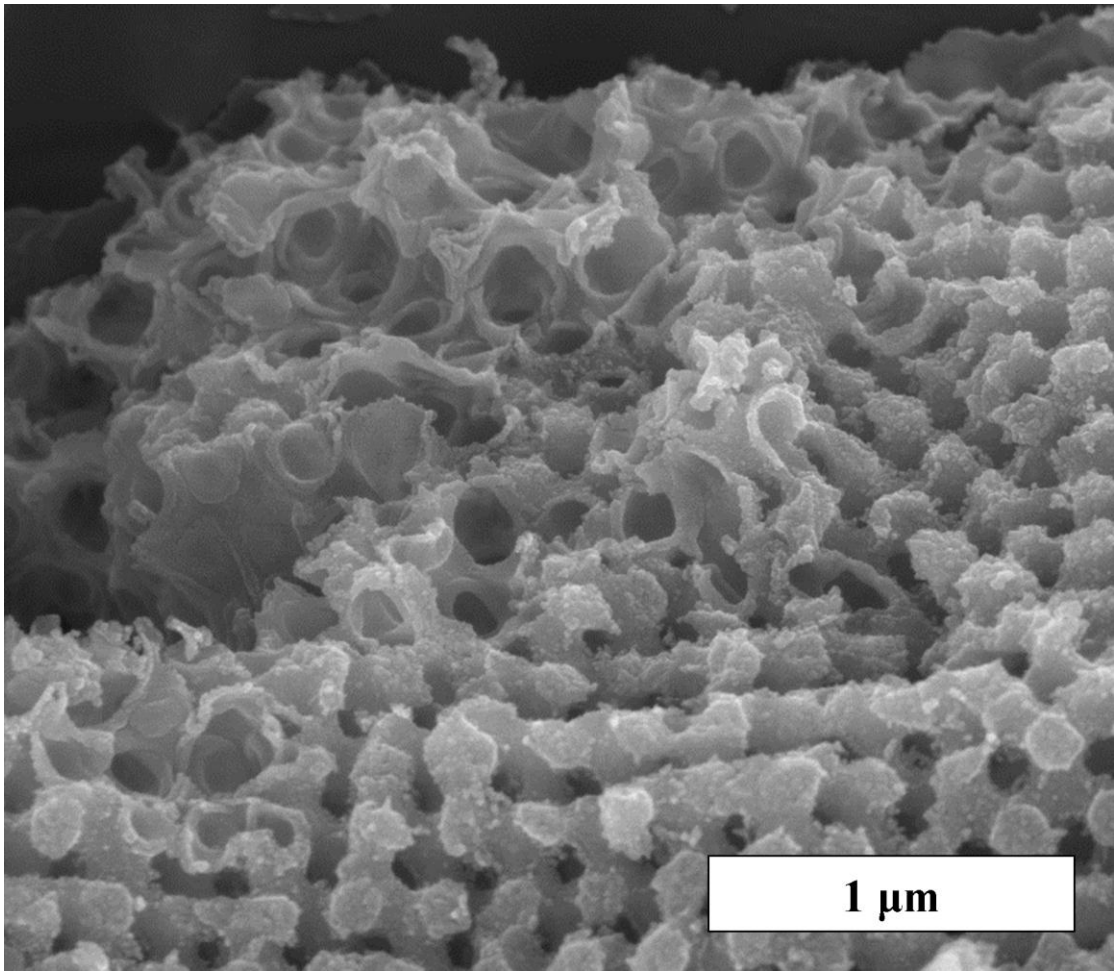

Figure 2.5 Hollow/solid composite titania inverse structure. This type of structure, with some areas clearly hollow and others clearly solid was found over a broad range of bioreplication parameters.

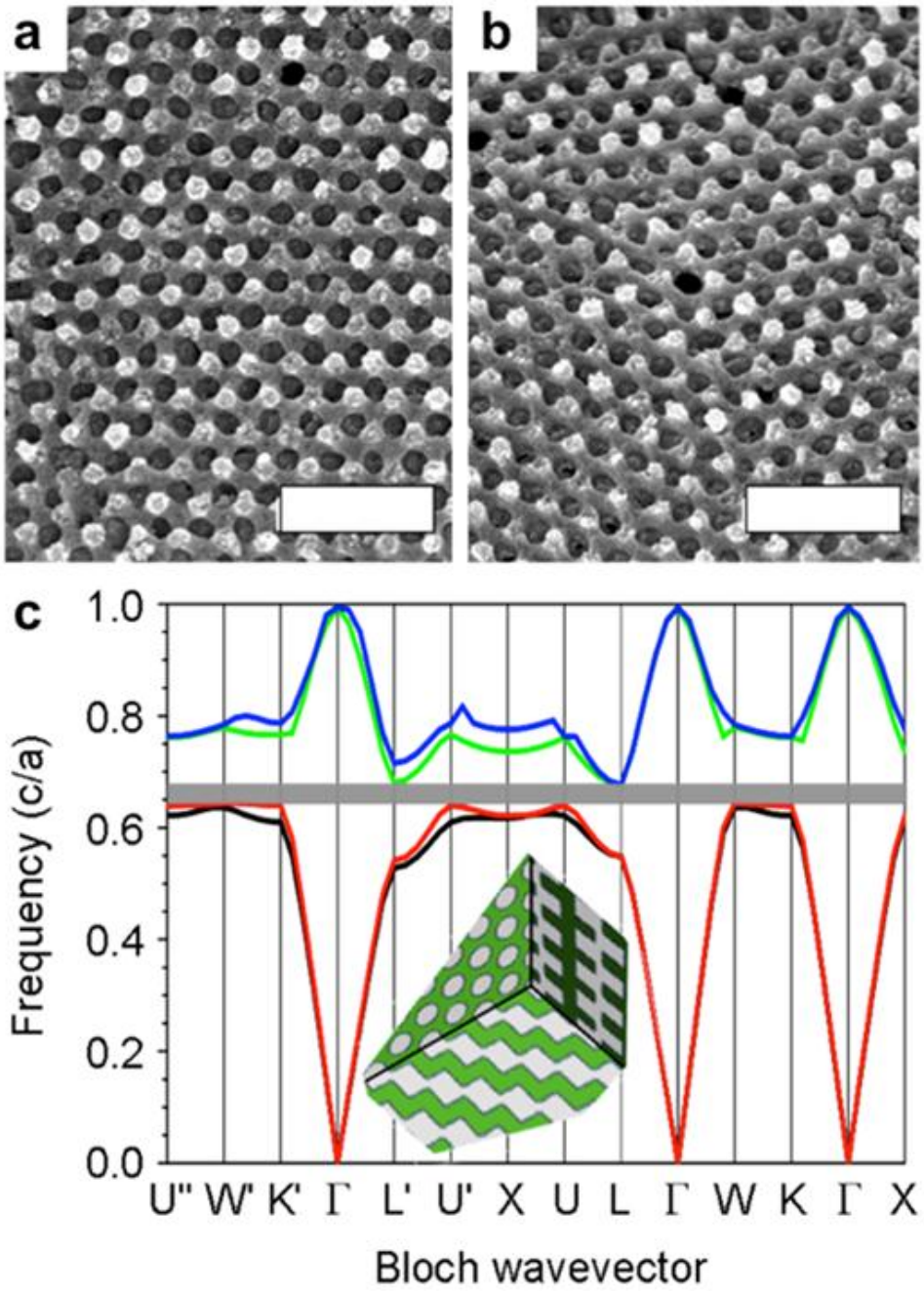

Figure 2.6 a) Scanning electron microscopy cross-sectional view of a biotemplated diamond-based titania photonic crystal lattice. b) Tilted view of the same titania structure. c) Corresponding calculated band-structure diagram. The complete photonic band gap between the second and third band is indicated by a gray rectangle. Scale bars in (a) and (b) are 1 μm. Adapted from 16, Copyright Wiley-VCH Verlag GmbH & Co. KGaA. Reproduced with permission.

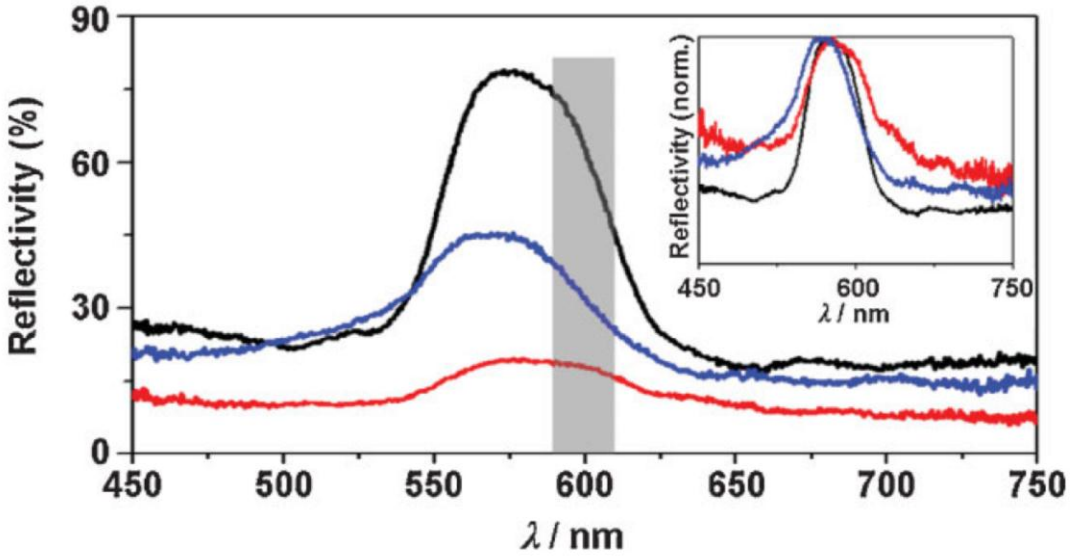

Figure 2.7 Reflection measurements spanning a 30° range of angles collected from a diamond structured titania replica. The black line is normal incidence, the blue is −15° off normal, and the red line is +15° off normal. Normalized plots are shown in the inset, highlighting their almost identical reflection peak positions. Adapted from 16, Copyright Wiley-VCH Verlag GmbH & Co. KGaA. Reproduced with permission.

References

1. Bone, R. A.; Lee, D. W.; Norman, J. M., Epidermal Cells Functioning as Lenses in Leaves of Tropical Rain-Forest Shade Plants. *Appl. Opt.* **1985,** *24* (10), 1408-1412.

2. Lee, D. W., Ultrastructural Basis and Function of Iridescent Blue Colour of Fruits in Elaeocarpus. *Nature* **1991,** *349* (6306), 260-262.

3. Arikkath, J.; Campbell, K. P., Auxiliary Subunits: Essential Components of the Voltage-Gated Calcium Channel Complex. *Curr. Opin. Neurobiol.* **2003,** *13* (3), 298-307.

4. Glover, B. J.; Whitney, H. M., Structural Colour and Iridescence in Plants: The Poorly Studied Relations of Pigment Colour. *Ann. Bot. London* **2010,** *105* (4), 505-511.

5. Dolphin, A. C., β Subunits of Voltage-Gated Calcium Channels. *J. Bioenerg. Biomembr.* **2003,** *35* (6), 599-620.

6. Mäthger, L. M.; Denton, E. J.; Marshall, N. J.; Hanlon, R. T., Mechanisms and Behavioural Functions of Structural Coloration in Cephalopods. *J. R. Soc. Interface* **2009,** *6* (Suppl 2), S149-S163.

7. Srinivasarao, M., Nano-Optics in the Biological World: Beetles, Butterflies, Birds, and Moths. *Chem. Rev.* **1999,** *99* (7), 1935-1962.

8. Vukusic, P.; Sambles, J. R., Photonic Structures in Biology. *Nature* **2003,** *424* (6950), 852-855.

9. Seago, A. E.; Brady, P.; Vigneron, J.-P.; Schultz, T. D., Gold Bugs and Beyond: A Review of Iridescence and Structural Colour Mechanisms in Beetles (Coleoptera). *J. R. Soc. Interface* **2009,** *6* (Suppl 2), S165-S184.

10. Martín-Palma, R. J., Biomimetization of Butterfly Wings by the Conformal-Evaporated-Film-By-Rotation Technique for Photonics. *Appl. Phys. Lett.* **2008,** *93* (8), 083901.

11. Izumi, M.; Sweeney, A. M.; DeMartini, D.; Weaver, J. C.; Powers, M. L.; Tao, A.; Silvas, T. V.; Kramer, R. M.; Crookes-Goodson, W. J.; Mäthger, L. M.; Naik, R. R.; Hanlon, R. T.; Morse, D. E., Changes in Reflectin Protein Phosphorylation are Associated with Dynamic Iridescence in Squid. *J. R. Soc. Interface* **2010,** *7* (44), 549-560.

12. Jorgensen, M. R.; Bartl, M. H., Biotemplating Routes to Three-Dimensional Photonic Crystals. *J. Mater. Chem.* **2011,** *21* (29), 10583-10591.

13. Prum, R. O.; Quinn, T.; Torres, R. H., Anatomically Diverse Butterfly Scales All Produce Structural Colours by Coherent Scattering. *J. Exp. Biol.* **2006,** *209* (4), 748-765.

14. Galusha, J. W.; Richey, L. R.; Gardner, J. S.; Cha, J. N.; Bartl, M. H., Discovery of a Diamond-Based Photonic Crystal Structure in Beetle Scales. *Phys. Rev. E* **2008,** *77* (5), 050904(1-4).

15. Galusha, J. W.; Richey, L. R.; Jorgensen, M. R.; Gardner, J. S.; Bartl, M. H., Study of Natural Photonic Crystals in Beetle Scales and their Conversion into Inorganic Structures via a Sol-Gel Bio-templating Route. *J. Mater. Chem.* **2010,** *20* (7), 1277-1284.

16. Galusha, J. W.; Jorgensen, M. R.; Bartl, M. H., Diamond-Structured Titania Photonic-Bandgap Crystals from Biological Templates. *Adv. Mater.* **2010,** *22* (1), 107-110.

17. Jorgensen, M. R.; Yonkee, B. P.; Bartl, M. H., Solid and Hollow Inorganic Replicas of Biological Photonic Crystals. *Scripta Mater.* **2011,** *65* (11), 954-957.

18. Jorgensen, M. R.; Yonkee, B.; Bartl, M. H. In *Strong Modification of Density of Optical States in Biotemplated Photonic Crystals*, SPIE 8071, Prague, Czech Republic, Bertolotti, M., Ed. SPIE: Prague, Czech Republic, 2011; pp 807109-9.

19. Zhao, D.; Yang, P.; Melosh, N.; Feng, J.; Chmelka, B. F.; Stucky, G. D., Continuous Mesoporous Silica Films with Highly Ordered Large Pore Structures. *Adv. Mater.* **1998,** *10* (16), 1380-+.

20. Galusha, J. W.; Tsung, C. K.; Stucky, G. D.; Bartl, M. H., Optimizing Sol-Gel Infiltration and Processing Methods for the Fabrication of High-Quality Planar Titania Inverse Opals. *Chem. Mater.* **2008,** *20* (15), 4925-4930.

CHAPTER 3

METHODS FOR THE CHARACTERIZATION OF PHOTONIC CRYSTALS

Introduction

The idea of photonic crystals was initially developed purely as a theoretical concept.[1-2] Therefore, predicted properties of photonic crystals were based on ideal structures of infinite size, with no defects, and homogeneous composition.[3-7] These models, however, are in stark contrast to real photonic crystal samples.[8-19] Naturally, real photonic crystals are of finite size and thus are characterized by bulk and surface properties. Furthermore, no real photonic crystal possesses a perfect lattice (i.e., point, line and plane lattice defects need to be considered) or is built up by a framework with perfectly homogeneous composition and interface. Unfortunately, these differences between ideal and real photonic crystal structures were not always taken into consideration in early experimental characterization studies of real samples.[20-21] This led to several unfortunate misconceptions and incorrect claims of complete and partial photonic band gaps.

Even today, some 25 years after the first conceptualization of photonic crystals, researchers are still adapting to new findings and challenges dealing with the correct characterization of photonic crystals.[22-24] Questions regarding what makes a "good" photonic crystal are still debated in the literature. The role of nonidealities in photonic

crystal structures is not completely resolved, though the issue has grown more important as creative new ways to produce nonideal photonic crystals are being discovered in contrast to the highly controlled photonic crystals produced using top-down synthetic methods.[25-27] Initially, a lot of weight was placed on a photonic crystal's reflection properties. However, as understanding of photonic crystals has matured, it has become clear that these measurements have serious limitations. Many of these will be discussed below in the context of a photonic crystal model system, inverse opals. The most meaningful characterizations of photonic crystals rely on a combination of measurements from scanning electron microscopy (SEM) images, optical reflection spectroscopy, and various modeling and theoretical studies. In this chapter, I will explain how optical reflection spectroscopy measurements are made, and how some of the limitations of these measurements are addressed. The process of modeling a photonic crystal from SEM images, calculating its photonic band structure diagram, and using this information in connection with reflection measurements will be described. Finally the limitations of the band structure diagrams will be discussed.

Optical Reflection Measurements and Photonic Crystal Properties

One of the core ideas of photonic band structure theory is that within a photonic crystal there can exist certain frequency ranges for which light is classically forbidden to propagate in specific directions. These frequency ranges are called stop gaps, a one-directional band gap. If there exists a range of frequencies for which light propagation is forbidden over all directions, the crystal is said to have a full (or complete) photonic band

gap. A full photonic band gap is a cumulative effect, resulting from stop gaps in all directions where the frequency ranges overlap. An important consequence of optical stop gaps is that if broadband light is incident on a photonic crystal in the direction of a photonic stop gap, then the frequency range of light forbidden by the gap will be reflected from the crystal, due to constructive interference. In the case of a full photonic band gap, light would be reflected over this frequency range regardless of the angle of incidence.[28] Optical reflection spectroscopy is therefore a valuable technique to study photonic crystals: In theory, it can give information about the frequency ranges in which stop gaps are present and, if the crystal orientation is known, also about the directional position of these stop gaps.

Optical reflection measurements are typically conducted by measuring the intensity of reflected light from the sample in reference to an efficient broadband reflector. Since the samples are often very small and are not completely homogeneous over large areas, reflection measurements are generally done using a microscope. In addition, a pinhole can be placed at the position of the image plane to isolate small areas of the sample and study defects and irregularities by scanning the sample surface. A schematic diagram of the reflectance measurement setup used in this thesis is shown in Figure 3.1. White light was focused onto the sample surface or into the sample using a 20× objective (N.A. 0.45). the same objective was also used to collect the reflected light. The area of image measured from the objective was narrowed using a pinhole or an adjustable aperture positioned in the image plane. Light passing the pinhole/aperture is then fiber-coupled into an Ocean Optics USB4000 vis/NIR spectrometer and analyzed. A

high-reflectance broadband mirror is used as standard. Using this set-up, the probed area of the photonic crystal samples was around 10 μm^2.

As mentioned, early characterization studies of photonic crystals relied heavily on optical reflectance measurements as an indirect measurement of photonic band gaps. The idea was very simple: By measuring reflections over a range of angles, various stop gaps can be probed. If stop gaps in all directions overlap in a certain frequency range, a complete band gap must be present in the photonic crystal. However, the complications in real samples arise from surface effects (surface-guided modes and random light scattering at the photonic crystal surface), exact sample positioning to ensure that ALL directions are probed, and the fact that light focused by a lens/objective is not a perfect plane wave but has a certain diffraction cone.[29-31] The interpretation of experimentally obtained optical reflection bands is further complicated by the fact that detailed structural parameters of a given real photonic crystal sample are often unknown; for example, exact refractive index of the high-dielectric framework, filling fractions of the dielectrics, crystal lattice constants and shape of the lattice objects (i.e., spherical, cylindrical, oblong etc.). If more than one structural parameter of a photonic crystal is unknown or known only within a certain range, then there exist many possible combinations of lattice types and dielectric properties that can give rise to an observed reflection peak. In the following section the limitations of optical reflection measurements to determine the band structure properties of a photonic crystal will be discussed in the context of a well know photonic crystal example: inverse opals—a face centered cubic lattice of closed-packed air spheres in a high-dielectric matrix.

Challenges and Limitations of Optical Reflection Measurements

According to Bragg's law applied to inverse opal photonic crystals, three structural properties determine the peak wavelength of light reflected by a photonic crystal: the distance between repeating units in the probed direction, the refractive indices of the dielectric compounds building up the photonic crystals, and their respective filling fractions. The lattice structure of most photonic crystals is composed of only two different dielectrics: a framework of a high-dielectric compound surrounded by air (the low-dielectric compound). In this case, Bragg's law is given as:

$$\lambda_{max} = 2d\sqrt{f \cdot n_s^2 + (1-f)n_{air}^2} = 2d \cdot n_{eff} \tag{3.1}$$

Here, λ_{max} is the wavelength position of the optical reflection peak, d is the interlayer spacing in the probed direction, f is the high-dielectric filling fraction, n_s is the high-dielectric refractive index, n_{air} is the refractive index of air (n_{air} = 1), and n_{eff} is the effective refractive index of the composite structure.

When inverse opals are made from a synthetic opal template using sol-gel chemistry, two of these parameters (the refractive index and filling fraction) are known only within a relatively broad range. This is because when sol-gel chemistry is used to make an inverse opal photonic crystal there are generally voids that can introduce significant uncertainty in the structure's filling fraction. Figure 3.2 shows an SEM image of an example titania inverse opal. While geometric arguments would make the solid volume fraction of an inverse-opal 26%, it is apparent that the volume fraction is reduced by holes connecting the air-spheres and voids (see the contrast enhanced inset of Figure 3.2). While the contribution that interconnecting holes have to the volume fraction is easily approximated in calculations, the contribution of the voids is more difficult. The

volume occupied by the voids in between spheres can be found if the structure is modeled as if the air spheres are coated with an interconnected shell of a solid, but the void volume is highly sensitive to the thickness of the solid shell and the shell thickness can only be approximated from SEM images.

The refractive index also has a degree of uncertainty because the inherent porosity of solids produced by sol-gel chemistry is often known to only a certain degree. Since the refractive index of three-dimensional frameworks such as those in photonic crystals cannot be measured directly, one relies on ellipsometry measurements on thin films; however, it is not established that the refractive index of a sol-gel compound is independent of its processing method (thin film dip-coating vs. templating/casting). The combined uncertainty of these two parameters, the filling fraction and refractive index, leads to a situation where there are many combinations that agree with reflection measurements.

Photonic Band Structure Diagrams

The limitations of reflection measurements are partially addressed by going beyond Bragg's law to a higher level of theory in understanding a photonic crystal's properties. As described in Chapter 1, the directionally dependent optical modes inside a photonic crystal may be found by casting Maxwell's equations as an eigenvalue problem.[28] These calculations can be executed for a digitally modeled structure in three dimensions using MIT's photonic bands software package (MPB).[32] MPB was written by Joannopoulos and coworkers and is offered as open source to the photonic crystal community (http://ab-initio.mit.edu/mpb). It is a powerful tool for the theoretical

analysis of photonic crystal structures with the built in capability to incorporate complex geometric structures, calculate three dimensional electronic energy density plots, and maximize photonic band gaps over a set of parameters. It is easy to interface with MPB using scripts, so that MPB processes can be used in connection with other programs as was done to calculate the density of optical states, which is described in the following chapter.

The digital model of the photonic crystal lattice is defined by the symmetry of the crystal and the geometry of the objects occupying the lattice points, which are built from a set of overlapping simple shapes. For example, in an inverse opal the symmetry of the lattice is specified using the primitive lattice vectors for the face centered cubic crystal lattice. To account for the interconnecting holes and voids in a real inverse opal, the geometry at the lattice points is specified by sequentially writing a series of objects. First, the entire space is defined as air to give a uniform clean slate, and then a solid titania sphere is written with its center at the lattice point origin. At this point, the structure would look like an FCC arrangement of solid intersecting spheres with small triangular vacancies where the spheres do not quite overlap. To make the structure hollow, air spheres are written into the solid spheres, but with a slightly smaller radius to give a shell-like structure. Finally, the holes that interconnect the air spheres are added. A lattice structure modeled in this way is shown in Figure 3.3, along with the SEM image it was based on, and the resulting photonic band structure diagram.

The inverse opal sample shown in Figures 3.2 and 3.3 was created from an artificial opal made using vertical deposition techniques. This deposition technique results in films of opal crystals with their 111 lattice direction normal to the film surface,

corresponding to the *Γ*-*L* stop gap of the photonic crystal band structure pointing normal to the film surface.[33-36] Therefore, it is this stop gap that leads to the inverse opal's measured reflection. If either the refractive index or volume fraction of the solid phase of the structure is known, the other parameter can be found by varying it to bring the reflection band position and calculated stop gap into agreement with each other. However, if both parameters have uncertainty, as they generally do in real samples, then correlation between the reflection measurement and band diagram becomes ambiguous. Figure 3.3 shows the predicted reflection peak from the *Γ*-*L* stop gap for a range of framework refractive indices and volume fractions of the dielectric components. The narrow line through the middle of the graph shows the range in which the predicted reflection agrees with the measured peak at 450 nm, verifying that there is a continuum of parameters that yield a photonic crystal agreeing with experiment. This problem could be overcome in samples where multiple stop gaps are available to probe, because each stop gap varies differently with refractive index and volume fraction, narrowing the range of parameters possible that allow all the different stop gaps to agree with measurements. However, this comes back to the problem of exactly orienting small samples to experimentally measure reflection properties in predetermined directions and also does not take into consideration uncertainties due to surface effects.

The Combination of Electron Microscopy, Optical Reflection Studies, and Calculations

The degree of accuracy in determining photonic crystal properties can be significantly enhanced through a coordinated combination of calculated photonic band

diagrams, multidirectional electron microscopy imaging, and optical reflection measurements on samples submersed in different solvents. For example, using measurements of structural parameters accessible through SEM images, the volume fraction of the inverse opal shown in Figure 3.3 is found to be between 14% and 19%. Figure 3.4 reveals that within this range, the refractive index of the solid can only be between 1.8 and 2.1 to give agreement with optical reflection measurements. Since the refractive index and volume fraction of the solid framework remain fixed regardless of the surrounding environment, but the wavelength position of the reflection band depends strongly on the refractive index contrast between the framework and surrounding phase, a variation of the surrounding's refractive index gives direct information regarding the framework refractive index and volume fraction. This can be seen by measuring the optical reflection properties of an inverse opal sample submersed in solvents with different, but well-known, refractive indices. Figure 3.5 shows the calculated reflectance due to the *Γ-L* stop gap for the inverse opal shown in Figure 3.3 in air, ethanol, and carbon disulfide as the low-dielectric component (surrounding phase). The colored lines show where calculations agree with the experimentally measured reflection. It is found that calculations and measurements over different low-dielectric components agree only for a narrow range of parameters with a filling fraction of 15.5±0.5% and a refractive index of 2.05±0.05. The developed method of combining different characterization tools thus significantly narrows the degree of uncertainty and gives valuable insights into photonic crystal properties.

However, it should be emphasized that the basis of this method is the calculated band structure diagram of a photonic crystal. This method thus relies on knowing the

structural parameters of photonic crystals to a high degree of accuracy. In cases in which this information is only limited available, such as in biological and biotemplated samples the uncertainty of the determined values can be significantly larger. Moreover, one of the original motivating properties of photonic crystals is their ability to inhibit or enhance spontaneous emission by controlling vacuum fluctuations, an effect that photonic band diagrams address in only a qualitative way. For example, the band diagram in Figure 3.3 shows that for the system studied there exists a stop gap in the Γ-L direction, a situation that clearly reduces the number of optical states in the crystal overall, but by how much? Other photonic systems we have studied include overlapping stop gaps in all directions except the Γ-L. The effect of a single nonoverlapping stop gap is not addressed in a photonic band structure diagram. To address this issue, the characterization of photonic crystals must be taken one theoretical step further to include the calculated density of optical states in addition to the other methods discussed previously.

Conclusion

The characterization of photonic crystals has been discussed in order from the most qualitative method, optical reflection spectroscopy, to a combination of multiple reflection spectra, SEM measurements, and photonic band structure calculations. It was shown that reflectance measurements do not adequately describe photonic crystal behavior, due to the many structural parameters that can yield similar reflections. This problem can be largely addressed by taking reflection measurements in various solvents, and correlating them with band structure calculations based on SEM images. While these characterization methods are useful in understanding many photonic crystal properties,

they neglect the control of vacuum fluctuations (or modification of the density of optical states), a critical property. A method for calculating the density of optical states within a photonic crystal will be described in the following chapter, the inclusion of which along with the other properties discussed provides the most complete characterization of photonic crystals currently available.

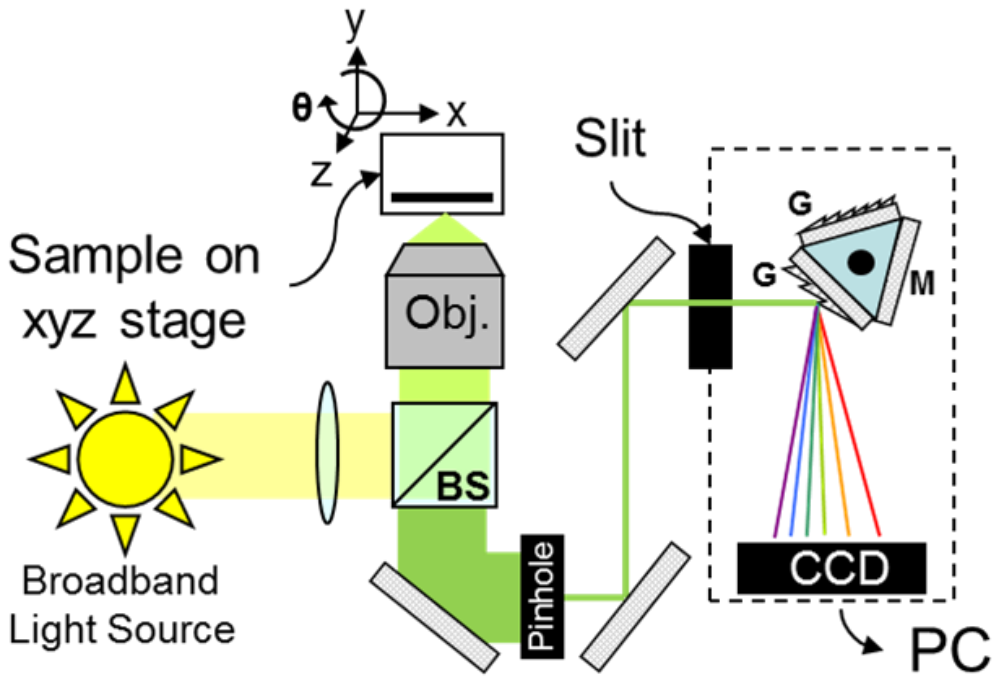

Figure 3.1 Schematic diagram of the reflection measurement experiemental setup. A broadband light source is directed through a mircroscope objective and focused onto the sample. An image of the reflected light is collected through the same objective, and narrowed by a pinhole. The area to be measured is positioned over the pinhole by oserving the image with an index card, or an optional camera and beam splitter. The area of the image narrowed by the pinhole is directed to a spectrometer for analysis.

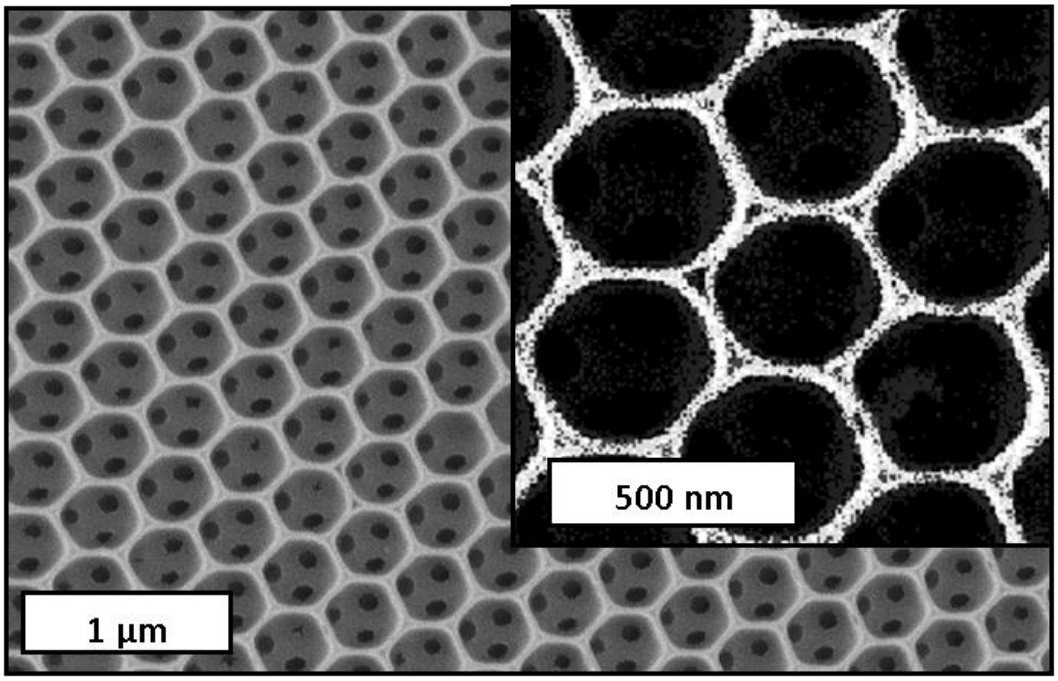

Figure 3.2 SEM image of titania inverse opal prepared using a polystyrene synthetic opal as a template. The small circular holes connecting air spheres are where the original polystyrene spheres touched eachother. The triangular shaped vacancies (highlighted in the contrast enhanced inset), are due to the way titania sol-gel coats the polystyrene spheres. The triangular vacancies cause an uncertainty of about ±5% in the volume fraction.

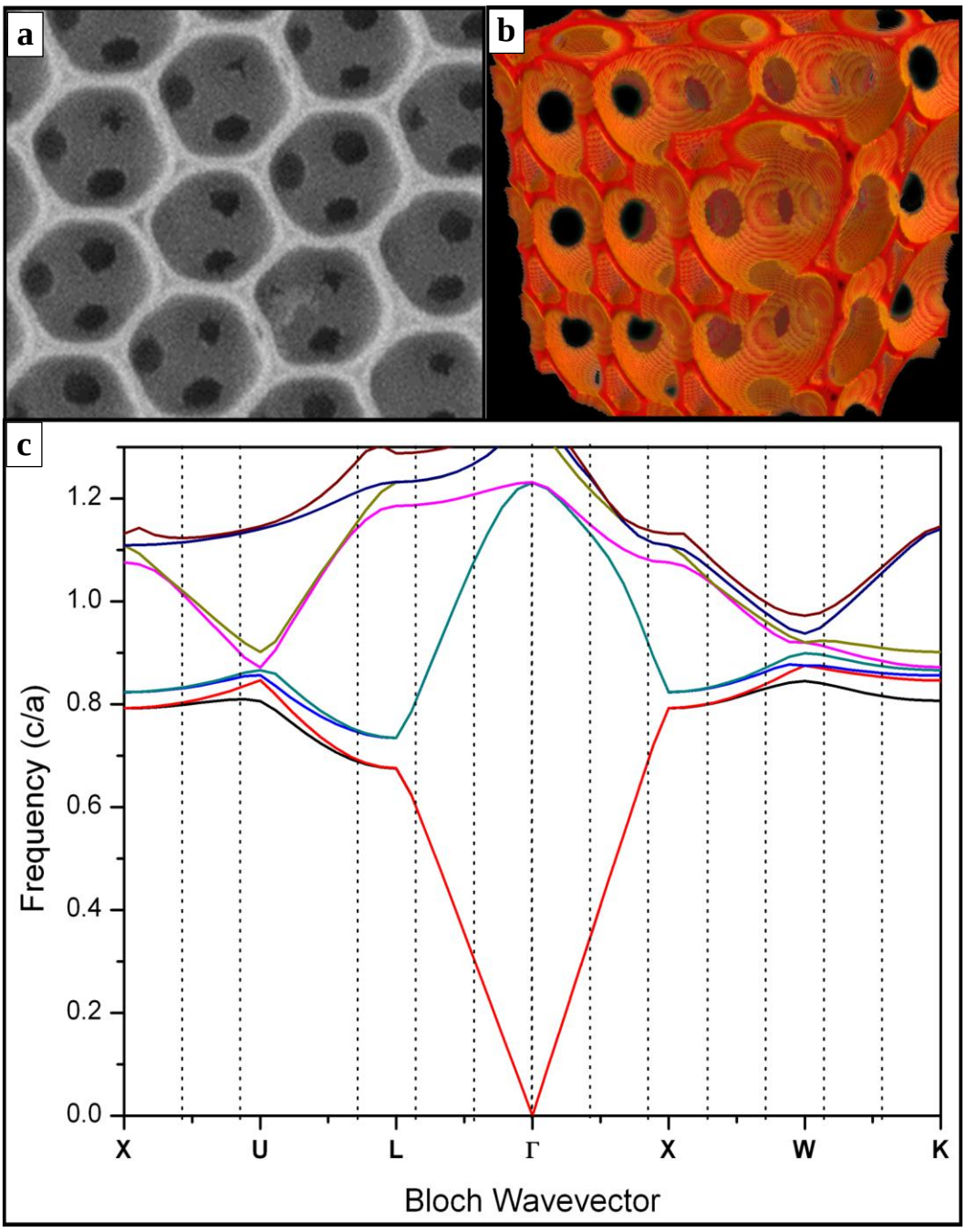

Figure 3.3 SEM image of titania inverse opal (a) and three dimensional model based on SEM measurements (b). The calculated band diagram (c) using the model includes a directional stop gap in the *Γ*-*L* direction.

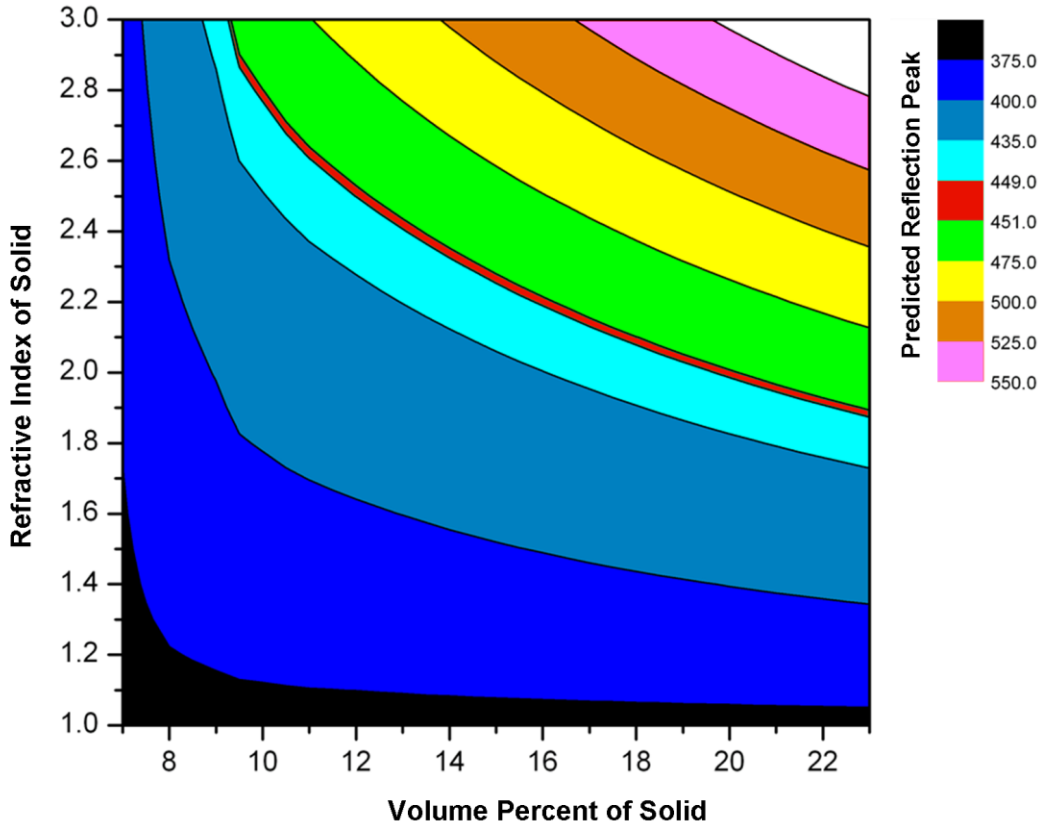

Figure 3.4 Plot of the predicted peak reflection of an inverse opal as a function of refractive index and filling fraction. In general, the peak reflection increases linearly with refractive index as predicted by Bragg's law. The narrow red band shows where the calculated reflection agrees with the experimental value of 450±1 nm, for this sample in air.

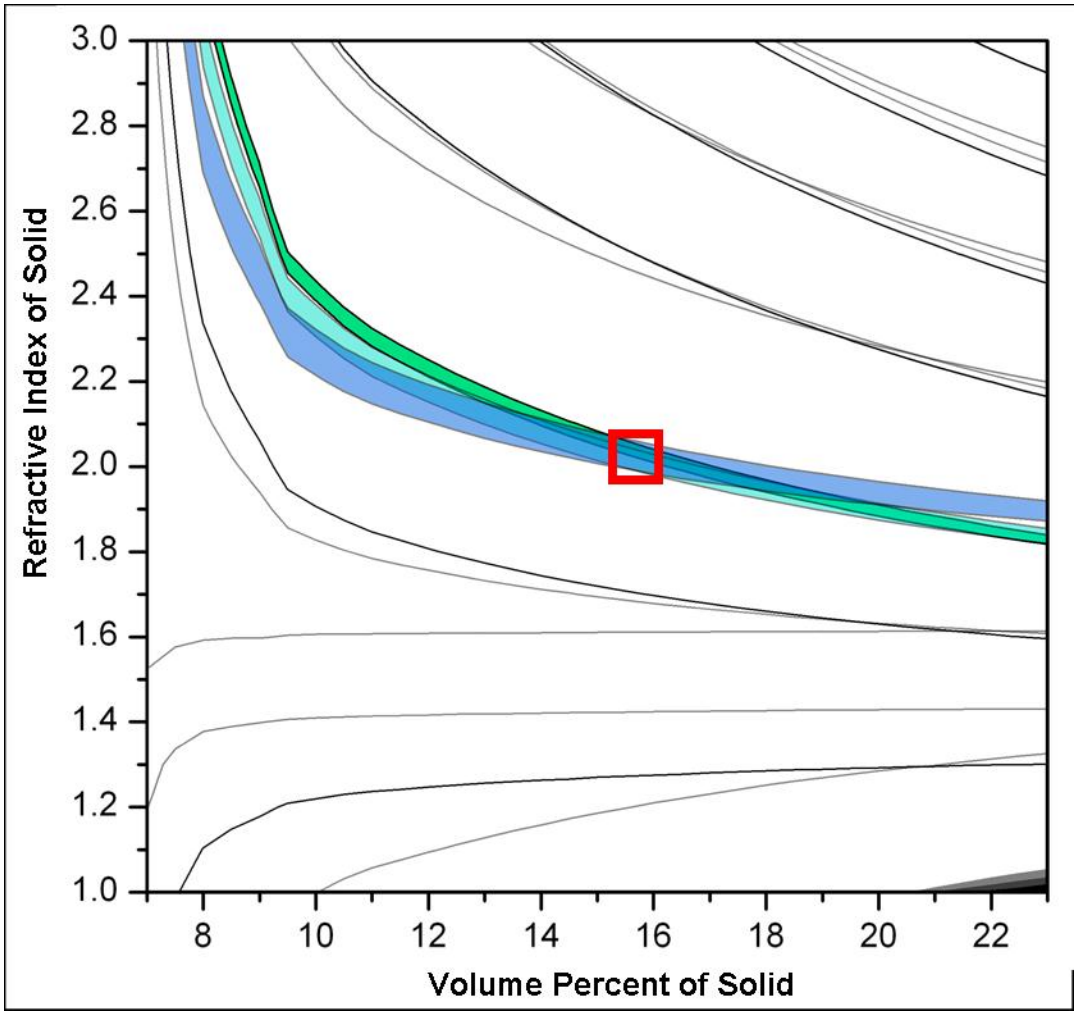

Figure 3.5 Overlapping plots showing the correlation between the calculated reflection peak and experimentally observed reflection for a titania inverse opal in air, submersed in ethanol, and submersed in carbon disulfide. The curves intersect at the refractive index and filling fraction corresponding to the sample, greatly narrowing the uncertainty in these properties.

References

1. John, S., Strong Localization of Photons in Certain Disordered Dielectric Superlattices. *Phys. Rev. Lett.* **1987,** *58* (23), 2486.

2. Yablonovitch, E., Inhibited Spontaneous Emission in Solid-State Physics and Electronics. *Phys. Rev. Lett.* **1987,** *58* (20), 2059.

3. Ho, K. M.; Chan, C. T.; Soukoulis, C. M., Existence of a Photonic Gap in Periodic Dielectric Structures. *Phys. Rev. Lett.* **1990,** *65* (25), 3152.

4. Yablonovitch, E.; Gmitter, T. J.; Leung, K. M., Photonic Band Structure: The Face-Centered-Cubic Case Employing Nonspherical Atoms. *Phys. Rev. Lett.* **1991,** *67* (17), 2295.

5. Joannopoulos, J. D.; Villeneuve, P. R.; Fan, S., Photonic Crystals: Putting a New Twist on Light. *Nature* **1997,** *386* (6621), 143-149.

6. Busch, K.; John, S., Photonic Band Gap Formation in Certain Self-Organizing Systems. *Phys. Rev. E* **1998,** *58* (3), 3896.

7. Maldovan, M.; Thomas, E. L., Diamond-Structured Photonic Crystals. *Nat. Mater.* **2004,** *3* (9), 593-600.

8. Lin, S.; Fleming, J.; Hetherington, D.; Smith, B.; Biswas, R.; Ho, K.; Sigalas, M.; Zubrzycki, W.; Kurtz, S.; Bur, J., A Three-Dimensional Photonic Crystal Operating at Infrared Wavelengths. *Nature* **1998,** *394* (6690), 251-253.

9. Painter, O.; Lee, R. K.; Scherer, A.; Yariv, A.; O'Brien, J. D.; Dapkus, P. D.; Kim, I., Two-Dimensional Photonic Band-Gap Defect Mode Laser. *Science* **1999,** *284* (5421), 1819-1821.

10. Noda, S.; Tomoda, K.; Yamamoto, N.; Chutinan, A., Full Three-Dimensional Photonic Bandgap Crystals at Near-Infrared Wavelengths. *Science* **2000,** *289* (5479), 604-606.

11. Y. A. Vlasov, X. Z. B., J. C. Sturm, D. J. Norris, On-Chip Natural Assembly of Silicon Photonic Bandgap Crystals. *Nature* **2001,** *414*, 289-293.

12. Im, S. H.; Kim, M. H.; Park, O. O., Thickness Control of Colloidal Crystals with a Substrate Dipped at a Tilted Angle into a Colloidal Suspension. *Chem. Mater.* **2003,** *15* (9), 1797-1802.

13. Maldovan, M.; Thomas, E. L.; Carter, C. W., Layer-By-Layer Diamond-Like Woodpile Structure with a Large Photonic Band Gap. *Appl. Phys. Lett.* **2004,** *84* (3), 362-364.

14. Mizeikis, V.; Seet, K. K.; Juodkazis, S.; Misawa, H., Three-Dimensional Woodpile Photonic Crystal Templates for the Infrared Spectral Range. *Opt. Lett.* **2004,** *29* (17), 2061-2063.

15. Gratson, G. M.; García-Santamaría, F.; Lousse, V.; Xu, M.; Fan, S.; Lewis, J. A.; Braun, P. V., Direct-Write Assembly of Three-Dimensional Photonic Crystals: Conversion of Polymer Scaffolds to Silicon Hollow-Woodpile Structures. *Adv. Mater.* **2006,** *18* (4), 461-465.

16. Lewis, J. A., Direct Ink Writing of 3D Functional Materials. *Adv. Funct. Mater.* **2006,** *16* (17), 2193-2204.

17. García-Santamaría, F.; Xu, M.; Lousse, V.; Fan, S.; Braun, P. V.; Lewis, J. A., A Germanium Inverse Woodpile Structure with a Large Photonic Band Gap. *Adv. Mater.* **2007,** *19*, 1567–1570.

18. Ding, T.; Song, K.; Clays, K.; Tung, C.-H., Bottom-Up Photonic Crystal Approach with Top-Down Defect and Heterostructure Fine-Tuning. *Langmuir* **2009,** *26* (6), 4535-4539.

19. Galusha, J. W.; Jorgensen, M. R.; Richey, L. R.; Gardner, J. S.; Bartl, M. H. In *Oxide-Based Photonic Crystals from Biological Templates*, SPIE 74010, Raul, J. M.-P.; Akhlesh, L., Eds. SPIE: 2009; p 74010G.

20. Wijnhoven, J.; Vos, W. L., Preparation of Photonic Crystals Made of Air Spheres in Titania. *Science* **1998,** *281* (5378), 802-804.

21. Lodahl, P.; Floris van Driel, A.; Nikolaev, I. S.; Irman, A.; Overgaag, K.; Vanmaekelbergh, D.; Vos, W. L., Controlling the Dynamics of Spontaneous Emission from Quantum Dots by Photonic Crystals. *Nature* **2004,** *430* (7000), 654-657.

22. Driel, A. F. v.; Nikolaev, I. S.; Vergeer, P.; Lodahl, P.; Vanmaekelbergh, D.; Vos, W. L., Statistical Analysis of Time-Resolved Emission from Ensembles of Semiconductor Quantum Dots: Interpretation of Exponential Decay Models. *Phys. Rev. B* **2007,** *75* (3), 035329.

23. Nikolaev, I. S.; Lodahl, P.; Floris van Driel, A.; Femius Koenderink, A.; Vos, W. L., Strongly Nonexponential Time-Resolved Fluorescence of Quantum-Dot Ensembles in Three-Dimensional Photonic Crystals. *Phys. Rev. B* **2007,** *75* (11), 115302.

24. Vos, W. L.; Koenderink, A. F.; Nikolaev, I. S., Orientation-Dependent Spontaneous Emission Rates of a Two-Level Quantum Emitter in any Nanophotonic Environment. *Phys. Rev. A* **2009,** *80* (5), 053802.

25. Qi, M. H.; Lidorikis, E.; Rakich, P. T.; Johnson, S. G.; Joannopoulos, J. D.; Ippen, E. P.; Smith, H. I., A Three-Dimensional Optical Photonic Crystal with Designed Point Defects. *Nature* **2004,** *429* (6991), 538-542.

26. Blanco, A.; Chomski, E.; Grabtchak, S.; Ibisate, M.; John, S.; Leonard, S. W.; Lopez, C.; Meseguer, F.; Miguez, H.; Mondia, J. P.; Ozin, G. A.; Toader, O.; van Driel, H. M., Large-Scale Synthesis of a Silicon Photonic Crystal with a Complete Three-Dimensional Bandgap near 1.5 Micrometres. *Nature* **2000,** *405* (6785), 437-440.

27. Wong, S.; Deubel, M.; Perez-Willard, F.; John, S.; Ozin, G. A.; Wegener, M.; von Freymann, G., Direct Laser Writing of Three-Dimensional Photonic Crystals with Complete a Photonic Bandgap in Chalcogenide Glasses. *Adv. Mater.* **2006,** *18* (3), 265-+.

28. Joannopoulos, J. D., *Photonic Crystals: Molding the Flow of Light*. Princeton Univ Pr: 2008.

29. Schroden, R. C.; Al-Daous, M.; Blanford, C. F.; Stein, A., Optical Properties of Inverse Opal Photonic Crystals. *Chem. Mater.* **2002,** *14* (8), 3305-3315.

30. Chen, Y. C.; Geddes, J. B.; Iii; Lee, J. T.; Braun, P. V.; Wiltzius, P., Holographically Fabricated Photonic Crystals with Large Reflectance. *Appl. Phys. Lett.* **2007,** *91* (24), 241103-3.

31. Thijssen, M. S.; Sprik, R.; Wijnhoven, J. E. G. J.; Megens, M.; Narayanan, T.; Lagendijk, A.; Vos, W. L., Inhibited Light Propagation and Broadband Reflection in Photonic Air-Sphere Crystals. *Phys. Rev. Lett.* **1999,** *83* (14), 2730-2733.

32. Johnson, S.; Joannopoulos, J., Block-Iterative Frequency-Domain Methods for Maxwell's Equations in a Planewave Basis. *Opt. Express* **2001,** *8* (3), 173-190.

33. Aguirre, C. I.; Reguera, E.; Stein, A., Tunable Colors in Opals and Inverse Opal Photonic Crystals. *Adv. Funct. Mater.* **2010,** *20* (16), 2565-2578.

34. Norris, D. J.; Arlinghaus, E. G.; Meng, L.; Heiny, R.; Scriven, L. E., Opaline Photonic Crystals: How Does Self-Assembly Work? *Adv. Mater.* **2004,** *16*, 1393-1399.

35. Lopez, C., Materials Aspects of Photonic Crystals. *Adv. Mater.* **2003,** *15* (20), 1679-1704.

36. Aparicio, F. J.; Lozano, G.; Blaszczyk-Lezak, I.; Barranco, A. n.; Míguez, H. n., Conformal Growth of Organic Luminescent Planar Defects within Artificial Opals. *Chem. Mater.* **2009,** *22* (2), 379-385.

CHAPTER 4

CALCULATION AND INTERPRETATION OF DENSITY OF OPTICAL STATES IN PHOTONIC CRYSTALS

Introduction

Control over excited state dynamics is of paramount importance for the next generation of photonic technologies such as solar cells, microlasers, and optical information processing.[1-4] Due to the potential impact of these technologies, focus on materials capable of controlling spontaneous emission has steadily increased. The discussion so far of biotemplated photonic crystals in this thesis was focused on the discovery, creation, and structural characterization of these materials. In this chapter, calculation will be presented of how the nonclassical properties of photonic crystals can affect the overall optical density of states and thus the excited state dynamics of light sources placed inside of them.

The concept that periodically organized dielectric materials could be capable of altering the density of optical states was first introduced in the early 1980s by Yablanovich and John.[5-6] Fermi's Golden Rule states that the rate of spontaneous emission is proportional to the density of optical states experienced by the emitter,[7] and therefore, elegantly bridges the connection between photonic crystals and control of spontaneous emission. The density of optical states is essentially a count of the optical

modes available to an emitter at a particular frequency, so structures that have several overlapping photonic stop gaps also have frequency ranges with strongly modified density of optical states.[8] In the most ideal case, a structure would have overlapping photonic stop gaps in all directions (a complete or full photonic band gap), resulting in a range of frequencies where the density of optical states drops to zero in the band gap while being greatly enhanced at the band edge. Both the crystal lattice and the geometry of the objects at the lattice points impact the photonic band structure of a photonic crystal. One system in particular, a diamond lattice connected by dielectric rods, has been proven to be the best at altering the density of optical states over the broadest range of refractive index and filling fraction.[9] Several other photonic crystal designs that are based on the dielectric rod diamond structure, but are more synthetically amenable, have also been theoretically investigated and have been shown to be almost as effective as the original champion diamond structure.[10]

Due to the recent discovery of naturally occurring photonic crystals with diamond based lattices[11-12] and their conversion into high refractive index materials,[13-15] to the author's knowledge this is the first work investigating the density of optical states in structured materials derived from nature. The uniqueness of these new materials has led to interesting theoretical results regarding the relationship between structures, photonic band structure diagrams, and their density of optical states. Based on our recent structural analysis of the naturally occurring diamond based structure in *Lamprocyphus augustus* scales,[11] we have calculated the corresponding density of optical states along with several other structures derivable from it. We have found that diamond based photonic crystals need not possess a full photonic band gap to show strong alteration of

the density of optical states—a finding of enormous importance regarding application of photonic crystals. This will be further discussed in Chapter five, along with a description of experimental measurements of modified spontaneous emission, an direct consequence of a modified density of optical states.

Density of Optical States Theory

It has long been realized since E. M. Purcell's first report[16] of modified spontaneous emission in 1942 that the irradiative dynamics of emitters are connected to the optical mode structure surrounding the emitter. An emitter will only decay from an excited state by emitting a photon if there is an optical state for the photon to couple to, having a frequency so that energy is conserved. Therefore, it may be expected that the rate of spontaneous emission is proportional to the density of optical modes available at the appropriate frequency to an emitter, in accordance with Fermi's Golden Rule[7], equation 4.1.

$$\Gamma_{rad} = \frac{2\pi}{\hbar^2}\left|M_{if}\right|^2 \rho_{rad} \tag{4.1}$$

In equation 4.1 Γ_{rad} is the rate of spontaneous emission, $\left|M_{if}\right|$ is the transition dipole moment of the emitter between an initial (*i*) and a final (*f*) state, and ρ_{rad} is the sum of all the local density of optical states available to emitters over the unit cell. The details of local density of optical states have been discussed in detail elsewhere.[17] In cases where the system of interest involves ensembles of emitters located randomly throughout a photonic crystal, as is the case here, the total density of states corresponds to the

ensemble average rate of spontaneous emission.[18-22] The density of optical states is given by equation 4.2, where *N(ω)* is the frequency dependent density of optical states (the ***k***-space volume yielding a particular frequency; with ***k*** being the wave vector) obtained by integrating ***k*** over the first Brillouin zone (B.Z.) and summing over *n* photonic bands, counting only ***k*** that yield the frequency of interest (using the Kronecker delta).

$$N(\omega) = \sum_n \int_{B.Z.} d^3\boldsymbol{k}\, \delta\big(\omega - \omega_n(\boldsymbol{k})\big) \tag{4.2}$$

In this thesis, density of optical states calculations were based on the method outlined by Busch and John,[8] using a combination of MIT photonic bands package (MPB) and house-written software. The density of optical states plot resulting from equation 4.2 provides important information regarding photonic crystal properties that are not included in photonic band diagrams. This is because the density of optical states includes information about the entire Brillouin zone, while photonic band diagrams contain information only from certain high-symmetry lines and points. While photonic band diagrams and density of optical states plots do mirror each other, we have found that certain crystal directions contribute to the density of optical states with differing weights, a finding important to photonic crystal design because it shows that achieving band gaps in some directions is more important than others.

Calculation of Density of Optical States

Solving of equation 4.2 is executed numerically in the same general manner for one-, two-, and three-dimensional photonic crystal examples by breaking the first

Brillouin zone into an array of ***k***-points, so that each ***k***-point corresponds to an equally sized piece of the Brillouin zone. When divided this way, a count of the number of ***k***-points yielding a frequency between ω and $\omega+\Delta\omega$ is proportional to $N(\omega)$.

For the three-dimensional cases discussed in this thesis, a grid of up to 269,001 equally spaced ***k***-points spanning the first Brillouin zone was calculated using house-made software written in c++. This was done by dividing the irreducible Brillouin zone into three pyramids with bases corresponding to the three faces of the zone, the apex of each being the origin. Each pyramid was then divided into an array of equally sized volumes. This was done by dividing each edge of the pyramids into an integral number of segments, which then become the primitive lattice vectors for the points filling each sub-space of the Brillouin zone. The points inside each pyramid were populated by iterating the lattice vectors over the entire pyramid volume as shown in Figure 4.1, which has a reduced number of points for clarity (see c++ source code in Appendix for details on calculation of array). Care was taken to avoid duplicate points, and each point included was weighted to account for the relative volume between the different sections of the Brillouin zone. The points along lines of high symmetry were weighted to account for their overall contribution to the volume of the Brillouin zone.

Using the list of 269,001 ***k***-points generated as input, MPB was used to calculate the frequencies at each ***k***-point for bands that yield a frequency result in between zero and one (in units of $c/2\pi a$). Typically, each calculation involved up to sixteen photonic bands resulting in 16×269,001 frequency computations that were each numerically solved. Calculations were performed in parallel at University of Utah's Center for High Performance Computing, an average run requiring 128 2.4 GHz processors about 24

hours. Finally, the density of optical states was calculated by sorting the frequencies into about 200 bins spanning the reduced frequency range from zero to one.

Results and Discussion

Figure 4.2 shows a comparison of the calculated density of optical states for a relatively simple structure, a two-dimensional lattice of air cylinders etched into silicon. The results of our calculations (using a Brillouin zone divided into 3321 equal parts) are shown to be in agreement with previous work published in the literature.[8] In this particular example, a very large photonic band gap is present in the structure resulting in a broad range of frequencies for which the density of optical states drops to zero.

Figure 4.3 shows the density of optical states for a face centered cubic lattice of air spheres (inverse opal), comparing the situations where the refractive index contrast is very low (0.1) and high (2.4). In the case of low refractive index contrast, the density of optical states exhibits quadratic behavior as expected (because the number of optical modes that can fit in an arbitrary volume is inversely proportional to the wavelength squared). The high refractive index contrast example, air spheres surrounded by silicon, shows modest modification of the density of optical states at low frequencies then drops to zero at a frequency of 0.8 $c/(2\pi a)$ corresponding to a full photonic band gap between the 8^{th} and 9^{th} bands. Calculation of the high-contrast inverse opal was executed on an office PC prior to access to the University of Utah's Center for High Performance Computing, so was calculated with a reduced number of $\boldsymbol{k}$-points (4,851 compared to 269,001) resulting in a rougher appearance.

Our previous work has shown that the structure contained within the scales of *L. augustus* and other similar weevils is a diamond-based lattice of air cylinders.[11] Photonic band calculations using spatial parameters collected from focused ion beam (FIB) and SEM studies have shown that while these chitin structures do not possess a full photonic band gap, they do have multiple overlapping stop gaps that correspond to the scale's reflections.[11] The calculated density of optical states for the photonic crystal structure contained in *L. augustus* scales is given in Figure 4.4 and shows that the density of optical states is dramatically reduced over two reduced frequency ranges dropping by 20% at 0.7 and 40% at 0.8 corresponding to the *Γ-L* gaps and overlapping *Γ-U*, *Γ-W*, and *Γ-K* directions, respectively. Such a large modification of density of optical states is surprising for a structure made from the biopolymer chitin—a material with a relatively low refractive index of 1.54.[23] Interestingly, the *Γ-L* stop gap reduces the overall density of optical states by 20% while the three overlapping *Γ-U*, *Γ-W*, and *Γ-K* directions reduce it by only 36%, a finding that applies directly to photonic crystal design.

Motivated by the strong effect chitin scales have on density of optical states, we have theoretically investigated all the replica structures that are accessible to us by sol-gel chemistry methods (as described in Chapter 2), including silica inverse, silica positive shell, titania inverse, titania positive shell, and titania replica structures. For each of these structures photonic band diagrams and density of optical states were calculated to assess their potential usefulness. As shown in Figure 4.5, we found that structures based on the diamond-based lattice are capable of dramatically altering the density of optical states, even in the absence of a complete photonic band gap. Silica shell and silica inverse structures modify the density of optical states at a magnitude similar to the original chitin

template, but have the distinct advantages of being nonfluorescent, mechanically stable, and photo-stable. The titania shell structures offer a degree of control over the magnitude of density of optical states inhibition through the shell thickness. Titania inverse structures show strong modification of density of optical states, reducing it by ± 80%. Titania replicas of the original chitin scale, produced using a two-step templating procedure,[13] show the greatest effect on density of optical states reducing it more than 80% over a broad range, even narrowly dropping to zero, as shown in Figure 4.6. Density of optical states calculations provided strong motivation for exploring the effect that titania replica photonic crystals have on the spontaneous emission. In contrast to the band structure diagram for the titania replica, which would predict inhibition of spontaneous emission over only a very small frequency range, the density of optical states show a broadband effect more amiable to experimental measurement.

Conclusion

We have introduced the density of optical states as a useful computational tool to understand the effect of photonic crystals on integrated light sources. The density of optical states has been calculated for several simple systems, including two dimensional lattices and inverse opals, to validate the computational method used. By using house-written software in conjunction with MPB software, the density of optical states for several biologically derived structures has been calculated. We have highlighted the potential of these structures by showing their ability to alter the density of optical states within them. It was found that the diamond lattice produces strong modification of the density of optical states, even when the refractive index contrast is relatively low. At

refractive index contrasts provided by titania, modest in comparison to materials available in the infrared, broadband reduction and even complete inhibition of optical states is possible providing motivation for additional experiments. These experiments will be addressed in the following chapter.

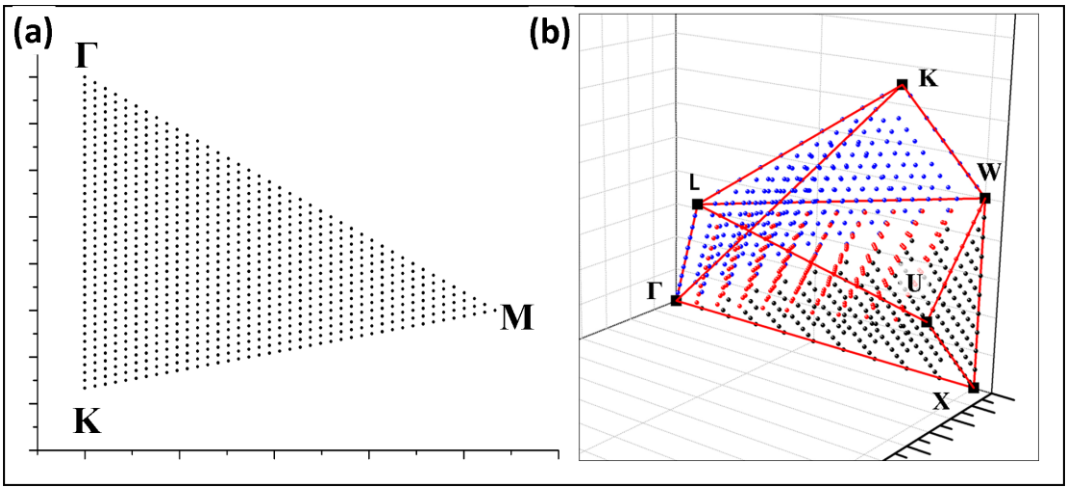

Figure 4.1 Plot of the 1st irreducible Brillouin zones of a two-dimensional lattice (a), and three-dimensional face centered cubic lattice (b). To produce the array of points shown in (b), the Brillouin zone was divided up into three pyramids having bases XUW, LUW, and LKW, with Γ being the apex of each.

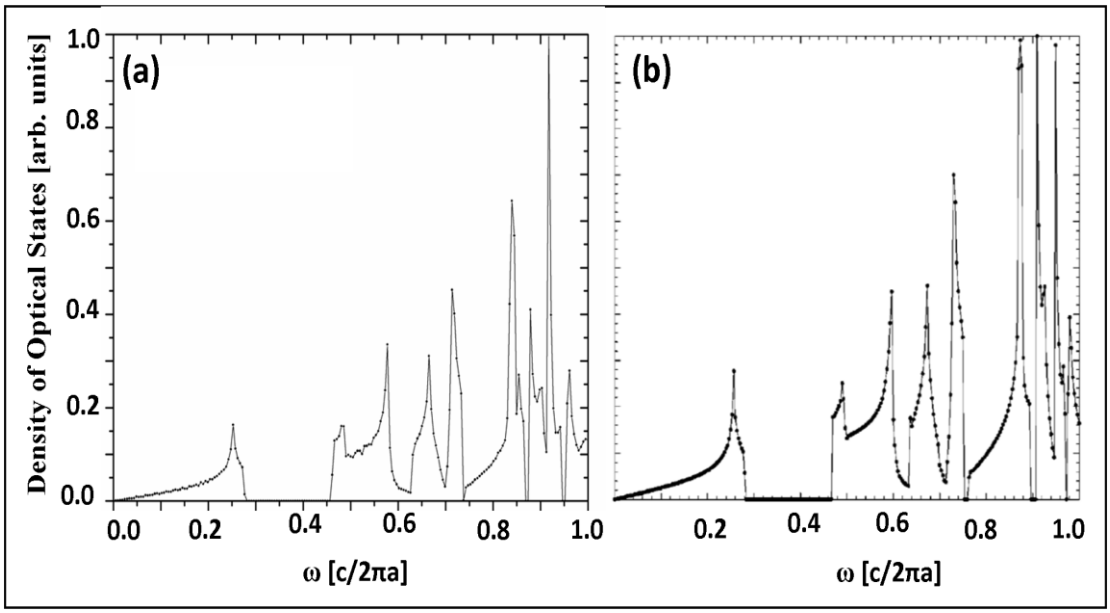

Figure 4.2 A comparison of calculated density of optical states for a triangular lattice of air cylinders etched into silicon, with a solid filling fraction of 33%. (a) Calculated density of states using a combination of MPB and house-written software, based on a two dimensional irreducible Brillouin zone divided into 3321 k-points. (b) Calculated density of states for the same structure, calculated using a similar method, reproduced with permission from reference 8, copyright 1998 The American Physical Society.

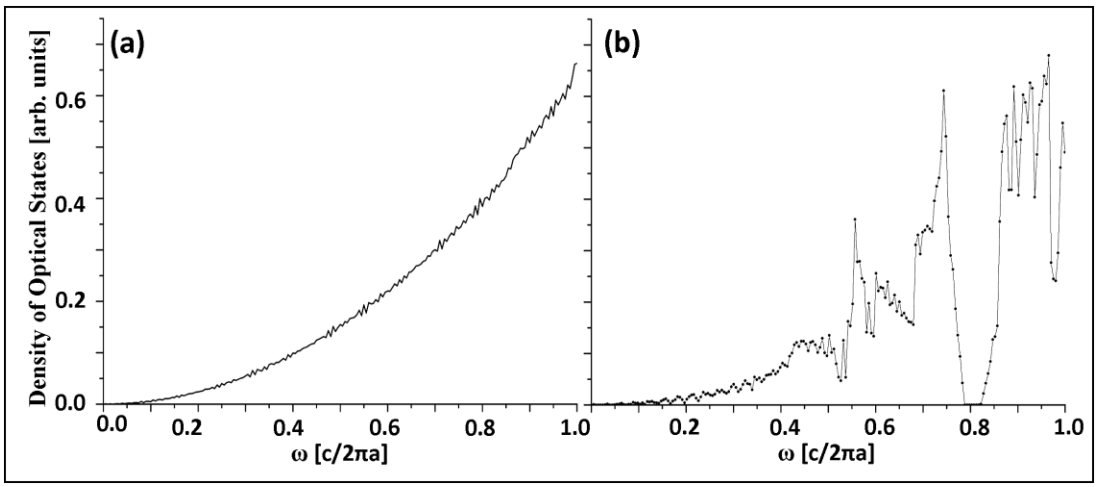

Figure 4.3 Density of optical states for two inverse opals, one with low refractive index contrast (a) and one with high refractive index contrast (b). a) A face centered cubic lattice of air spheres (refractive index of 1) surrounded by a matrix with refractive index of 1.1. b) An inverse opal identical to the one yielding (a), except the surrounding refractive index is 3.4. The drop to zero density of optical states in (b) corresponds to a full photonic band gap between the 8^{th} and 9^{th} photonic bands.

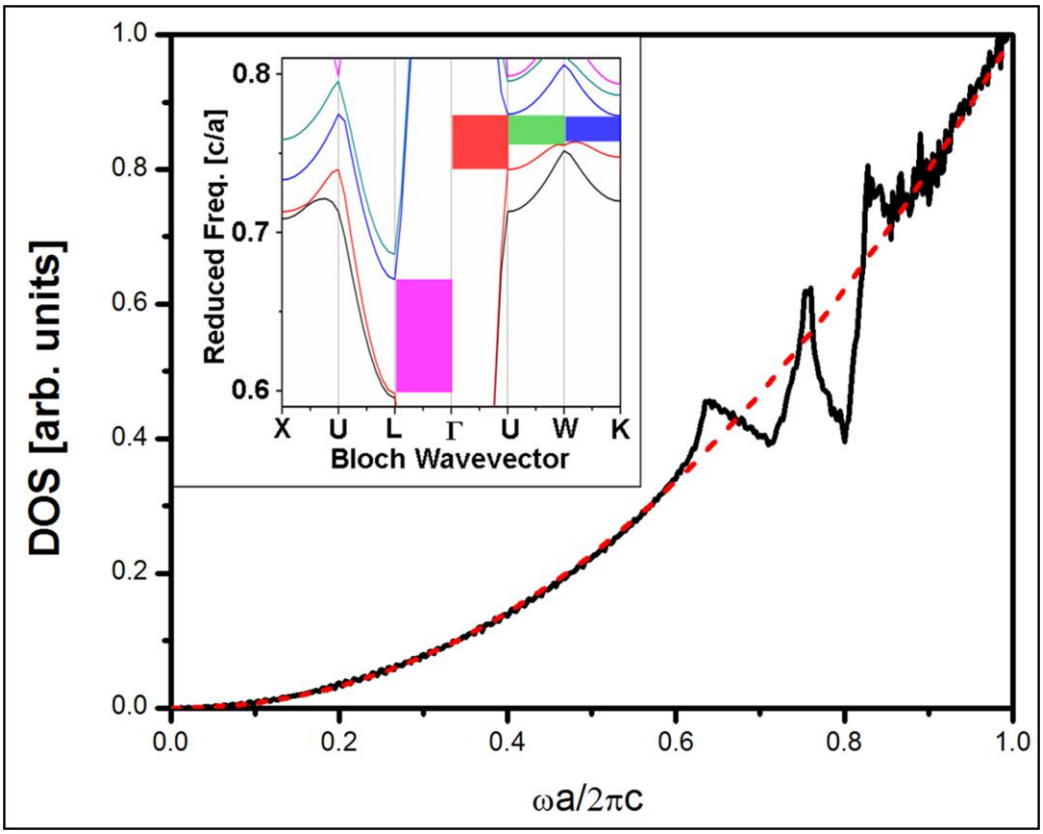

Figure 4.4 Calculated density of optical states and band diagram (inset) for an FCC lattice of air cylinders surrounded by a biopolymer matrix, the diamond-based structure found within the scales of *L. Augustus*. The red dashed line is a quadratic fit to the curve meant to reflect the density of optical states in a homogeneous medium having the same effective refractive index.

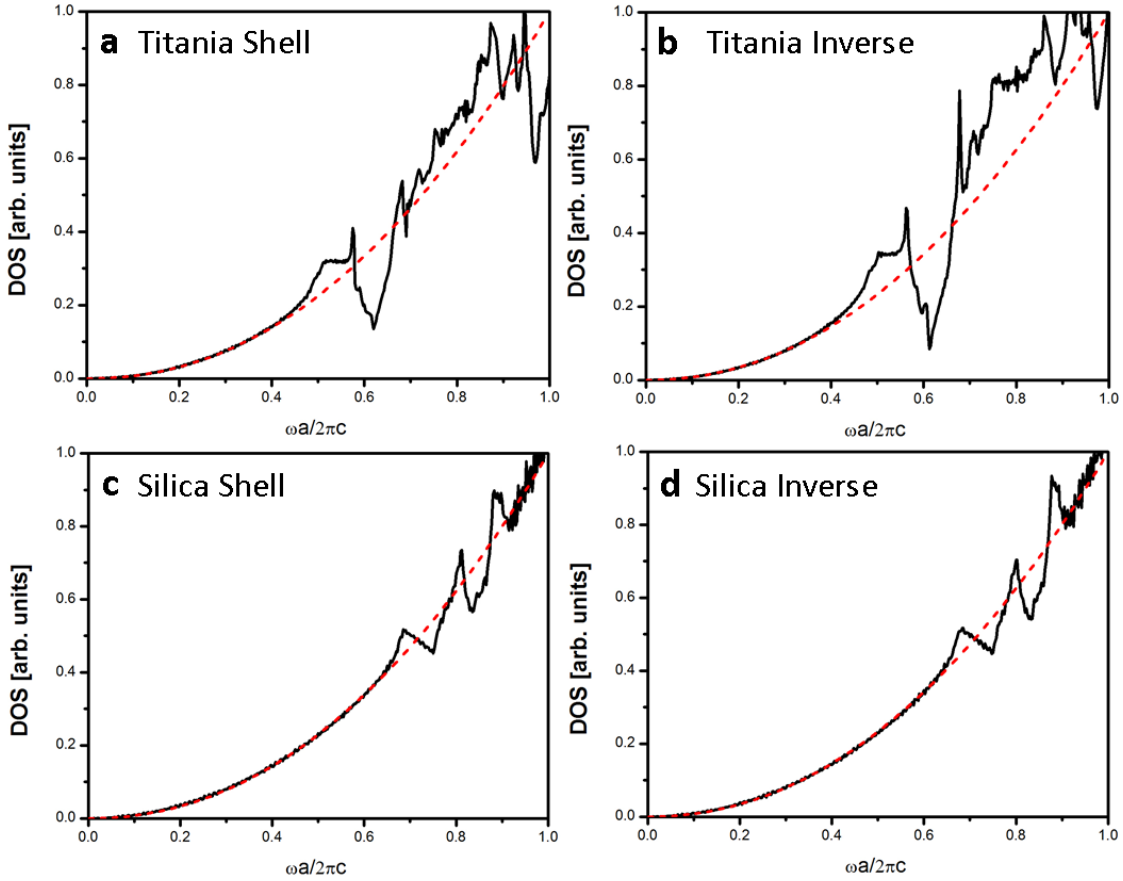

Figure 4.5 Calculated DOS for several structures possible using a diamond-based chitin structure as a template. See Figure 2.4 for examples of corresponding SEM and reflection measurements. For comparison purposes each calculation is based on the same structural parameters, which is an FCC lattice of air cylinders oriented in the [1,1,1] direction (diamond-based) with a radius of 0.22a and height of 0.81a. a) DOS from titania shell structure showing a 65% reduction in DOS at a red. freq. of 0.62. b) DOS from titania inverse structure showing a 80% reduction in DOS at a red. freq. of 0.61. c) DOS from silica shell structure showing a 20% reduction of DOS at red. freqs. 0.75 and 0.85. d) DOS from silica inverse structure showing a 22% reduction of DOS at red. freqs. of 0.74 and 0.84.

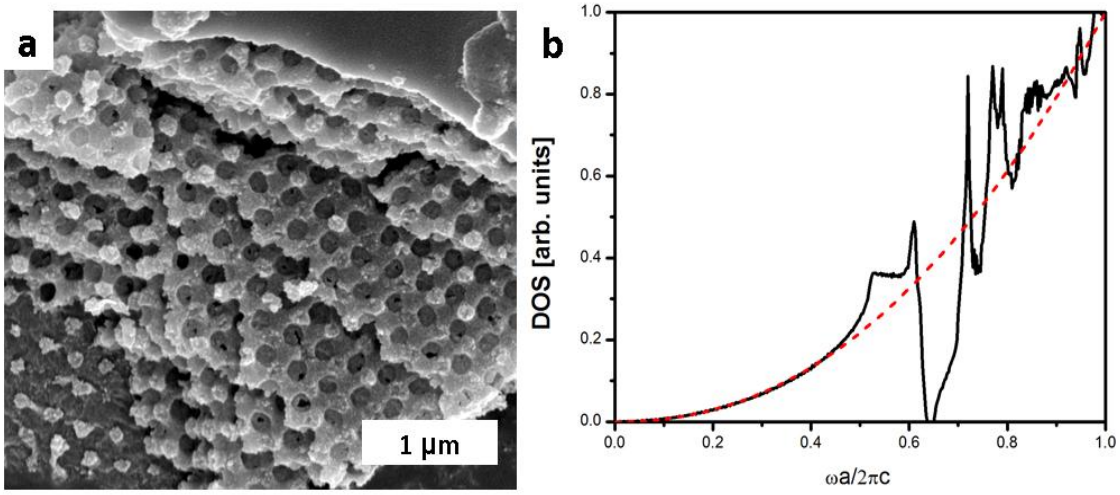

Figure 4.6 Example of a titania photonic crystal and its accompanying calculated DOS. a) SEM image of a titania replica of Lamprocyphus Augustus exoskeletal scale. b) Calculated DOS (solid line) from structure shown in (a) showing strong deviation from homogeneous space behavior, including a frequency range where optical states are completely inhibited.

Appendix Code in C++ to Break FCC Brillouin Zone into Discrete Points

In C++, text after // and between /* and */ is ignored, allowing for comments on the code and for certain sections to be commented out. This code was compiled using g++ in Ubuntu. The code outputs the list of kpoints to the screen, which can then be redirected to a file using >& in Linux or >> in windows terminal.

The Brillouin zone is broken up into pieces: lines, planes, and solids. Each piece is labeled by the points at its vertex: Gamma (G), X, U, W, and K. Each line is broken up into D number of pieces.

```
#include<iostream>
#include<fstream>
#include<stdlib.h>
using namespace std;

int main(int argc, char *argv[]){
//The Reciprocal Space Basis Vecotrs
        double *b1, *b2, *b3;
        b1 = new double[3], b2 = new double[3], b3 = new double[3];
        int D=atoi(argv[1]); int kcount=0;

        b1[0] = -1, b1[1] = 1, b1[2] =1; b2[0] = 1, b2[1] = -1, b2[2] =1;
        b3[0] = 1, b3[1] = 1, b3[2] =-1;
/*
        cout << "\nb1 = (" << b1[0] << ", " << b1[1] << ", " << b1[2] << ")\n";
        cout << "b2 = (" << b2[0] << ", " << b2[1] << ", " << b2[2] << ")\n";
        cout << "b3 = (" << b3[0] << ", " << b3[1] << ", " << b3[2] << ")\n\n";
*/
//Key directions in the FCC Brillouin zone
        double *X, *U, *W, *K, *L, *G;
        X = new double[3], U = new double[3], W = new double[3];
        K = new double[3], L = new double[3], G = new double[3];

//Definition of key directions in the reciprocal basis
        G[0] = 0.000, G[1] = 0.000, G[2] = 0.000;
        U[0] = 0.000, U[1] = 0.625, U[2] = 0.375;
        W[0] = 0.250, W[1] = 0.750, W[2] = 0.500;
        K[0] = 0.375, K[1] = 0.750, K[2] = 0.375;
        L[0] = 0.000, L[1] = 0.500, L[2] = 0.000;
        X[0] = 0.000, X[1] = 0.500, X[2] = 0.500;

//Checking input of key directions/*
cout << "G(basis) = (" << G[0] << ", " << G[1] << ", " << G[2] << ")\n";
cout << "X(basis) = (" << X[0] << ", " << X[1] << ", " << X[2] << ")\n";
cout << "U(basis) = (" << U[0] << ", " << U[1] << ", " << U[2] << ")\n";
cout << "W(basis) = (" << W[0] << ", " << W[1] << ", " << W[2] << ")\n";
cout << "K(basis) = (" << K[0] << ", " << K[1] << ", " << K[2] << ")\n";
cout << "L(basis) = (" << L[0] << ", " << L[1] << ", " << L[2] << ")\n\n";
*/
//Key directions in cartesian coordinates
        double *Xc, *Uc, *Wc, *Kc, *Lc;
        Xc = new double[3], Uc = new double[3], Wc = new double[3];
        Kc = new double[3], Lc = new double[3];

//Converting from reciprocal lattice basis to cartesian
        for(int i =0; i < 3; i++){
        Xc[i] = X[0]*b1[i]+X[1]*b2[i]+X[2]*b3[i];
        Lc[i] = L[0]*b1[i]+L[1]*b2[i]+L[2]*b3[i];
        Kc[i] = K[0]*b1[i]+K[1]*b2[i]+K[2]*b3[i];
        Wc[i] = W[0]*b1[i]+W[1]*b2[i]+W[2]*b3[i];
        Uc[i] = U[0]*b1[i]+U[1]*b2[i]+U[2]*b3[i];
```

```
}
/*
cout << "X(cart.) = (" << Xc[0] << ", " << Xc[1] << ", " << Xc[2] << ")\n";
cout << "U(cart.) = (" << Uc[0] << ", " << Uc[1] << ", " << Uc[2] << ")\n";
cout << "W(cart.) = (" << Wc[0] << ", " << Wc[1] << ", " << Wc[2] << ")\n";
cout << "K(cart.) = (" << Kc[0] << ", " << Kc[1] << ", " << Kc[2] << ")\n";
cout << "L(cart.) = (" << Lc[0] << ", " << Lc[1] << ", " << Lc[2] << ")\n";
*/
        double *dXc = new double[3];  double *dLc = new double[3];
        double *dKc = new double[3];  double *dWc = new double[3];
        double *dUc = new double[3];

  for(int i = 0; i < 3; i++){
        dXc[i] = Xc[i]/D;
        dLc[i] = Lc[i]/D;
        dKc[i] = Kc[i]/D;
        dWc[i] = Wc[i]/D;
        dUc[i] = Uc[i]/D;
}

//Points along line GL, excluding origin
  for(int i = 1; i <= D; i++){ kcount++;
    cout << "Weight: " << "0.166667 " << kcount << " " << "GL " << i*dLc[0] << " " <<
i*dLc[1] << " " << i*dLc[2] << "\n";
  }
//Points along line GX, excluding origin
  for(int i = 1; i <= D; i++){ kcount++;
    cout << "Weight: " << "0.25 " << kcount << " " << "GX " << i*dXc[0] << " " <<
i*dXc[1] << " " << i*dXc[2] << "\n";
  }
//Points along line GK, excluding origin
  for(int i = 1; i <= D; i++){ kcount++;
    cout << "Weight: " << "0.25 " << kcount << " " << "GK " << i*dKc[0] << " " <<
i*dKc[1] << " " << i*dKc[2] << "\n";
}
//points along line GU, including the origin
  for(int i = 0; i <= D; i++){ kcount++;
    cout << "Weight: " << "0.5 " << kcount << " " << "GU " << i*dUc[0] << " " << i*dUc[1]
<< " " << i*dUc[2] << "\n";
  }
//Points along the line GW, excluding origin
for(int i = 1; i <= D; i++){ kcount++;
    cout << "Weight: " << "0.5 " << kcount << " " << "GW " << i*dWc[0] << " " << i*dWc[1]
<< " " << i*dWc[2] << "\n";
}
//Points in plane GXU, exlcuding origin and lines GU and GX
  for(int i = 2; i <= D; i++){
    for(int j = 1; j <= i-1; j++){ kcount++;
      cout << "Weight: " << "0.5 " << kcount << " " << "GXU " << (i-j)*dXc[0]+j*dUc[0] <<
" " << (i-j)*dXc[1]+j*dUc[1] << " " << (i-j)*dXc[2]+j*dUc[2] << "\n";
    }
  }
//Points in plane GXW, excluding origin and lines GX and GW
  for(int i = 2; i <= D; i++){
    for(int j = 1; j <= i-1; j++){ kcount++;
      cout << "Weight: " << "0.5 " << kcount << " " << "GXW " << (i-j)*dXc[0]+j*dWc[0] <<
" " << (i-j)*dXc[1]+j*dWc[1] << " " << (i-j)*dXc[2]+j*dWc[2] << "\n";
    }
  }
//Points in plane GLU, exlcuding origin and lines GL and GU
  for(int i = 2; i <= D; i++){
    for(int j = 1; j <= i-1; j++){ kcount++;
      cout << "Weight: " << "0.5 " << kcount << " " << "GLU " << (i-j)*dLc[0]+j*dUc[0] <<
" " << (i-j)*dLc[1]+j*dUc[1] << " " << (i-j)*dLc[2]+j*dUc[2] << "\n";
    }
  }
//Points in plane GKL, excluding origin and lines GW and GU
for(int i = 2; i <= D; i++){
    for(int j = 1; j <= i-1; j++){ kcount++;
```

```
      cout << "Weight: " << "0.5 " << kcount << " " << "GKL " << (i-j)*dKc[0]+j*dLc[0] <<
" " << (i-j)*dKc[1]+j*dLc[1] << " " << (i-j)*dKc[2]+j*dLc[2] << "\n";
    }
  }
//Points in plane GWK, excluding origin and lines GW and GU
for(int i = 2; i <= D; i++){
    for(int j = 1; j <= i-1; j++){ kcount++;
      cout << "Weight: " << "0.5 " << kcount << " " << "GWK " << (i-j)*dKc[0]+j*dWc[0] <<
" " << (i-j)*dKc[1]+j*dWc[1] << " " << (i-j)*dKc[2]+j*dWc[2] << "\n";
    }
  }
//Points in internal plane GWU, excluding origin and lines GW and GU
for(int i = 2; i <= D; i++){
    for(int j = 1; j <= i-1; j++){ kcount++;
      cout << "Weight: " << "1.0 " << kcount << " " << "GWU " << (i-j)*dUc[0]+j*dWc[0] <<
" " << (i-j)*dUc[1]+j*dWc[1] << " " << (i-j)*dUc[2]+j*dWc[2] << "\n";
    }
  }
//Points in internal plane GLW, exlcuding origin and lines GL and GW
  for(int i = 2; i <= D; i++){
    for(int j = 1; j <= i-1; j++){ kcount++;
      cout << "Weight: " << "1.0 " << kcount << " " << "GLW " << (i-j)*dLc[0]+j*dWc[0] <<
" " << (i-j)*dLc[1]+j*dWc[1] << " " << (i-j)*dLc[2]+j*dWc[2] << "\n";
    }
  }
//Points inside, excluding internal planes and lines
  for(int i = 1; i <= D; i++){
    for(int j = 2; j <= D-i; j++){
      for(int k = 1; k <= j-1; k++){ kcount++;
        cout << "Weight: " << "1.0 " << kcount << " " << "GXUW " << (j-
k)*dXc[0]+(k)*dWc[0]+i*dWc[0] << " " << (j-k)*dXc[1]+(k)*dUc[1]+i*dWc[1] << " " << (j-
k)*dXc[2]+(k)*dUc[2]+i*dWc[2] << "\n";
      }
    }
  }

//Points inside, excluding internal planes and lines
  for(int i = 1; i <= D; i++){
    for(int j = 2; j <= D-i; j++){
      for(int k = 1; k <= j-1; k++){ kcount++;
        cout << "Weight: " << "1.0 " << kcount << " " << "GLUW " << (j-
k)*dLc[0]+(k)*dUc[0]+i*dWc[0] << " " << (j-k)*dLc[1]+(k)*dUc[1]+i*dWc[1] << " " << (j-
k)*dLc[2]+(k)*dUc[2]+i*dWc[2] << "\n";
      }
    }
  }
//Points inside, excluding internal planes and lines
  for(int i = 1; i <= D; i++){
    for(int j = 2; j <= D-i; j++){
      for(int k = 1; k <= j-1; k++){ kcount++;
        cout << "Weight: " << "1.0 " << kcount << " " << "GLKW " << (j-
k)*dLc[0]+(k)*dKc[0]+i*dWc[0] << " " << (j-k)*dLc[1]+(k)*dKc[1]+i*dWc[1] << " " << (j-
k)*dLc[2]+(k)*dKc[2]+i*dWc[2] << "\n";
      }
    }
  }
}
```

References

1. Arpin, K. A.; Mihi, A.; Johnson, H. T.; Baca, A. J.; Rogers, J. A.; Lewis, J. A.; Braun, P. V., Multidimensional Architectures for Functional Optical Devices. *Adv. Mater.* **2010,** *22* (10), 1084–1101.

2. Woldeyohannes, M.; John, S., Coherent Control of Spontaneous Emission Near a Photonic Band Edge. *J. Opt. B* **2003,** (2), R43-R82.

3. Halaoui, L. I.; Abrams, N. M.; Mallouk, T. E., Increasing the Conversion Efficiency of Dye-Sensitized TiO2 Photoelectrochemical Cells by Coupling to Photonic Crystals. *J. Phys. Chem. B* **2005,** *109* (13), 6334-6342.

4. Chen, J. I. L.; von Freymann, G.; Choi, S. Y.; Kitaev, V.; Ozin, G. A., Amplified Photochemistry with Slow Photons. *Adv. Mater.* **2006,** *18* (14), 1915-1919.

5. Yablonovitch, E., Inhibited Spontaneous Emission in Solid-State Physics and Electronics. *Phys. Rev. Lett.* **1987,** *58* (20), 2059.

6. John, S., Strong Localization of Photons in Certain Disordered Dielectric Superlattices. *Phys. Rev. Lett.* **1987,** *58* (23), 2486.

7. Loudon, R., *The Quantum Theory of Light*. Oxford University press: New York, 2000.

8. Busch, K.; John, S., Photonic Band Gap Formation in Certain Self-Organizing Systems. *Phys. Rev. E* **1998,** *58* (3), 3896.

9. Maldovan, M.; Thomas, E. L., Diamond-Structured Photonic Crystals. *Nat. Mater.* **2004,** *3* (9), 593-600.

10. Maldovan, M.; Thomas, E. L.; Carter, C. W., Layer-By-Layer Diamond-Like Woodpile Structure with a Large Photonic Band Gap. *Appl. Phys. Lett.* **2004,** *84* (3), 362-364.

11. Galusha, J. W.; Richey, L. R.; Gardner, J. S.; Cha, J. N.; Bartl, M. H., Discovery of a Diamond-Based Photonic Crystal Structure in Beetle Scales. *Phys. Rev. E* **2008,** *77* (5), 050904(1-4).

12. Galusha, J. W.; Richey, L. R.; Jorgensen, M. R.; Gardner, J. S.; Bartl, M. H., Study of Natural Photonic Crystals in Beetle Scales and their Conversion into Inorganic Structures via a Sol-Gel Bio-templating Route. *J. Mater. Chem.* **2010,** *20* (7), 1277-1284.

13. Galusha, J. W.; Jorgensen, M. R.; Bartl, M. H., Diamond-Structured Titania Photonic-Bandgap Crystals from Biological Templates. *Adv. Mater.* **2010,** *22* (1), 107-110.

14. Jorgensen, M. R.; Bartl, M. H., Biotemplating Routes to Three-Dimensional Photonic Crystals. *J. Mater. Chem.* **2011,** *21* (29), 10583-10591.

15. Jorgensen, M. R.; Yonkee, B. P.; Bartl, M. H., Solid and Hollow Inorganic Replicas of Biological Photonic Crystals. *Scripta Mater.* **2011,** *65* (11), 954-957.

16. Purcell, E. M.; Torrey, H. C.; Pound, R. V., Resonance Absorption by Nuclear Magnetic Moments in a Solid. *Phys. Rev.* **1946,** *69* (1-2), 37.

17. Nikolaev, I. S.; Vos, W. L.; Koenderink, A. F., Accurate Calculation of the Local Density of Optical States in Inverse-Opal Photonic Crystals. *J. Opt. Soc. Am. B* **2009,** *26* (5), 987-997.

18. Kleppner, D., Inhibited Spontaneous Emission. *Phys. Rev. Lett.* **1981,** *47* (4), 233.

19. Koenderink, A. F.; Bechger, L.; Lagendijk, A.; Vos, W. L., An Experimental Study of Strongly Modified Emission in Inverse Opal Photonic Crystals. *Phys. Status Solidi* **2003,** *197* (3), 648-661.

20. Lodahl, P.; Floris van Driel, A.; Nikolaev, I. S.; Irman, A.; Overgaag, K.; Vanmaekelbergh, D.; Vos, W. L., Controlling the Dynamics of Spontaneous Emission from Quantum Dots by Photonic Crystals. *Nature* **2004,** *430* (7000), 654-657.

21. Nikolaev, I. S.; Lodahl, P.; Vos, W. L., Quantitative Analysis of Directional Spontaneous Emission Spectra from Light Sources in Photonic Crystals. *Phys. Rev. A* **2005,** *71* (5), -.

22. Vos, W. L.; Koenderink, A. F.; Nikolaev, I. S., Orientation-Dependent Spontaneous Emission Rates of a Two-Level Quantum Emitter in any Nanophotonic Environment. *Phys. Rev. A* **2009,** *80* (5), 053802.

23. Biró, L. P.; Kertész, K.; Vértesy, Z.; Márk, G. I.; Bálint, Z.; Lousse, V.; Vigneron, J. P., Living Photonic Crystals: Butterfly Scales -- Nanostructure and Optical Properties. *Mat. Sci. Eng. C* **2007,** *27* (5-8), 941-946.

CHAPTER 5

STRONGLY MODIFIED SPONTANEOUS EMISSION RATES IN DIAMOND-STRUCTURED PHOTONIC CRYSTALS

Introduction

The dynamics of radiative transitions is directly proportional to the density of optical states, according to Fermi's golden rule.[1] Given the pivotal role of radiative processes in solar energy conversion, solid-state lighting and lasing, along with quantum information processing, strategies to manipulate the radiative density of optical states over broad frequency ranges are of paramount technological importance. A central tenet in quantum electrodynamics is that the density of optical states and thus the dynamics of spontaneous emission can be manipulated in the presence of specifically engineered environments.[1-7] Prime examples of such environments are three-dimensional (3D) periodically ordered crystal structures with lattice parameters comparable to the photon wavelength of interest. Because of this periodic variation of the refractive index, these materials, termed photonic crystals, possess direction-dependent energy dispersion of photonic states (band structures) with directional photonic stop gaps and, under certain circumstances, overlap of all directional photonic stop gaps into a complete band gap.[8-15] The band structure properties of these materials cause significant modifications in the density of optical states distribution,[16] and importantly, compared to other density of

optical states-modifying media such as optical microcavities,[6-7] modifications occur over large bandwidths ($\Delta\omega/\omega$ of up to tens of percent) and are a bulk effect and thus not limited to small cavity volumes.

While such broadband modification of spontaneous emission has been demonstrated at infrared wavelengths in 2D[17] and 3D[14-15] photonic crystals, experimental studies at visible frequencies have been limited by the difficulty of fabricating photonic crystal structures that strongly modify the density of optical states distribution. Photonic crystals mainly used at visible frequencies are so-called inverse opals.[18-21] While inverse-opal photonic crystals operating at visible frequencies have a 3D periodic lattice, unfortunately, they possess only nonoverlapping single-directional photonic stop gaps and therefore cause only modest density of optical states modification.[22-23] Photonic crystal structures with much stronger impact on the photonic density of optical states distribution would be those with diamond-based lattices.[24-26] In these lattices overlap of multiple photonic stop gaps occurs in the low-frequency range (between the second and third optical band) for dielectric lattices with even only modest refractive indices.[26] However, in contrast to infrared photonic crystals, difficulties of fabricating diamond-based photonic crystals with lattice constants at visible wavelengths have kept them out of reach—until recently, when the Bartl group discovered that the striking coloration of various weevils is the result of light reflecting from biopolymeric chitin photonic crystals with a diamond-based lattice structure.[27-28] Moreover, these biopolymeric structures can be used as molds for creating high-dielectric replicas, including the first photonic crystal with structural and dielectric properties for which calculations revealed a complete band gap in the visible.[29]

In this chapter, the experimental aspects of studying excited state dynamics of photon sources placed inside photonic crystals will be discussed. First, a few of the different models used to understand the radiative lifetime of emitters will be examined. Then, these models will be applied to several photonic crystal systems. The central part of this chapter will be a description of radiative lifetime measurements in several systems and a discussion of the measured decay dynamics in connection with the characterization and theoretical treatments discussed previously. The chapter will conclude with a brief outlook on the impact of controlling excited state dynamics in photonic crystals on various optical applications.

Experimental Aspects of Radiative Lifetime Measurement

To study the impact of the density of optical states variations within photonic crystals on excited state dynamics, we analyzed the spontaneous emission decay rates of embedded CdSe/ZnS core-shell quantum dot (QD) light sources (‘‘eviDots’’ purchased from Evident Technologies). QDs with photoluminescence emission band positions overlapping with different parts of the photonic band structure were infiltrated into the photonic crystal samples by drop-casting from a 9:1 hexane/octane solution (9×10^{-9} M).[22] The functionalized photonic crystal samples were then placed in a quartz cell under argon atmosphere to avoid photo-oxidation and mounted on a computer-controlled 3D nanomotion stage for optical microreflectance and time-correlated single photon counting (TCSPC) emission measurements.

Because of the inherent local inhomogeneity of biological or biotemplated structures,[27-28] it is of great importance to inspect the sample quality by optical

microscopy and microreflectance spectroscopy prior to determining the spontaneous emission decay rates of QDs at various locations inside the photonic crystals. This was done by an optical setup, shown schematically in Figure 5.1 with a beam splitter/dichroic mirror combination to overlay a collimated white light source and the 405 nm line of a picosecond diode laser (Becker & Hickle BDL-405, 20 MHz repetition rate). Both beams were focused onto the sample with a 50× extra-long working distance objective (N.A. 0.55). The reflectance properties of each photonic crystal sample were first mapped out under white light illumination and at least ten spots per sample were chosen for spontaneous emission decay rate investigation. For this, the white light was blocked and the QDs were excited by the 405 nm line of the diode laser. The light emitted from the QDs was collected by the same microscope objective, directed into a spectrometer (Princeton Instruments SpectraPro 2300i), dispersed by a grating (600 grooves/mm) and detected by a thermoelectrically cooled single photon counting detector (Hamamatsu Photosensor, H7422p). Spontaneous emission decay curves were collected over a 50 ns time window at a 12 ps time resolution.

Analysis of Decay Curves

The first order rate of decay of an emitter from an initial excited state to a final state is given as the sum of the radiative and all the different nonradiative decay pathways possible as shown in equation 5.1 where Γ_{tot} is the total rate of decay, Γ_{rad} is the radiative rate, and Γ_{nrad} stands for the various nonradiative rates of decay.

(5.1) $$\Gamma_{tot} = \Gamma_{rad} + \sum \Gamma_{nrad}$$

(5.2) $$I(t) = a_1 e^{-t \cdot \Gamma_{tot}} = a_1 e^{-t/\tau}$$

Under the assumption that there is only one radiative pathway, equation 5.1 may be integrated to yield the monoexponential normalized intensity of light as a function of time as shown in equation 5.2, where *I(t)* is the time-dependent intensity, a_1 is a normalization constant, and τ is the radiative lifetime defined as $1/\Gamma_{tot}$. If more than one radiative pathway is possible, then a sum of exponential decays, typically two or three, may be used with each lifetime corresponding to a different radiative pathway, as shown in equation 5.3, where the sum of the coefficients a_n must equal one, if the decay curve is normalized.

(5.3) $$I(t) = \sum_n a_n e^{-\tau_n \cdot t}$$

When emitters are embedded within photonic crystals, the radiative rates of decay depend strongly on the frequency of emission and the physical location within the crystal due to the coupling that must take place between the emitter and the optical modes in its local environment. As was described in Chapter 4, photonic crystals can alter the local density of optical states significantly. Ensemble emission of randomly located light sources results in nonexponential decay behavior that significantly complicates interpretation of decay curves from emitters embedded inside photonic crystals.[23, 30-32]

While multiexponential decay models with four or more free parameters can numerically fit data, the result is flawed by the fact that it is known that there exists a continuous distribution of radiative lifetimes from ensembles of emitters in environments with nonhomogeneous local density of optical states. Choosing a physically meaningful model describing the local photonic density of optical states distribution is therefore of great importance for extracting relevant spontaneous emission rates from QD ensemble decay curves from within photonic crystals.

The problem of analyzing ensemble spontaneous emission from within photonic crystals has been treated previously in the context of inverse opals by Nikolaev et al.,[23] who recommended a log-normal distribution of decay rates as shown in equations 5.4, 5.5, and graphically in Figure 5.2.

(5.4) $$\varphi(\Gamma) = A \cdot \exp\left[-\frac{\ln^2(\Gamma/\Gamma_{MF})}{w^2}\right]$$

(5.5) $$I(t) = I(0)\int_{\Gamma=0}^{\infty} \varphi(\Gamma)\exp(-\Gamma \cdot t)d\Gamma$$

Equation 5.4 creates a distribution of radiative rates of decay, $\varphi(\Gamma)$, centered at the most probable decay rate Γ_{MF}, with a distribution width of w. The factor A in equation 5.4 is a normalization constant that insures integration of $\varphi(\Gamma)$ equals one. Since there is a continuum of decay rates, they are integrated rather than summed in equation 5.5. This distribution accounts for the variable local density of optical states experienced by the emitters while limiting free fitting parameters to Γ_{MF} and w, if the decay curve is normalized so that $I(0) = 1$. The maximum of the log-normal distribution represents the most probable rate of decay, while the distribution width relates to the variability of the local density of optical states over the entire photonic crystal unit cell. Here, a broad distribution width indicates that emitters experience a strong variation of local density of optical states.

The log-normal fit was used in this thesis to analyze radiative decay data so that our results could be compared with results in the literature that also use this method. However, in spite of the log-normal distribution's strong advantages of providing a reasonable model for the physical interpretation of decay in photonic crystals while limiting free fitting parameters, it still has challenges. Equation 5.5 contains an integral that must be solved numerically for each data point in the fitted curve, and since the

fitting process involves many steps this integral is solved numerically thousands of times in a single fit. To overcome this, the number of data points was limited by preprocessing the decay curves by smoothing them using a one nanosecond wide boxcar average, normalizing, and interpolating 100 points over the curve using a house-written c++ program. Numerical evaluation of the integral was incorporated using scripts into the function-fitting suite built into OriginLab® software. Another challenge presented by fitting with a log-normal distribution is the relatively shallow minimum in χ^2 (the square of the difference between the fitting curve and the data). Figure 5.3 plots χ^2 versus the free fitting parameters for four points along a sample decay curve, showing the broad range in which the fitting curve and data agree very closely. There is a minimum, however, and the shallowness of the minimum decreases as more data points are included. Qualitative analysis of the shape of the residual plots provides immediate feedback on the quality of the fit during the fitting process that can distinguish between a correct and incorrect fit. In the following section monoexponential, biexponential, and log-normal distribution models will be discussed in reference to the radiative decay of several different QD systems.

Radiative Decay Measurements in Simple Dielectric Environments

To place lifetime measurements in context and explore competing effects, the radiative lifetime of the QDs used to probe the photonic structure was measured in a hexane solution, and drop-cast onto quartz slides and titania thin films. Sample decay curves from each of these systems overlaid with monoexponential and biexponential

decay fits are shown in Figure 5.4. It was found that QDs in hexane were the most ideal system, fitting the monoexponential decay model with a lifetime of 20 ns very closely with little dependence on the solution concentration.

To test the effect that deposition on a substrate has on the lifetime, QDs solutions with varying concentrations were deposited on quartz substrates. We speculate that an inhomogeneity in local environments creates a distribution of lifetimes less dramatic than what is caused by the variability of local density of states in a photonic crystal, but still significant enough to result in observed nonexponential behavior. As the concentration of QDs on quartz was increased from 1×10^{-7} M to 1×10^{-5} M, the radiative lifetime found by fitting the decay curves to a log-normal distribution decreased from 24 ns to 13 ns as shown in Figure 5.5 indicating possible energy transfer between emitters. For comparison, the solution of QDs in hexane was also fit with a log-normal distribution. Although this fit is not the most appropriate because the QDs are in a homogenous environment, it provides useful context for the other measurements. It was found that 1×10^{-6} M solutions of QDs in hexane have a most probable rate of decay corresponding to a lifetime of 36 ns. In general it was found that the log-normal distribution yielded different results than the monoexponential decay because the most probable lifetime in a distribution doesn't necessarily correspond to the average lifetime that matches the monoexponential. However, this discrepancy is accepted so that the same method may be used for purposes of comparison across several different systems.

The same 1×10^{-6} M QD solution was drop-cast onto a titania thin film, resulting in a strongly nonexponential radiative decay, the most probable lifetime dropping to 13 ns (Figure 5.4). This reduction in lifetime is attributed to a combination of energy

transfer between QDs and electron transfer from QDs to titania, a well-documented effect that is part of the motivation for QD sensitized titania solar cells.[33] We also observed that at higher QD emission energies, photoluminescence on titania became quenched, due to the increased likelihood of QD-titania electron transfer as the lowest excitonic state of the QDs approached the titania conduction band.[34]

Radiative Decay in Photonic Crystals

The radiative lifetime/rate of decay was measured from QDs embedded in inverse opal, diamond-based chitin, and diamond-based titania photonic crystals. Since there are several factors capable of altering rate of excited state decay, such as energy or electron transfer between the QDs and the substrate/host, finding an appropriate reference material was critical. At each frequency probed in the chitin photonic crystals, we therefore measured the emission from identical QDs from within a chitin scale that has the same diamond-based structure but with a lattice constant that placed the photonic stop gaps outside of the emission of the QDs. For the *L. augustus* scales (which have photonic stop gaps in the green), we chose the scales from the red form of *P. moniliferus* (which has photonic stop gaps in the red).

To provide a baseline for the titania replica photonic crystals, we fabricated inverse opal samples consisting of the same nanocrystalline titania framework as the bioreplicas. For this, polystyrene opal templates were fabricated by self-assembly[35] and converted into inverse opals using the same titania sol infiltration and processing method as for the bioreplicas.[29] Radiative lifetime measurements of QDs embedded within inverse opals having different lattice constants were also measured to assess the impact

the single *Γ-L* stop gap experimentally has on the density of optical states. Figure 5.6 shows two representative decay curves of QDs embedded in inverse opal photonic crystals. We found that when QD emission overlapped with the prominent *Γ-L* stop gap the radiative lifetime was about 1.5 times longer than at frequencies outside of the stop gap, a finding consistent with the literature.[22-23]

After finding appropriate baseline systems, the properties of the biopolymeric photonic crystal structures, consisting of the rather low refractive index compound chitin (about 1.5),[36] were studied. Because of this low refractive index of the diamond-based lattice, this biological photonic crystal is far from opening a complete band gap. Nevertheless, our photonic band structure calculations revealed overlap of multiple low-frequency stop gaps with a combined reduction of the density of optical states of up to 40% (Figure 5.7). The effect of these overlapping stop gaps on the spontaneous emission decay behavior was significant and we found strong inhibition of spontaneous emission. In detail, the decay rate increased by a factor of two for emission inside the predicted zone of greatest density of optical states inhibition (Figure 5.7) with averaged inhibited radiative lifetimes as high as 39±6 ns. Given the low refractive index of the biopolymeric photonic crystal structure the observed inhibition of spontaneous emission is remarkable, rivaling that of the best inverse opal photonic crystals made from high-dielectric titania.

The high-dielectric titania photonic crystals with a diamond-based lattice used in this study were replicated from biopolymeric chitin scales of the beetle *L. augustus*,[27] using the double-imprint sol-gel chemistry-based biotemplation method described in Chapter 3.[29] A typical scanning electron microscopy (SEM) image and the reconstructed 3D model of the ABC-stacked air-cylinder lattice in a nanocrystalline titania matrix

(refractive index of 2.2–2.3) is shown in Figure 5.8(b). The corresponding photonic band structures and density of optical states distribution are shown in Figure 5.8, and were calculated using the MIT photonic bands package[37] and our own program[38] as described in Chapter 4 based on the work by Busch and John.[16] The defining feature is strong overlap of multiple low-frequency photonic stop gaps, including the formation of a narrow complete band gap of about 2.5% gap-width-to-mid-gap ratio.[39] This results in a significant modification of the density of optical states distribution with strong depression in the overlap region and enhancement at the edges (Figure 5.8).

Typical spontaneous emission decay curves for QDs located within the high-dielectric titania photonic crystals with a diamond-based lattice are given in Figure 5.9. Even a merely qualitative comparison of the decay curves for emission frequencies inside and outside of overlapping photonic stop gaps shows the strong impact of the photonic crystal. Not only does the photonic crystal band structure significantly alter the QD emission decay behavior, but it also results in strongly nonexponential decay behavior. The latter is the direct result of ensemble emission of randomly located light sources within the photonic crystal and displays the strong variation of the local density of optical states.[16, 23]

Quantitative QD emission decay curve analysis using the log-normal distribution fitting procedure revealed the immense impact of the photonic crystal. Average QD emission decay rates were obtained by measuring several different local positions inside the photonic crystal at a particular frequency. Within the predicted frequency zone of greatest inhibition (the simultaneous overlap of different photonic stop gaps) the QD emission decay rate was reduced by factors of more than six, resulting in a dramatic

increase in the radiative lifetime to values reaching 100 ns inside the band gap (Figure 5.10). In detail, while average QD emission decay rates were found to be 0.068±0.009 ns^{-1} (corresponding to a lifetime range of 13–18 ns) at frequencies far outside the inhibition zone, inside the band gap zone the decay rate of the same QDs decreased to values of 0.012±0.002 ns^{-1} (lifetime range of 71–100 ns). In addition, the decay rate log-normal distribution width narrowed from 0.19–0.21 ns^{-1} to 0.064–0.076 ns^{-1}. This is indicative of a reduced overall density of optical states, since contribution to the local density of optical states from several directions is eliminated, as was suggested by Nikolaev and co-workers.[23]

These inhibition results obtained from diamond-based photonic crystal structures were placed in perspective by comparing with the previously mentioned studies on inverse opals. Two important results were obtained from the inverse-opal study. First, using the same QDs as for the diamond-based photonic crystal studies, we found an inhibition of their emission by a factor of only about 1.5 inside the inverse opal Γ-L PSG (Figures 5.7(a) and 5.6) and a reduction in the distribution width. The inhibition findings in titania inverse opals agree very well with previously reported results.[22-23] This comparison—using the same light sources in both photonic crystal lattice types—provides clear evidence of the superiority of the diamond-based structure over inverse-opal structures and points out the importance of several overlapping photonic stop gaps. Secondly, the decay rates of QD emission occurring outside any stop gap of the titania inverse-opal photonic crystal gave values in the same range (13–17 ns) as we found for the titania bioreplica samples outside stop gap regions. This finding is of great importance, since the framework of both photonic crystals consists of the same sol-gel

derived titania material, and thus provides a valuable baseline as outlined above. For the following analysis we therefore used titania inverse-opal samples with stop gap positions far away from the QD emission as an important additional control system for evaluating a baseline of QD radiative decay behavior that is not directly influenced by the photonic crystal-induced density of optical states variations.

To map the density of optical states variation of the diamond-based titania photonic crystal over a broad frequency range we systematically analyzed QD decay rate behavior over a large portion of the band structure, from 16,000 to 20,000 cm^{-1}. Decay rate measurements in the high frequency regime (at and above the photonic stop gap/edge range) were also attempted. However, for CdSe/ZnS QDs with emission frequencies above 20,000 cm^{-1} the emitting $1S_e$ electronic energy level moves above the titania conduction band (located at −3.9 eV below vacuum).[34] This leads to strong QD-to-titania charge transfer.[33-34] In fact, the QD emission intensity decreased rapidly as we approached frequencies exceeding 19,000 cm^{-1} and QD emission completely disappeared beyond 20,000 cm^{-1}. Interestingly, the onset of charge transfer also seems to compensate the calculated increase in density of optical states in this regime, resulting in lower decay rates than predicted. Nevertheless, reference baseline-normalized decay rate averages of QD emission within the 16,000 to 20,000 cm^{-1} frequency range (Figure 5.10) give some important insights into the emission decay control by a real photonic crystal. Both strong inhibition over a broad frequency range (larger than ten percent bandwidth) and enhancement within the narrow range of predicted density of optical states increase at the low-frequency band edge were experimentally observed. Radiative lifetimes from 8 ns (enhancement region) to up to 100 ns (inhibition region) were obtained, spanning an

unprecedented decay variation by a factor larger than ten. The strong modification of spontaneous emission dynamics in diamond-based photonic crystals highlights the superiority of photonic crystal lattices with strong overlap of multiple photonic stop gaps—in contrast to only a single stop gap in inverse opals.

Interestingly, we found that the decay rates stayed at very constant values within the entire region of overlap of multiple stop gaps, including the narrow range of the calculated complete band gap. Since the calculated complete band gap is most likely too narrow to stay open in a real photonic crystal sample, we conclude that overlap of multiple stop gaps, but not necessarily the complete band gap, is responsible for the observed strong inhibition of excited state dynamics. The larger decay rate variations across different sampling spots (hence larger standard deviations) at the low-frequency range of the inhibition region are most likely caused by the presence of photonic stop gap/edge combinations.

Conclusion

We experimentally demonstrated the strong impact of diamond-based photonic crystal lattices on spontaneous emission decay rates. The overlap of multiple photonic stop gaps in these structures efficiently modifies spontaneous emission dynamics of embedded light sources. Both inhibition and enhancement was observed with decay rate variations by a factor larger than ten, greatly exceeding previously used titania inverse-opal photonic crystals.

In addition, we showed even when made from compounds with refractive indices of only around 1.5, diamond-based lattices possess multiple overlapping stop gaps and

strongly affect spontaneous emission dynamics—a finding that further emphasizes the superiority of diamond-based lattices.[24-26] A multitude of functional dielectrics, including optoelectronically and piezoelectrically active polymeric materials, fall in this range, paving the ground for externally tunable broadband control of excited state dynamics in bulk materials. Our findings should therefore be of high relevance for future photonic crystal design—particularly for light-localization and quantum coherence based applications that require strongly inhibited radiative decay.

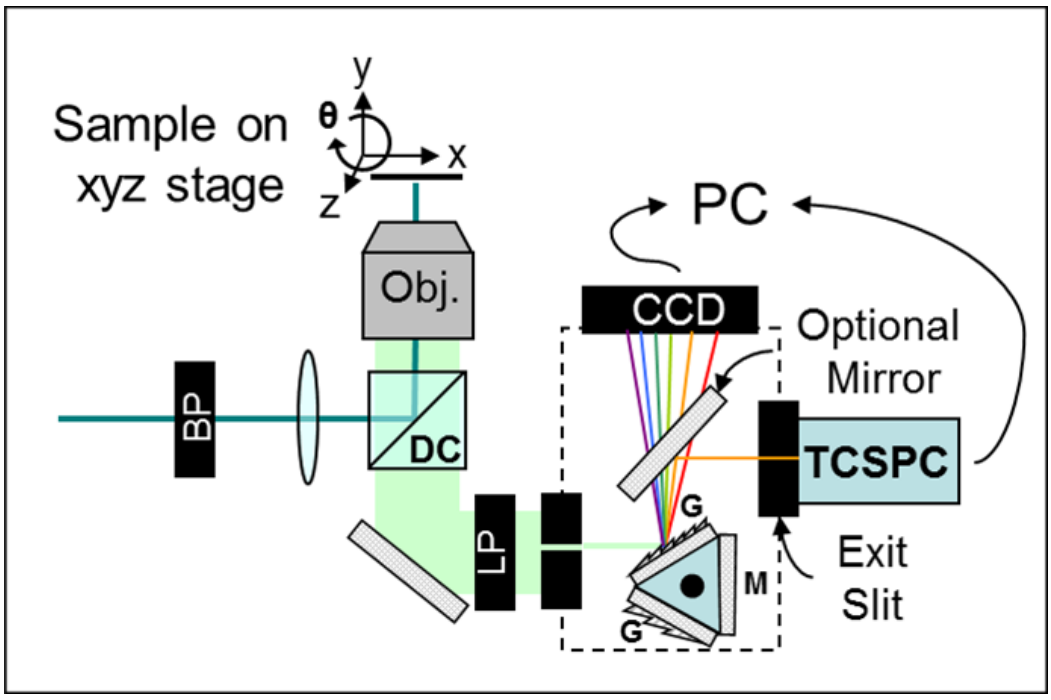

Figure 5.1 Experimental setup used to measure radiative decay with time correlated single photon counting. Pulsed laser light is directed through a microscope objective onto the sample. Fluorescence is collected by the same objective and directed to a spectrometer where a frequency range is selected and measured by a TCSPC crystal detector.

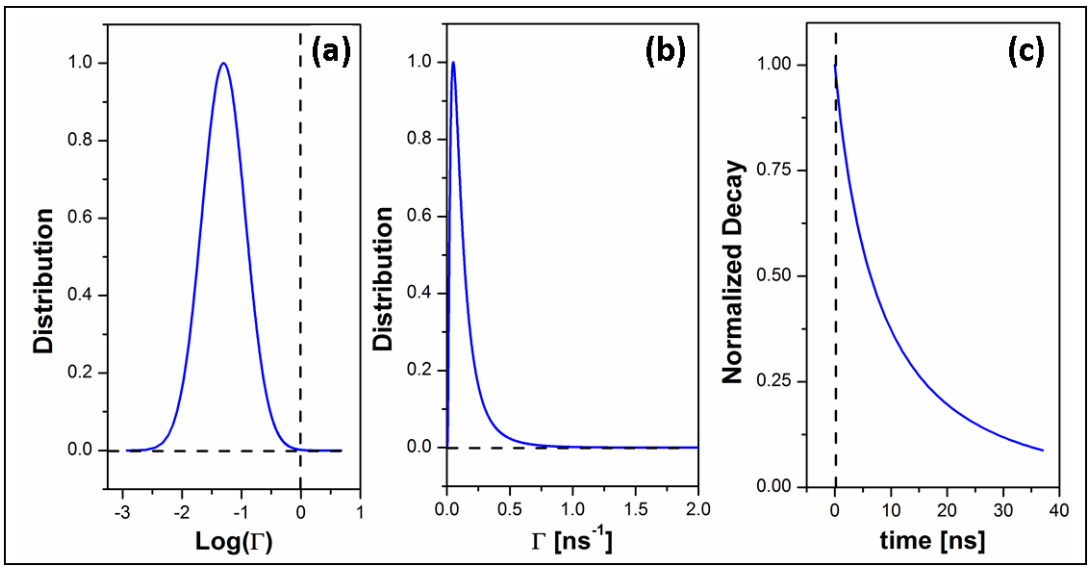

Figure 5.2 Most of the decay curves used in this study were fit with a log-normal distribution (a) that has the form of a Gaussian distribution when plotted on the log-scale, but is asymmetric on a linear scale (b). The distribution is integrated to yield a complex decay curve (c). All the curves shown here correspond to a lifetime of 20 ns (Γ_{MF} = 0.05 ns^{-1}) and width, *w*, of 1.2 (equivalent to $\Delta\Gamma$ = 0.15 ns^{-1}).

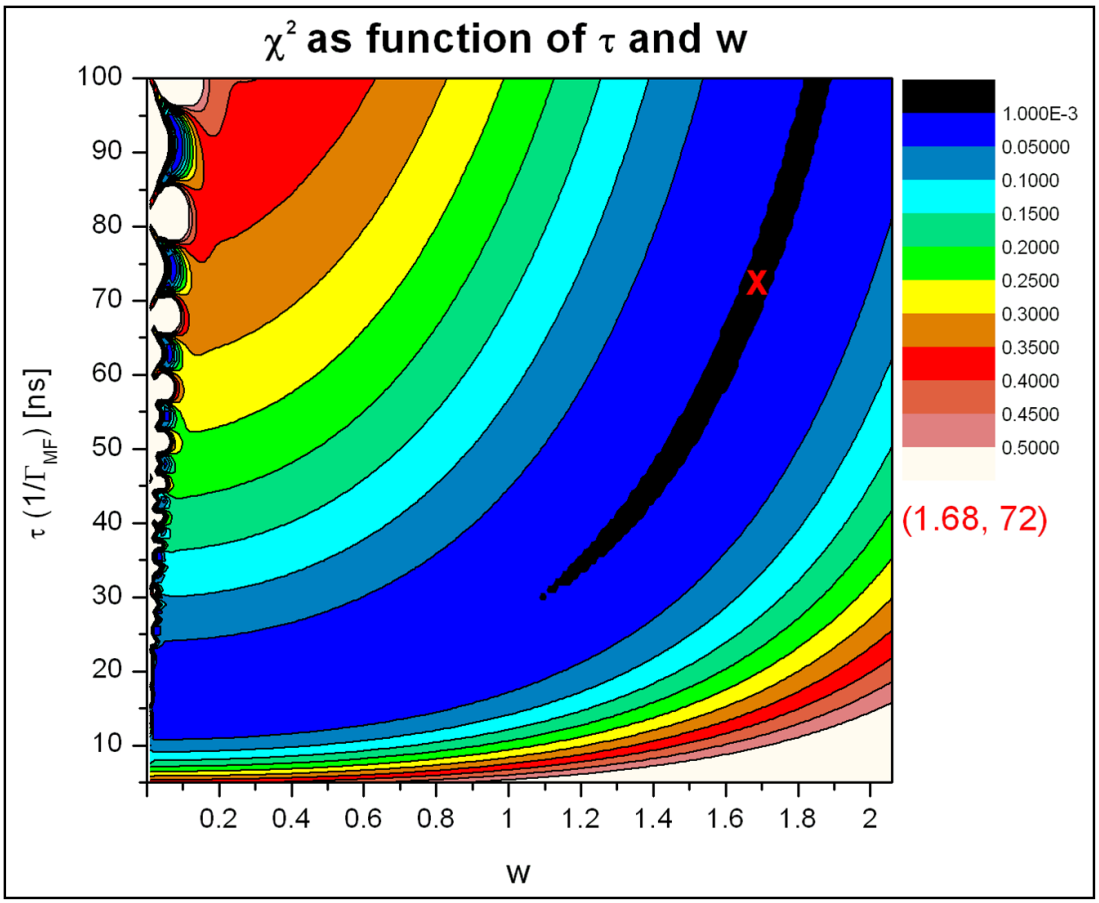

Figure 5.3 χ^2 (the squared difference between the fitting curve and data) versus the free parameters in the log-normal fit. In this case, a minimum exists in χ^2 at a lifetime of 72 ns and a distribution width of 1.68, but the minimum is in a shallow trough that makes fitting difficult.

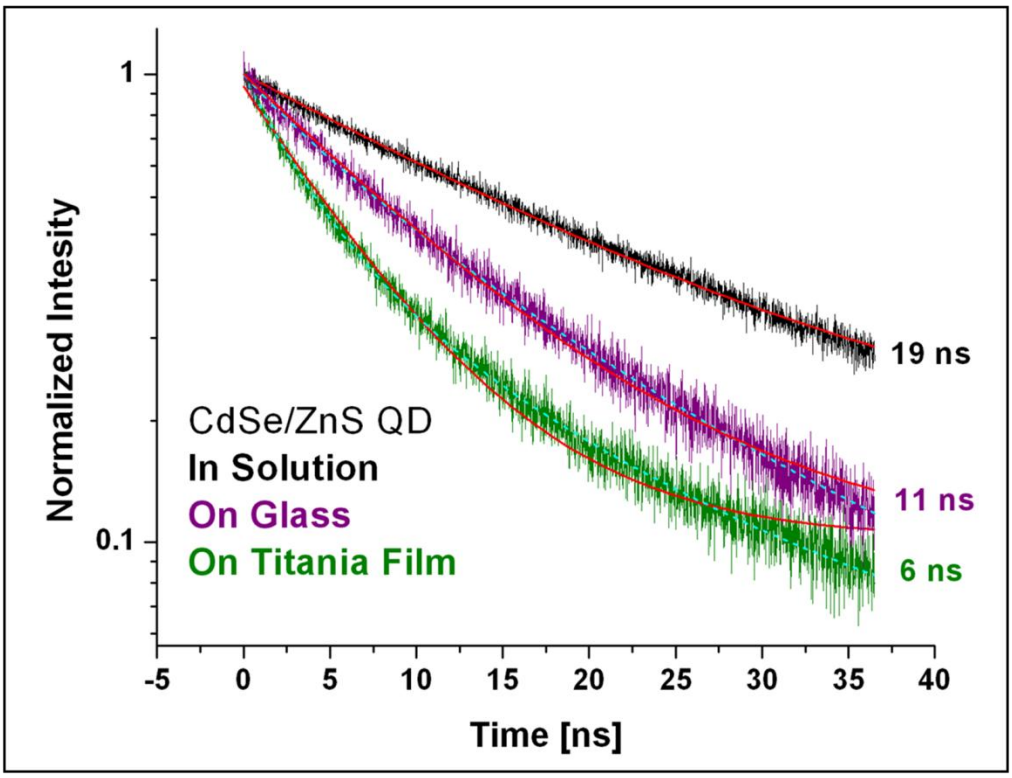

Figure 5.4 Radiative decay curves from CdSe/ZnS quantum dots in solution (top), deposited on quartz (middle), and deposited on a titania thin film (bottom) plotted on a log scale. Solid red trend lines correspond to a monoexponential decay model fit to the data. Light blue dashed lines correspond to a biexponential fit. The red monoexponential line in the top curve lies on top of the blue dashed line. It can be seen that the best monoexponential fits for the bottom two curves were inadequate.

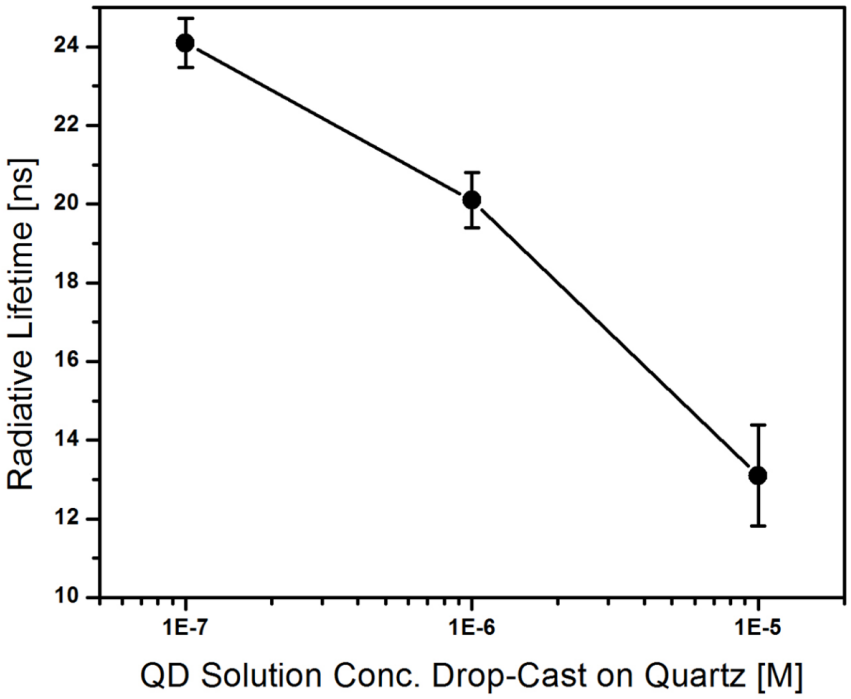

Figure 5.5 The average radiative lifetime over 10 measurements of quantum dots deposited on quartz slides at three different concentrations. As the concentration was reduced, the decay became closer to a monoexponential curve and the lifetime approached that of the quantum dots in hexane.

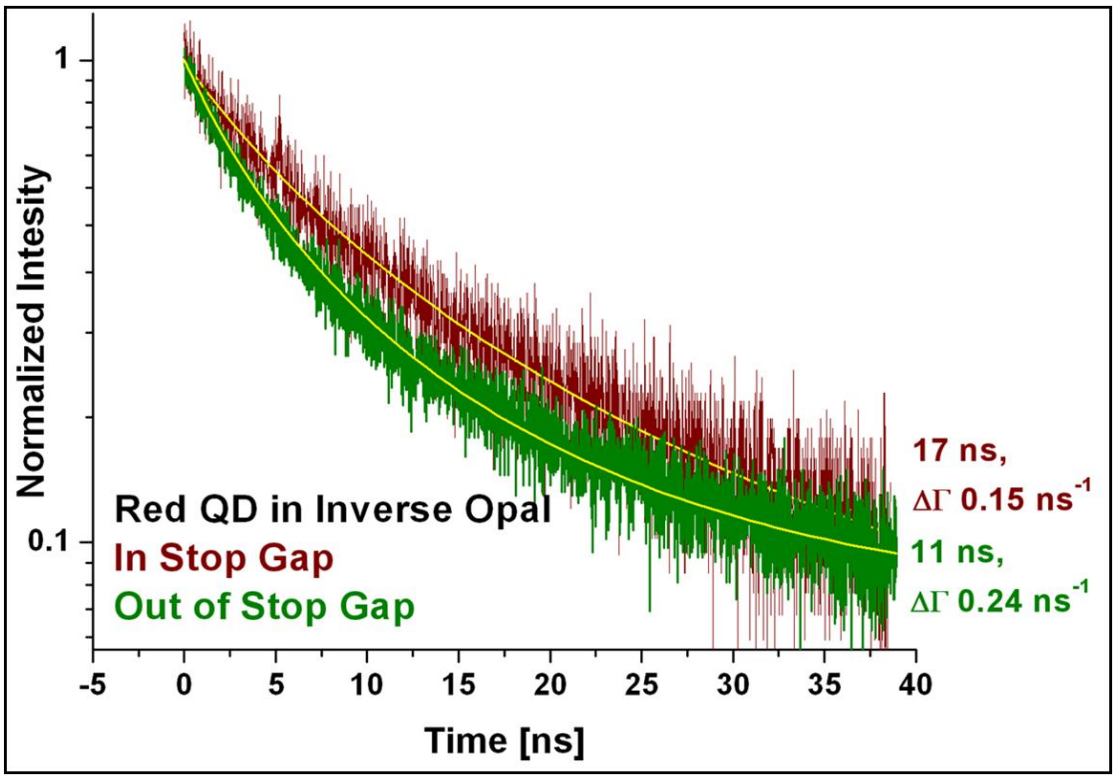

Figure 5.6 Representative decay curves from red colored quantum dots embedded in a two titania inverse opals. Quantum dots emitting at a frequency overlapping with the *Γ-L* stop gap (top) have a lifetime about 1.5 longer than quantum dots emitting outside the gap (bottom).

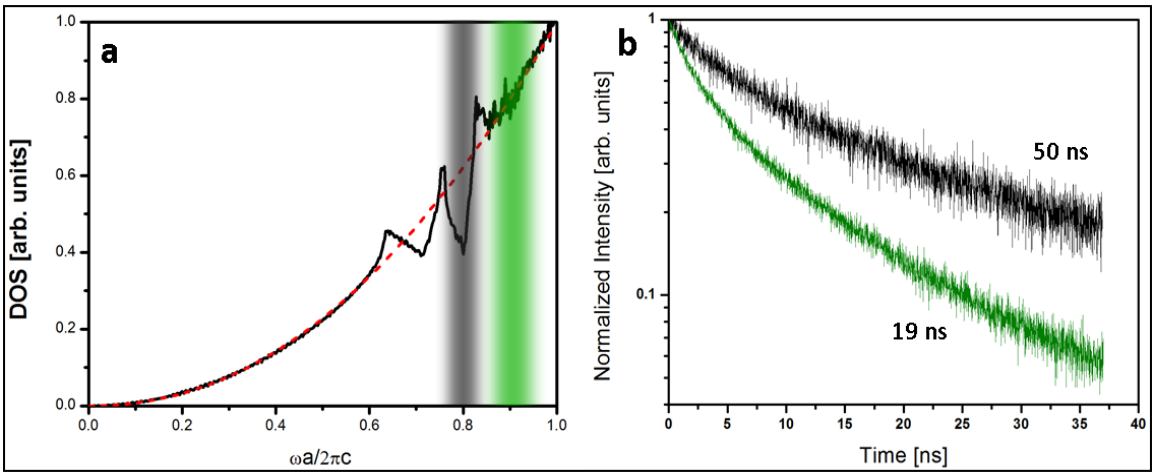

Figure 5.7 Example of the correlation between band gaps, DOS, and spontaneous emission in a chitin structure. (a) Calculated density of optical states for the biopolymeric (chitin) photonic crystal, with vertical bars indicating the frequency regions probed. (b) PL emission decay curves plotted on a normalized log scale for QDs in the region of overlapping stop gaps (top) and far away from any stop gaps (bottom). Both decay curves were measured at 18,350 cm^{-1} in two different isomorphic structures with different lattice constants. The reduced frequency positions are indicated by the vertical bars and the width of the bars resembles the lattice constant uncertainty of these biological photonic structures.

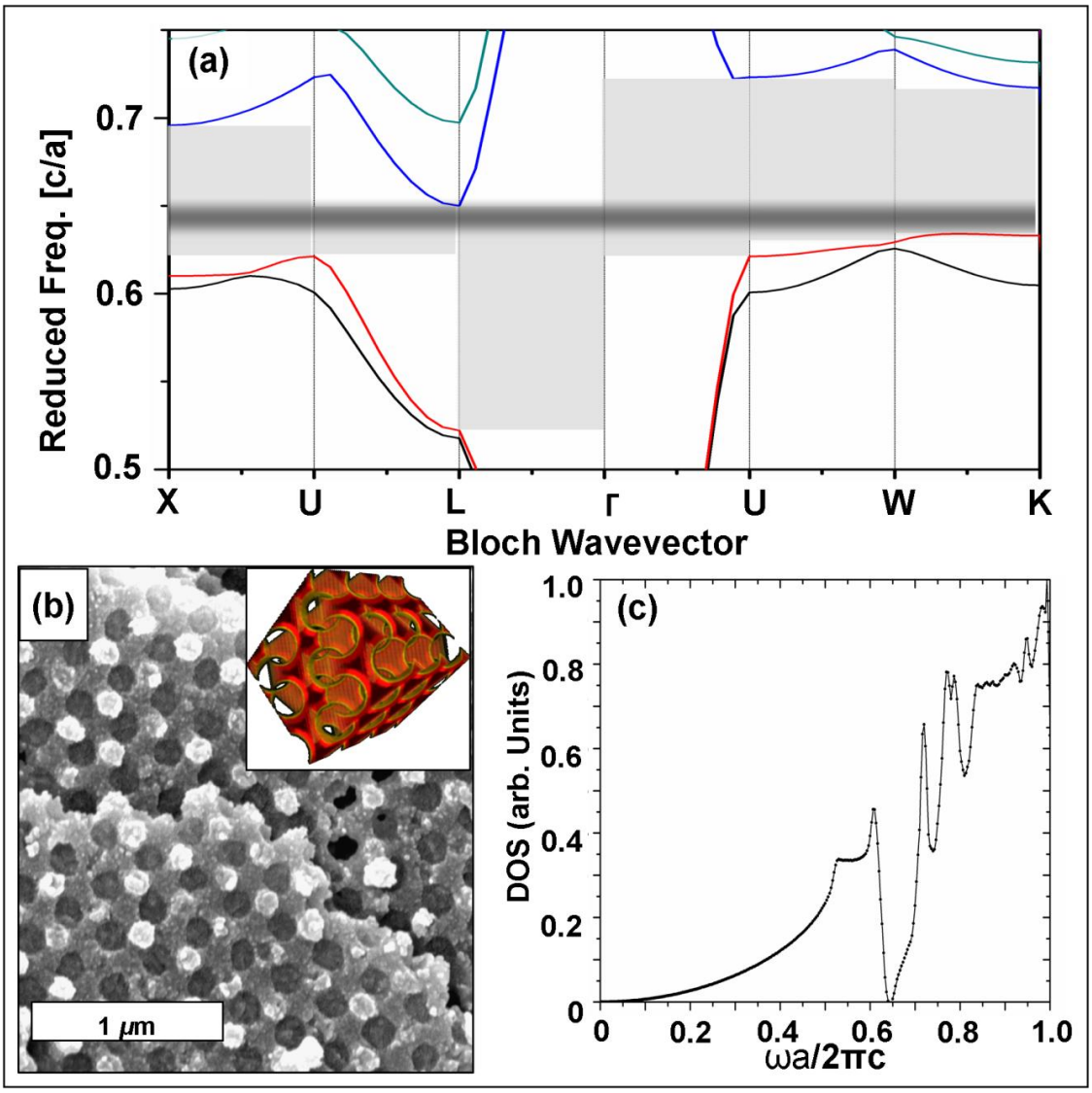

Figure 5.8 The band structure and calculated DOS corresponding to the titania replicate structure, as shown in the SEM image. (a) Calculated photonic band structure for a diamond-based lattice of air cylinders surrounded by dielectric with refractive index of 2.2; shown is the low-frequency region around the overlapping PSGs. Calculations are based on scanning electron microscopy images of the titania photonic crystal lattice (a = 354±9 nm) used in this study (b). Inset in (b) shows the dielectric model for the band structure calculations. (c) Corresponding calculated density of optical states of photonic crystal lattice described in (a). Reprinted with permission from reference 39, copyright 2011 The American Physical Society.

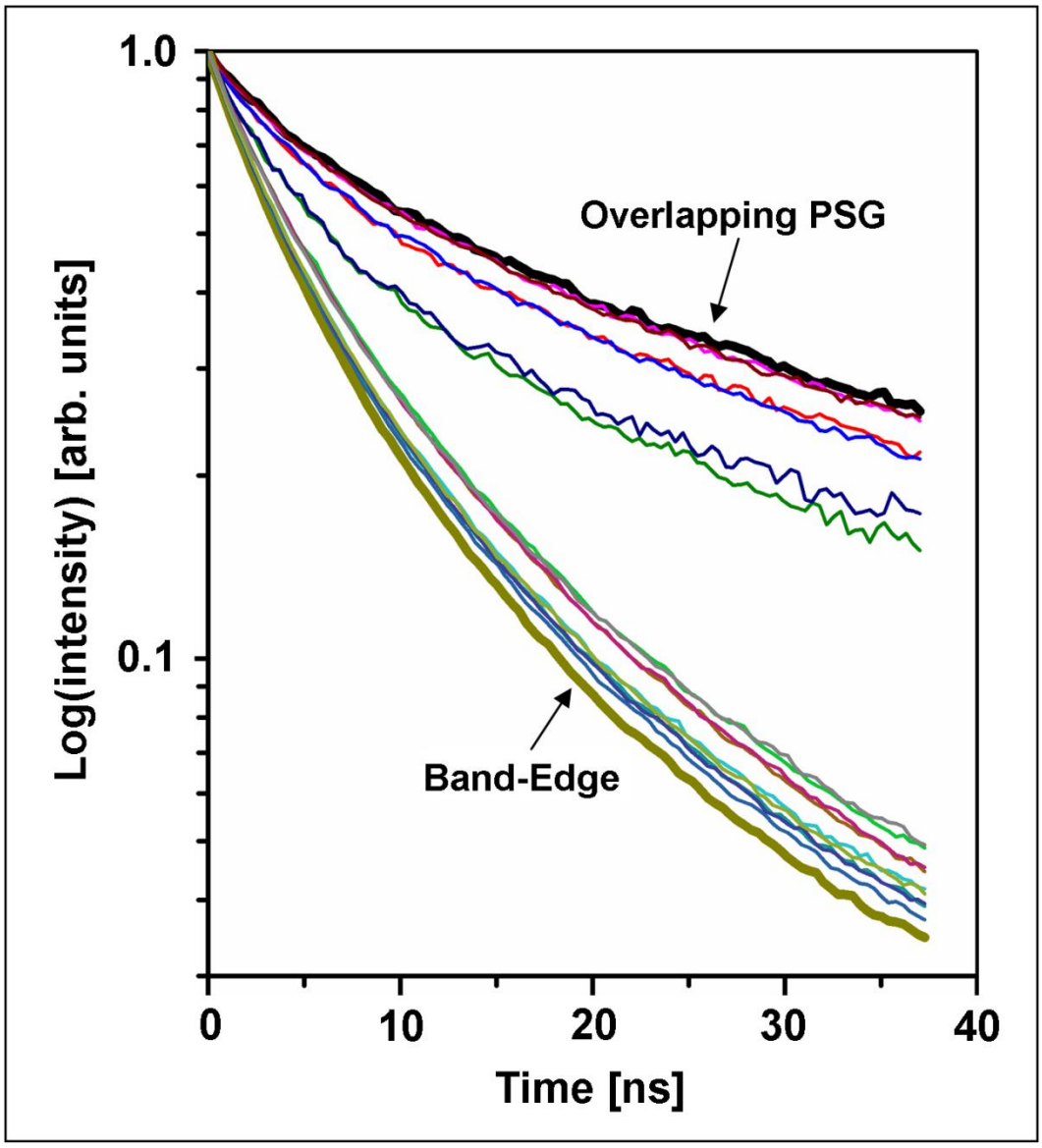

Figure 5.9 Plot of the processed decay curves used in the log-normal fitting procedure. The different groups of decay curves came from different samples, with each line in the group coming from a different spatial location, and the bold lines indicate which curves were used in Figure 5.10. The top plots showing inhibition were measured at 19,800 cm^{-1} and the bottom plots showing enhancement were measured at 16,950 cm^{-1}. Reprinted with permission from reference 39, copyright 2011 The American Physical Society.

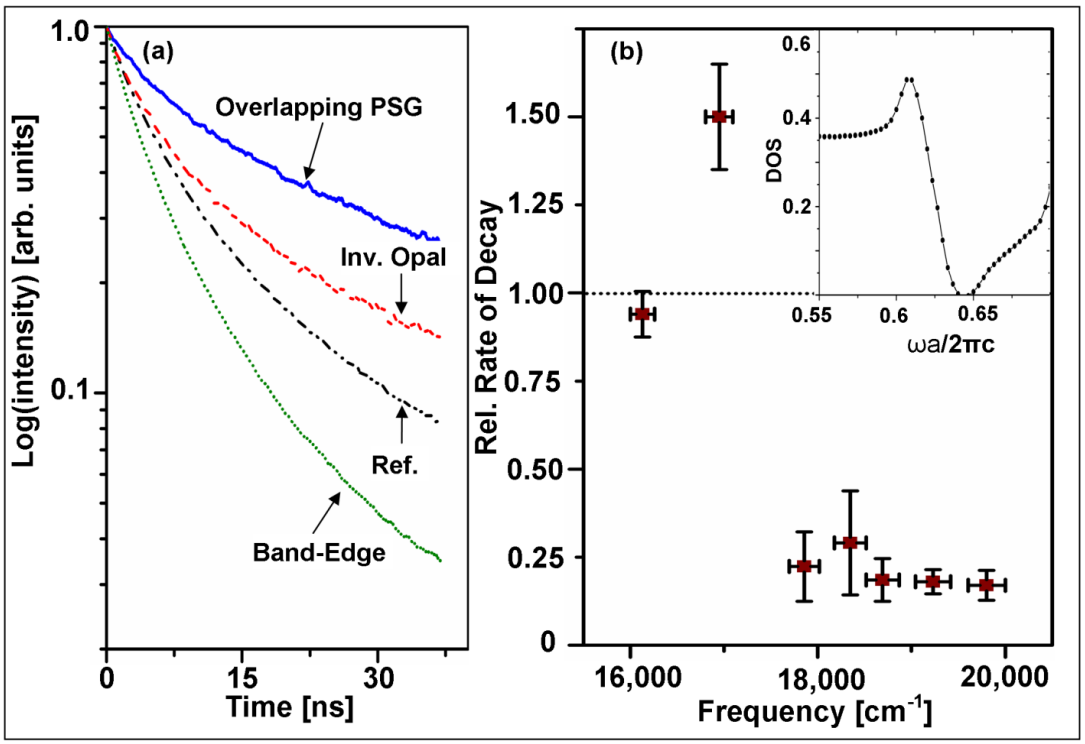

Figure 5.10 Emission decay curves and relative rates of decay for several titania measurements. (a) Selected PL emission decay curves plotted on a normalized log scale of QDs embedded into various titania photonic crystals. QD emission in the region of strong stop gap overlap (solid line; calculated lifetime of 99±2 ns) and at the low-frequency band edge (dotted; calculated lifetime 8±1 ns) of the titania photonic crystal with a diamond-based lattice (for a full range of decay curves, see Figure 5.9). QD emission inside the titania inverse opal *Γ*-*L* stop gap (dashed; calculated lifetime 20±1 ns) and in the titania reference sample outside of any stop gaps (dashed-dotted; calculated lifetime 14±0.5 ns). Reported lifetimes reflect the peak of the log-normal distribution of the decay curve fitting. (b) Decay rates of QD spontaneous emission over a broad frequency range of the band structure of the titania photonic crystal with a diamond-based lattice, including regions of normal, enhanced and emission. All decay rates are given relative to the decay rates of the same QDs in a titania reference sample outside any stop gaps. Vertical error bars indicate the variation of the measured lifetime over several spatial positions in the sample. Horizontal bars represent the spectral width over which the measurements were made. Reprinted with permission from reference 39, copyright 2011 The American Physical Society.

References

1. Loudon, R., *The Quantum Theory of Light*. Oxford University Press: New York, 2000.

2. Scully, M. O.; Zubairy, M. S., *The Quantum Theory of Light*. Cambridge University Press: Cambridge, England, 1997.

3. Yablonovitch, E., Inhibited Spontaneous Emission in Solid-State Physics and Electronics. *Phys. Rev. Lett.* **1987,** *58* (20), 2059.

4. Woldeyohannes, M.; John, S., Coherent Control of Spontaneous Emission Near a Photonic Band Edge. *J. Opt. B* **2003,** (2), R43-R82.

5. Lambropoulos, P.; et al., Fundamental Quantum Optics in Structured Reservoirs. *Rep. Prog. Phys.* **2000,** *63* (4), 455.

6. Vahala, K. J., Optical Microcavities. *Nature* **2003,** *424* (6950), 839-846.

7. Hennessy, K.; Badolato, A.; Winger, M.; Gerace, D.; Atature, M.; Gulde, S.; Falt, S.; Hu, E. L.; Imamoglu, A., Quantum Nature of a Strongly Coupled Single Quantum Dot-Cavity System. *Nature* **2007,** *445* (7130), 896-899.

8. John, S., Strong Localization of Photons in Certain Disordered Dielectric Superlattices. *Phys. Rev. Lett.* **1987,** *58* (23), 2486.

9. Joannopoulos, J. D.; Villeneuve, P. R.; Fan, S., Photonic Crystals: Putting a New Twist on Light. *Nature* **1997,** *386* (6621), 143-149.

10. Blanco, A.; Chomski, E.; Grabtchak, S.; Ibisate, M.; John, S.; Leonard, S. W.; Lopez, C.; Meseguer, F.; Miguez, H.; Mondia, J. P.; Ozin, G. A.; Toader, O.; van Driel, H. M., Large-Scale Synthesis of a Silicon Photonic Crystal with a Complete Three-Dimensional Bandgap near 1.5 Micrometres. *Nature* **2000,** *405* (6785), 437-440.

11. García-Santamaría, F.; Xu, M.; Lousse, V.; Fan, S.; Braun, P. V.; Lewis, J. A., A Germanium Inverse Woodpile Structure with a Large Photonic Band Gap. *Adv. Mater.* **2007,** *19*, 1567–1570.

12. Y. A. Vlasov, X. Z. B., J. C. Sturm, D. J. Norris, On-Chip Natural Assembly of Silicon Photonic Bandgap Crystals. *Nature* **2001,** *414*, 289-293.

13. Maldovan, M.; Thomas, E. L.; Carter, C. W., Layer-By-Layer Diamond-Like Woodpile Structure with a Large Photonic Band Gap. *Appl. Phys. Lett.* **2004,** *84* (3), 362-364.

14. Qi, M. H.; Lidorikis, E.; Rakich, P. T.; Johnson, S. G.; Joannopoulos, J. D.; Ippen, E. P.; Smith, H. I., A Three-Dimensional Optical Photonic Crystal with Designed Point Defects. *Nature* **2004,** *429* (6991), 538-542.

15. Aoki, K.; Guimard, D.; Nishioka, M.; Nomura, M.; Iwamoto, S.; Arakawa, Y., Coupling of Quantum-Dot Light Emission with a Three-Dimensional Photonic-Crystal Nanocavity. *Nat. Photonics* **2008,** *2* (11), 688-692.

16. Busch, K.; John, S., Photonic Band Gap Formation in Certain Self-Organizing Systems. *Phys. Rev. E* **1998,** *58* (3), 3896.

17. Fujita, M.; Takahashi, S.; Tanaka, Y.; Asano, T.; Noda, S., Simultaneous Inhibition and Redistribution of Spontaneous Light Emission in Photonic Crystals. *Science* **2005,** *308* (5726), 1296-1298.

18. Holland, B. T.; Blanford, C. F.; Stein, A., Synthesis of Macroporous Minerals with Highly Ordered Three-Dimensional Arrays of Spheroidal Voids. *Science* **1998,** *281* (5376), 538-540.

19. Wijnhoven, J.; Vos, W. L., Preparation of Photonic Crystals Made of Air Spheres in Titania. *Science* **1998,** *281* (5378), 802-804.

20. Subramanian, G.; Manoharan, V. N.; Thorne, J. D.; Pine, D. J., Ordered Macroporous Materials by Colloidal Assembly: A Possible Route to Photonic Bandgap Materials. *Adv. Mater.* **1999,** *11* (15), 1261-1265,1233.

21. Galusha, J. W.; Tsung, C. K.; Stucky, G. D.; Bartl, M. H., Optimizing Sol-Gel Infiltration and Processing Methods for the Fabrication of High-Quality Planar Titania Inverse Opals. *Chem. Mater.* **2008,** *20* (15), 4925-4930.

22. Lodahl, P.; Floris van Driel, A.; Nikolaev, I. S.; Irman, A.; Overgaag, K.; Vanmaekelbergh, D.; Vos, W. L., Controlling the Dynamics of Spontaneous Emission from Quantum Dots by Photonic Crystals. *Nature* **2004,** *430* (7000), 654-657.

23. Nikolaev, I. S.; Lodahl, P.; Floris van Driel, A.; Femius Koenderink, A.; Vos, W. L., Strongly Nonexponential Time-Resolved Fluorescence of Quantum-Dot Ensembles in Three-Dimensional Photonic Crystals. *Phys. Rev. B* **2007,** *75* (11), 115302.

24. Ho, K. M.; Chan, C. T.; Soukoulis, C. M., Existence of a Photonic Gap in Periodic Dielectric Structures. *Phys. Rev. Lett.* **1990,** *65* (25), 3152.

25. Moroz, A., Metallo-Dielectric Diamond and Zinc-Blende Photonic Crystals. *Phys. Rev. B* **2002,** *66* (11), 115109.

26. Maldovan, M.; Thomas, E. L., Diamond-Structured Photonic Crystals. *Nat. Mater.* **2004,** *3* (9), 593-600.

27. Galusha, J. W.; Richey, L. R.; Gardner, J. S.; Cha, J. N.; Bartl, M. H., Discovery of a Diamond-Based Photonic Crystal Structure in Beetle Scales. *Phys. Rev. E* **2008,** *77* (5), 050904(1-4).

28. Galusha, J. W.; Richey, L. R.; Jorgensen, M. R.; Gardner, J. S.; Bartl, M. H., Study of Natural Photonic Crystals in Beetle Scales and their Conversion into Inorganic Structures via a Sol-Gel Bio-templating Route. *J. Mater. Chem.* **2010,** *20* (7), 1277-1284.

29. Galusha, J. W.; Jorgensen, M. R.; Bartl, M. H., Diamond-Structured Titania Photonic-Bandgap Crystals from Biological Templates. *Adv. Mater.* **2010,** *22* (1), 107-110.

30. Driel, A. F. v.; Nikolaev, I. S.; Vergeer, P.; Lodahl, P.; Vanmaekelbergh, D.; Vos, W. L., Statistical Analysis of Time-Resolved Emission from Ensembles of Semiconductor Quantum Dots: Interpretation of Exponential Decay Models. *Phys. Rev. B* **2007,** *75* (3), 035329.

31. Nikolaev, I. S.; Lodahl, P.; Vos, W. L., Fluorescence Lifetime of Emitters with Broad Homogeneous Linewidths Modified in Opal Photonic Crystals. *J. Phys. Chem. C* **2008,** *112* (18), 7250-7254.

32. Nikolaev, I. S.; Vos, W. L.; Koenderink, A. F., Accurate Calculation of the Local Density of Optical States in Inverse-Opal Photonic Crystals. *J. Opt. Soc. Am. B* **2009,** *26* (5), 987-997.

33. Kamat, P. V., Quantum Dot Solar Cells. Semiconductor Nanocrystals as Light Harvesters. *J. Phys. Chem. C* **2008,** *112* (48), 18737-18753.

34. Jasieniak, J.; Pacifico, J.; Signorini, R.; Chiasera, A.; Ferrari, M.; Martucci, A.; Mulvaney, P., Luminescence and Amplified Stimulated Emission in CdSe–ZnS-Nanocrystal-Doped TiO2 and ZrO2 Waveguides. *Adv. Funct. Mater.* **2007,** *17* (10), 1654-1662.

35. Im, S. H.; Kim, M. H.; Park, O. O., Thickness Control of Colloidal Crystals with a Substrate Dipped at a Tilted Angle into a Colloidal Suspension. *Chem. Mater.* **2003,** *15* (9), 1797-1802.

36. Noyes, J. A.; Vukusic, P.; Hooper, I. R., Experimental Method for Reliably Establishing the Refractive Index of Buprestid Beetle Exocuticle. *Opt. Express* **2007,** *15* (7), 4351-4358.

37. Johnson, S.; Joannopoulos, J., Block-Iterative Frequency-Domain Methods for Maxwell's Equations in a Planewave Basis. *Opt. Express* **2001,** *8* (3), 173-190.

38. Jorgensen, M. R.; Yonkee, B.; Bartl, M. H. In *Strong Modification of Density of Optical States in Biotemplated Photonic Crystals*, SPIE 8071, Prague, Czech Republic, Bertolotti, M., Ed. SPIE: Prague, Czech Republic, 2011; pp 807109-9.

39. Jorgensen, M. R.; Galusha, J. W.; Bartl, M. H., Strongly Modified Spontaneous Emission Rates in Diamond-Structured Photonic Crystals. *Phys. Rev. Lett.* **2011,** *107* (14), 143902.

CHAPTER 6

CONCLUDING REMARKS AND OUTLOOK

Summary

The primary focus of this thesis has been the creation of photonic crystals from biological templates, the details of their characterization, and the measurement of photonic crystals' nonclassical effects towards an understanding of the relationships between material, structure, and properties of these new types of electromagnetic environments. We began in Chapter 1 with a discussion of how the three underlying disciplines, photonics, biology, and physical chemistry, are being woven together into the field encompassing bioreplicated or biomimetic photonics. Background in structural coloration in nature, photonic crystal theory, and materials chemistry has been given. New biotemplated photonic crystal structures that address some of the challenges of previous examples were described in Chapter 2. In Chapters 3 and 4 we have provided insight into the characterization of photonic crystals using a combination of reflection measurements, SEM images, photonic bands, and calculated density of optical states. Particular focus has been given with respect to the volume fraction and refractive index of photonic crystals. Finally, the unprecedented effect diamond-based photonic crystals can have on spontaneous emission has been demonstrated in Chapter 5.

The field of photonic crystal research has significantly evolved since its sudden beginning just 30 years ago. Photonic crystals started purely as a theoretical concept in a pair of articles published in *Physical Review Letters.*[1-2] For years, a robust theory of photonic crystals was developed computationally before[1-7] it was even know if a full photonic band gap was physically possible.[8] This birth in theory—before any experimental observation—has led to some problems as researchers initially tried to fit experiments to the existing theory rather than modifying/adapting strict theoretical predictions to explain observations on real systems. For example, theoretical treatments do not take into account (or only very limited) nonidealities such as finite sample size, crystal lattice defects, and surface/interface effects—all of which are of great importance in real photonic crystal samples, affecting their properties. This thesis focused on adapting photonic crystal theory to observations obtained from real samples, admitting limitations in the application of the highly idealized theoretical concepts to our finite and nonideal photonic crystal samples derived from nature. In the process, a deeper insight into the connection between real photonic crystals and their properties in the context of theory was developed, helping to better understand the properties of nonideal photonic crystals, correctly interpret experimental results, and obtain a more meaningful appreciation about the potential and limitations of real photonic crystal samples.

Perhaps the most significant achievement of the research behind this thesis is that, even while admitting nonidealities, we have demonstrated an unsurpassed ability to control the spontaneous emission of light sources in a bulk material.[9-10] By accepting the limits of our system, we have been open to the exploration of other nonideal photonic systems, producing interesting results on the uneven contribution of photonic crystal

directions to the overall density of optical states. Because we have noticed the value of naturally occurring photonic crystals, and have observed that imperfect crystals can still be useful, a whole range of new experiments are possible.

Future Experiments and Applications of the Current Work

The work represented here, along with the foundational work of Jeremy Galusha and others in the Bartl group,[11-16] has paved the ground for a multitude of new investigations and applications of photonic crystal based systems. The experimental expertise and theoretical framework are in place for many interesting studies. As was mentioned in Chapter 2, four "inverse type" structures can be created from an individual biological template.[16] The benefit of these inverse structures is that they can be created in a single templating step, greatly increasing yield. The ease in making these structures makes them amiable to further experimental investigation of modified density of optical states geared towards particular applications in solar energy conversion and light amplification. By making a series of photonic crystals with varying lattice parameters, the density of optical states could be explored nearly continuously over a large portion of the band structure. In addition, as was briefly mentioned in Chapter 5, such a detailed study of the relationship between structure, predicted density of optical states, and observation could yield important insight into the details of electron transfer between quantum dots and titania, a process of utmost importance in photocatalysis and photovoltaics.[17-18]

Very recently, experiments in biotemplating photonic crystals using functional polymer materials have shown promising preliminary results. Use of the already mature

field of polymer materials in biotemplated photonics allows for the creation and investigation of many interesting systems. For example, polymers with a refractive index responsive to their chemical environments could be used to make highly sensitive nonlinear optical sensors. Piezoelectric polymers[19-21] could be used to create a photonic crystal with a lattice constant modulated by external electric field, resulting in highly dynamic optical effects useful for optical filters and switches. The strong modification of density of optical states within diamond-based photonic crystals provides the opportunity for cavity-less lasing.[22-24] This might be accomplished if photonic crystals are templated using a polymer impregnated with highly dyes of high photoluminescence quantum efficiency.[25-27] Future work will include trying to induce lasing in dye-doped biotemplated photonic crystals.

In spite of the robust theoretical backbone of photonic crystals currently available, there is still work that needs to be done to bridge the gap between the highly idealized computational models used and real samples with surfaces and defects. One way this might be addressed is by comparing electronic density plots of photonic modes calculated using idealized methods, like MPB, with those calculated using finite element analysis. Finite element analysis has only recently been applied to photonic crystal problems, mainly fibers,[28-29] due to the number of elements (and time) required by the complexity of the structure. However, with advancements in computational capability a rigorous treatment of photonics using finite element analysis is possible.

Through the work of this thesis, we have matured from showing how a structure found in the scales of a destructive insect fit a highly sought after and idealized theoretical model to gaining understanding from that same structure's nonidealities.

Learning along the way with the rest of the photonic crystal community, I have cut a jagged path. While there have been many hundreds of failed samples, there have been a few successes along the way. We have gained powerful insight into the structure/property relationships of real photonic crystal systems. We demonstrated that a structure naïvely pursued by a graduate student, in pursuit of a full photonic band gap does in fact control visible light in three dimensions better than any other real material in the literature, a finding that we profoundly enjoy.

References

1. John, S., Strong Localization of Photons in Certain Disordered Dielectric Superlattices. *Phys. Rev. Lett.* **1987,** *58* (23), 2486.

2. Yablonovitch, E., Inhibited Spontaneous Emission in Solid-State Physics and Electronics. *Phys. Rev. Lett.* **1987,** *58* (20), 2059.

3. Yablonovitch, E.; Gmitter, T. J., Photonic Band Structure: The Face-Centered-Cubic Case. *Physical Review Letters* **1989,** *63* (18), 1950-1953.

4. John, S.; Wang, J., Quantum Electrodynamics near a Photonic Band Gap: Photon Bound States and Dressed Atoms. *Physical Review Letters* **1990,** *64* (20), 2418-2421.

5. Kurizki, G., Two-Atom Resonant Radiative Coupling in Photonic Band Structures. *Physical Review A* **1990,** *42* (5), 2915-2924.

6. Leung, K. M.; Liu, Y. F., Full Vector Wave Calculation of Photonic Band Structures in Face-Centered-Cubic Dielectric Media. *Physical Review Letters* **1990,** *65* (21), 2646-2649.

7. Maddox, J., Photonic Band-Gaps Bite the Dust. *Nature* **1990,** *348,* 481.

8. Ho, K. M.; Chan, C. T.; Soukoulis, C. M., Existence of a Photonic Gap in Periodic Dielectric Structures. *Phys. Rev. Lett.* **1990,** *65* (25), 3152.

9. Jorgensen, M. R.; Galusha, J. W.; Bartl, M. H., Strongly Modified Spontaneous Emission Rates in Diamond-Structured Photonic Crystals. *Phys. Rev. Lett.* **2011,** *107* (14), 143902.

10. Jorgensen, M. R.; Yonkee, B.; Bartl, M. H. In *Strong Modification of Density of Optical States in Biotemplated Photonic Crystals*, SPIE 8071, Prague, Czech Republic, Bertolotti, M., Ed. SPIE: Prague, Czech Republic, 2011; pp 807109-9.

11. Galusha, J. W.; Richey, L. R.; Gardner, J. S.; Cha, J. N.; Bartl, M. H., Discovery of a Diamond-Based Photonic Crystal Structure in Beetle Scales. *Phys. Rev. E* **2008,** *77* (5), 050904(1-4).

12. Galusha, J. W.; Tsung, C. K.; Stucky, G. D.; Bartl, M. H., Optimizing Sol-Gel Infiltration and Processing Methods for the Fabrication of High-Quality Planar Titania Inverse Opals. *Chem. Mater.* **2008,** *20* (15), 4925-4930.

13. Galusha, J. W.; Jorgensen, M. R.; Bartl, M. H., Diamond-Structured Titania Photonic-Bandgap Crystals from Biological Templates. *Adv. Mater.* **2010,** *22* (1), 107-110.

14. Galusha, J. W.; Richey, L. R.; Jorgensen, M. R.; Gardner, J. S.; Bartl, M. H., Study of Natural Photonic Crystals in Beetle Scales and their Conversion into Inorganic Structures via a Sol-Gel Bio-templating Route. *J. Mater. Chem.* **2010,** *20* (7), 1277-1284.

15. Jorgensen, M. R.; Bartl, M. H., Biotemplating Routes to Three-Dimensional Photonic Crystals. *J. Mater. Chem.* **2011,** *21* (29), 10583-10591.

16. Jorgensen, M. R.; Yonkee, B. P.; Bartl, M. H., Solid and Hollow Inorganic Replicas of Biological Photonic Crystals. *Scripta Mater.* **2011,** *65* (11), 954-957.

17. Kamat, P. V., Quantum Dot Solar Cells. Semiconductor Nanocrystals as Light Harvesters. *J. Phys. Chem. C* **2008,** *112* (48), 18737-18753.

18. Jasieniak, J.; Pacifico, J.; Signorini, R.; Chiasera, A.; Ferrari, M.; Martucci, A.; Mulvaney, P., Luminescence and Amplified Stimulated Emission in CdSe–ZnS-Nanocrystal-Doped TiO2 and ZrO2 Waveguides. *Adv. Funct. Mater.* **2007,** *17* (10), 1654-1662.

19. Chidsey, C. E. D.; Murray, R. W., Electroactive Polymers and Macromolecular Electronics. *Science* **1986,** *231* (4733), 25-31.

20. Pierre, U., PVDF Piezoelectric Polymer. *Sensor Review* **2001,** *21* (2), 118-126.

21. Rogge, T.; Rummler, Z.; Schomburg, W. K., Polymer Micro Valve with a Hydraulic Piezo-Drive Fabricated by the AMANDA process. *Sensors and Actuators A: Physical* **2004,** *110* (1-3), 206-212.

22. Painter, O.; Lee, R. K.; Scherer, A.; Yariv, A.; O'Brien, J. D.; Dapkus, P. D.; Kim, I., Two-Dimensional Photonic Band-Gap Defect Mode Laser. *Science* **1999,** *284* (5421), 1819-1821.

23. Woldeyohannes, M.; John, S., Coherent Control of Spontaneous Emission Near a Photonic Band Edge. *J. Opt. B* **2003,** (2), R43-R82.

24. Park, H.-G.; Kim, S.-H.; Kwon, S.-H.; Ju, Y.-G.; Yang, J.-K.; Baek, J.-H.; Kim, S.-B.; Lee, Y.-H., Electrically Driven Single-Cell Photonic Crystal Laser. *Science* **2004,** *305* (5689), 1444-1447.

25. Hide, F.; Díaz-García, M. A.; Schwartz, B. J.; Andersson, M. R.; Pei, Q.; Heeger, A. J., Semiconducting Polymers: A New Class of Solid-State Laser Materials. *Science* **1996,** *273* (5283), 1833-1836.

26. Somasundaram, G.; Ramalingam, A., Gain Studies of Rhodamine 6G Dye Doped Polymer Laser. *Journal of Photochemistry and Photobiology A: Chemistry* **1999,** *125* (1-3), 93-98.

27. Brouwer, H.-J.; Krasnikov, V. V.; Hilberer, A.; Wildeman, J.; Hadziioannou, G., Novel High Efficiency Copolymer Laser Dye in the Blue Wavelength Region. *Applied Physics Letters* **1995,** *66* (25), 3404-3406.

28. Brechet, F.; Marcou, J.; Pagnoux, D.; Roy, P., Complete Analysis of the Characteristics of Propagation into Photonic Crystal Fibers, by the Finite Element Method. *Optical Fiber Technology* **2000,** *6* (2), 181-191.

29. Frei, W. R.; Johnson, H. T., Finite-Element Analysis of Disorder Effects in Photonic Crystals. *Physical Review B* **2004,** *70* (16), 165116.